

ISSN 1605-2730

# **MATERIALS PHYSICS AND MECHANICS**

**Vol. 1, No. 1, 2000**

# MATERIALS PHYSICS AND MECHANICS

## PRINCIPAL EDITORS

**V. P. Bulatov**

**I. A. Ovid'ko**

*Institute of Problems  
of Mechanical Engineering  
(Russian Academy of Sciences (RAS))*

*Institute of Problems  
of Mechanical Engineering  
(Russian Academy of Sciences (RAS))*

## EDITORIAL STAFF

**I. Yu. Archakov, Staff Editor**  
**A. B. Reizis, Production Editor**

**V. F. Stepanets, Production Editor**

## EDITORIAL BOARD

**Y. G. Gogotsi**  
*University of Illinois  
at Chicago, USA*  
**S. A. Kukushkin**  
*Institute of Problems  
of Mechanical Engineering (RAS)*

**A. E. Romanov**  
*Ioffe Physico-Technical  
Institute (RAS)*  
**Y. F. Titovets**  
*St. Petersburg State Technical  
University, Russia*  
**A. Tholen**  
*Chalmers Laboratory, Sweden*

## Editorial Office:

### Materials Physics and Mechanics Editorial Office

Institute of Problems of Mechanical Engineering (Russian Academy of Sciences),  
Bolshoi 61, Vas. Ostrov, St. Petersburg 199178, Russia  
FAX +7(812)3214771  
E-mail:mpm@def.ipme.ru  
Web-sites: <http://www.ipme.ru/e-journals/MPM/>  
<http://www.ipme.nw.ru/e-journals/MPM/>  
<http://mclab.me.uic.edu/MPM>

**Materials Physics and Mechanics (ISSN 1605-2730)** – Published quarterly, one volume per year, by Advanced Study Center Co. Ltd. (St.Petersburg, Russia)

**Editorial Policy.** The journal specializes in the rapid publication of international conference proceedings in every area of materials physics and mechanics. This permits such proceedings to be conveniently referenced, abstracted and read. All contributions are edited by the corresponding guest editor(s) and they may not be published elsewhere. The journal will cover research activities in physics and mechanics of the traditional as well as the newly emerging materials.

## Owner Organizations:

Institute of Problems of Mechanical Engineering  
(Russian Academy of Sciences, St.Petersburg, Russia)

Advanced Study Center Co. Ltd.  
(St.Petersburg, Russia)



# **Materials Physics and Mechanics**

**Volume 1, Number 1, March 2000**

20010808 128

AQ F01-11-2211

**Editorial Policy.** The journal specializes in the rapid publication of international conference proceedings in every area of materials physics and mechanics. This permits such proceedings to be conveniently referenced, abstracted and read. All contributions are edited by the corresponding guest editor(s) and they may not be published elsewhere. The journal will cover research activities in physics and mechanics of the traditional as well as the newly emerging materials.

International Workshop on  
**APPLIED ASPECTS OF INTERFACE SCIENCE (AAIS)**  
(St.Petersburg, Russia; September 22 - 24, 1999)

**Sponsored by**

*US Office of Naval Research, International Field Office, Europe*

*European Office of Aerospace Research and Development, UK*

*European Research Office of the US Army, UK*

**Announcement:**

If any one technology can be said to shape the face of today society, it is materials technology. New materials, materials processes and applications are of major importance in boosting other military and civilian technological sectors such as electronics, energy technology and aerospace engineering. The objective of this Workshop is to present current research on advanced nanostructured materials and high temperature superconducting materials (characterized by nano-scaled coherence length) with the special attention being paid to the effect of interfaces on the unique, commonly highly desired properties of such materials as well their applications in various high technology areas. The Workshop aims to assess the current status and to identify future directions of R&D and applications of nanostructured bulk solids, films and coatings as well as polycrystalline superconducting materials. Particular emphasis is placed on developing close interactions and fostering future collaborations among scientists and engineers from the USA, Russia and other countries.

**We plan to focus to the following topics:**

Synthesis and processing;

Modeling;

Characterization and properties (mechanical and transport properties of nanostructured materials, high- and low-current properties of superconducting materials);

Applications.

**Workshop venue:** Palace of Scientists, St.Petersburg, Russia

**International Organizing Committee:**

R.Masumura (Naval Research Laboratory, USA)

I.Ovid'ko (Russian Academy of Sciences, Russia)

C.Pande (Naval Research Laboratory, USA)

B.Smirnov (Russian Academy of Sciences, Russia)

M.Soto (Office of the US Naval Research, USA)

**Contacts:**

Dr.Ilya Ovid'ko  
Institute of Problems of Mechanical Engineering,  
Russian Academy of Sciences  
Bolshoj 61, Vas.Ostrov, St.Petersburg 199178, Russia  
Phone: +(7 812)321 4764  
Fax: +(7 812)321 4771  
E-mail: [ovidko@def.ipme.ru](mailto:ovidko@def.ipme.ru)

Accommodation and Excursions:

Mrs.Dina Grigorieva  
E-mail: [n\\_grigorieva@hotmail.com](mailto:n_grigorieva@hotmail.com)

**Preliminary list of AAIS participants**

Prof.R.A.Andrievskii (Institute of Chemical Problems, Russia)

Dr.U.Balachandran (Argonne National Laboratory, USA)

Prof.N.Browning (University of Illinois at Chicago, USA)

Prof..Chow (National University of Singapore, Singapore)

Dr.J.Eastman (Argonne National Laboratory, USA)

Dr.K.Goretta (Argonne National Laboratory, USA)

Prof.Y.Gogotsi (University of Illinois at Chicago, USA)

Dr.P.Hazzledine (Universal Energy System, USA)

Dr.P. Jena (Virginia Commonwealth University, USA)

Prof.G.Kiriakidis (IESL/FORTH, Greece)

Prof.J.-Y.Laval (CNRS/ESPCI, France)

Dr.R.A.Masumura (Naval Research Laboratory, USA)

Dr.T.Orlova (Ioffe Physico-Technical Institute, Russia):

Dr. I.Ovid'ko (Institute of Problems of Mechanical Engineering, Russia)

# REPORT DOCUMENTATION PAGE

Form Approved OMB No. 0704-0188

Public reporting burden for this collection of information is estimated to average 1 hour per response, including the time for reviewing instructions, searching existing data sources, gathering and maintaining the data needed, and completing and reviewing the collection of information. Send comments regarding this burden estimate or any other aspect of this collection of information, including suggestions for reducing this burden to Washington Headquarters Services, Directorate for Information Operations and Reports, 1215 Jefferson Davis Highway, Suite 1204, Arlington, VA 22202-4302, and to the Office of Management and Budget, Paperwork Reduction Project (0704-0188), Washington, DC 20503.

1. AGENCY USE ONLY (Leave blank)	2. REPORT DATE	3. REPORT TYPE AND DATES COVERED	
	September 1999	11-24 September 1999 Final Report	
4. TITLE AND SUBTITLE		5. FUNDING NUMBERS	
International Workshop on Applied Aspects of Interface Science. September 22-24, 1999. St. Petersburg, Russia.		N000-99-1-	
6. AUTHOR(S)			
Multiple			
7. PERFORMING ORGANIZATION NAME(S) AND ADDRESS(ES)		8. PERFORMING ORGANIZATION REPORT NUMBER	
Institute of Problems of Mechanical Engineering Russian Academy of Sciences Boshoi 61, Vas. Ostrov St. Petersburg 199178 Russia		ISSN 1605-2730	
9. SPONSORING/MONITORING AGENCY NAME(S) AND ADDRESS(ES)		10. SPONSORING/MONITORING AGENCY REPORT NUMBER	
Office of Naval Research] European Office PSC 802 Box 39 FPO AE 09499-0039			
11. SUPPLEMENTARY NOTES			
Published in Materials Physics and Mechanics, Vol. 1, No.1 (March 2000). This work relates to Department of the Navy Grant issued by the Office of Naval Research International Field Office. The United States has a royalty free license throughout the world in all copyrightable material contained herein.			
12a. DISTRIBUTION/AVAILABILITY STATEMENT		12b. DISTRIBUTION CODE	
Approved for Public Release; Distribution Unlimited. U.S. Government Rights License. All other rights reserved by the copyright holder.		A	
12. ABSTRACT (Maximum 200 words)			
This volume is a collection of selected original papers presented at the International Workshop on Applied Aspects of Interfaces Science held at the Palace of Scientists, St. Petersburg, Russia, September 22-24, 1999. The workshop objective was to present current research on advanced nanostructured materials and high temperature superconducting materials characterized by nano-scaled coherence length. Focus was placed synthesis and processing, modeling, characterization and properties, and applications. A total of 33 scientists from 8 countries participated. Particular emphasis was placed on fostering future collaborations among scientists and engineers from Russia, the USA and other countries.			
13. SUBJECT TERMS		15. NUMBER OF PAGES	
Materials science, Nanotechnology, Foreign reports			
		16. PRICE CODE	
17. SECURITY CLASSIFICATION OF REPORT	18. SECURITY CLASSIFICATION OF THIS PAGE	19. SECURITY CLASSIFICATION OF ABSTRACT	20. LIMITATION OF ABSTRACT
UNCLASSIFIED	UNCLASSIFIED	UNCLASSIFIED	UL

## CONTENTS

<b>New Journal – Reviews on Advanced Materials Science .....</b>	<b>A4</b>
<b>Introductionary Article .....</b>	<b>A5</b>
<b>Preface .....</b>	<b>A6</b>
<b>AC Magnetic Properties of Compacted FeCo Nanocomposites .....</b>	<b>1</b>
A.K. Giri, K.M. Chowdary and S.A. Majetich	
<b>Nanostructured Ni films by Polyol Electroless Deposition .....</b>	<b>11</b>
J. Zhang, G.M. Chow, S. H. Lawrence and C.R. Feng	
<b>Heteroepitaxial Growth of InAs on Si: the New Type of Quantum Dots .....</b>	<b>15</b>
G.E. Cirlin, N.K. Polyakov, V.N. Petrov, V.A. Egorov, D.V. Denisov, B.V. Volovik, V.M. Ustinov, Zh.I. Alferov, N.N. Ledentsov, R. Heitz, D. Bimberg, N.D. Zakharov, P. Werner and U.G. Osele	
<b>Fabrication of 2-D and 3-D Photonic Band-Gap Crystals in the GHz and THz Regions .....</b>	<b>20</b>
G. Kiriakidis and N. Katsarakis	
<b>A Mathematical Model of Metal Film Deposition from Photoactive Compound Solutions on Solid-Liquid Interface .....</b>	<b>27</b>
S.A. Kukushkin and S.V. Nemenat	
<b>Enhanced Diffusion near Amorphous Grain Boundaries in Nanocrystalline and Polycrystalline Solids .....</b>	<b>31</b>
R.A. Masumura and I.A. Ovid'ko	
<b>Correlation Between Superconducting Transport Properties and Grain Boundary Microstructure in High-Tc Superconducting Ceramics .....</b>	<b>39</b>
T.S. Orlova, J.Y. Laval and B.I. Smirnov	
<b>Modeling of Size Effect on Dielectric Response of Thin Ferroelectric Films .....</b>	<b>45</b>
O.G. Vendik and S.P. Zubko	
<b>Critical Current Density in Polycrystalline High-Tc Superconductors with Disordered Tilt Boundaries .....</b>	<b>49</b>
S.A. Kukushkin, A.V. Osipov and I.A. Ovid'ko	
<b>TEM and STM Investigations on the Disclination Nature of Fragment Boundary Triple Junctions .....</b>	<b>54</b>
M. Seefeldt	
<b>Symposium Information .....</b>	<b>A7</b>
<b>Copyright Transfer Form .....</b>	<b>A8</b>

## NEW JOURNAL

### REVIEWS ON ADVANCED MATERIALS SCIENCE

Commencing publication with the April 2000 issue, the new journal "Reviews on Advanced Materials Science" provides an international medium for the publication of reviews in the area of theoretical and experimental studies of advanced materials. Focuses are placed on nanostructured materials, high-transition-temperature superconductors, and high-melting point compounds.

Audience:

Materials Scientists, Physicists, Metallurgists, Mechanical Engineers, Ceramists

Principal Editor:

**I.A. Ovid'ko**, Institute of Problems of Mechanical Engineering, Russian Academy of Sciences, Bolshoj 61, Vas.Ostrov, St.Petersburg 199178, Russia

International Editorial Board:

**V.P.Bulatov**, Russian Academy of Sciences (Russia); **G.-M.Chow**, National University of Singapore (Singapore); **Y.G.Gogotsi**, University of Illinois at Chicago (USA); **P.Jena**, Virginia Commonwealth University (USA); **L.Kabacoff**, Office of Naval Research(USA); **C.S.Pande**, Naval Research Laboratory (USA); **H.-E.Schaefer**, Stuttgart University (Germany); **R.D.Shull**, National Institute of Standards and Technology (USA); **B.I.Smirnov**, Russian Academy of Sciences (Russia); **M.Soto**, Office of Naval Research (USA); **R.A.Suris**, Russian Academy of Sciences (Russia); **A.Tholen**, Chalmers Laboratory (Sweden); **Y.F.Titovets**, St.Petersburg State Technical University (Russia); **T.Tsakalakos**, Rutgers University (USA); **D.Wolf**, Argonne National Laboratory (USA).

Prospective authors are encouraged to correspond with the principal editor before submitting an article. Proposals should include an outline with key citations. All papers submitted will be rigorously peer-reviewed prior to publication.

#### Postal Address:

Reviews on Advanced Materials Science  
Editorial Office

Institute of Problems of Mechanical Engineering  
Russian Academy of Sciences  
Bolshoj 61, Vas.Ostrov, St.Petersburg, 199178, Russia

Fax: +(7 812)321 4771

E-mail: rams@def.ipme.ru

Web-sites: <http://www.ipme.ru/e-journals/RAMS/>  
<http://www.ipme.nw.ru/e-journals/RAMS/>  
<http://mclab.me.uic.edu/RAMS>

## **INTRODUCTIONARY ARTICLE**

Dear Colleagues,

We would like to introduce you to the journal «Materials Physics and Mechanics», which is launched this year by Institute of Problems of Mechanical Engineering (Russian Academy of Sciences, St.Petersburg, Russia) and Advanced Study Center Co.Ltd. (St.Petersburg, Russia).

If any one technology can be said to shape the face of today society, it is materials technology. New materials, materials processes and applications are of major importance in boosting many high technological sectors. As discussions and intererst in materials science and technology grow, the journal “Materials Physics and Mechanics” will became the place to disseminate knowledge of the physical and mechanical phenomena and processes in materials.

The journal specializes in the rapid publication of international conference proceedings in every area of materials physics and mechanics. All papers will be subject to rigourous peer review.

The editors of the journal “Materials Physics and Mechanics” look forward to receiving your comments and contributions to the journal.

Have a useful enjoyable read!

Yours sincerely,

Vladimir Bulatov  
Principal Editor

and

Ilya Ovid'ko  
Principal Editor

## **PREFACE**

This volume is a collection of selected original papers presented at the International Workshop on Applied Aspects of Interfaces Science (St.Petersburg, Russia, September 22-24, 1999). The workshop successfully provided a critical, up-to-date tutorial review and discussion on applied science of nanostructured materials and polycrystalline high-T<sub>c</sub> superconductors. Focuses were placed on synthesis, processing, characterization, properties, and applications of nanostructured materials and polycrystalline superconductors. A total of 33 scientists from 8 countries (Belgium, France, Germany, Russia, Singapore, South Africa, UK, USA) participated in the workshop, making it a really international event.

About equal number of papers in this volume cover theoretical and experimental research in the area of interface science. All papers have been peer-reviewed prior to publication.

Support of the workshop from the Office of the US Naval Research, International Field Office, Europe; the European Office of the US Aerospace Research and Development, UK; and the European Research Office of the US Army, UK is greatly appreciated. Administrative support of the Institute of Problems of Mechanical Engineering (Russian Academy of Sciences, St.Petersburg, Russia) is also acknowledged.

Ilya Ovid'ko  
Chairman, Organizing Committee

# AC MAGNETIC PROPERTIES OF COMPACTED FeCo NANOCOMPOSITES

Anit K. Giri, Krishna M. Chowdary and Sara A. Majetich

Department of Physics, Carnegie Mellon University  
Pittsburgh, PA 15213-3890, USA

Received: September 23, 1999

**Abstract.** Here we report the AC magnetic properties of soft magnetic nanocomposites made from compaction of  $Fe_{10}Co_{90}$  nanoparticles. Following a discussion of previous work on soft magnetic nanocomposites, the sample preparation and experimental characterization by AC permeametry are described. The permeability is constant and equal to the DC value for low frequencies, but drops off sharply above a characteristic frequency  $f_c$ . A model is developed to explore the relation between  $f_c$  and material parameters including the effective anisotropy, exchange coupled volume, temperature, and saturation magnetization.

## 1. INTRODUCTION

Many recent developments in soft magnets, which are used in power applications, have been based on amorphous and nanocrystalline materials [1-5]. In amorphous solids the magnetocrystalline anisotropy  $K$  is by definition equal to zero, eliminating the main material-dependent contribution to the coercivity. The effective anisotropy  $K_{eff}$  can also be low in nanocrystalline materials if conditions specified by the Random Anisotropy Model are met [1-3, 6]. The grain size must be smaller than the magnetic exchange length  $L_{ex}$ , and the grains must be exchange coupled with their easy axes for magnetization randomly oriented. The combination of random orientation and averaging over multiple grains makes the preference for magnetization in a particular direction, and therefore  $K_{eff}$  very small. Theoretically, low  $K$  materials become even softer if the grain size  $D$  is small enough. The DC magnetic properties of nanocomposites have been modeled in terms of the Random Anisotropy Model [1-3]. The magnetization reversal field or coercivity  $H_c$  is predicted to be proportional to  $D^6$ , while the permeability  $\mu=B/H$  is predicted to be proportional to  $D^{-6}$ . Here we extend this approach to understand the AC magnetic properties of nanocomposites.

Previous work on the AC magnetic properties of bulk magnetic materials has shown that the permeability can be split into in-phase ( $\mu'$ ) and out-of-phase

( $\mu''$ ) components, just like the permittivity of dielectric materials:

$$\mu = \mu' - i\mu'' \quad (1)$$

These components obey a Kramers-Krönig relationship [7], so that by knowing the value of one for all frequencies, the other is uniquely determined. The real part  $\mu'$  is typically flat up to a cutoff frequency, and then drops off, while the imaginary part  $\mu''$  shows a peak at the same frequency. In the best high frequency ferrite materials, the cutoff frequency is in the GHz range, and is associated with the precession frequency of spins about the applied magnetic field. While high frequency magnetic materials are highly insulating to reduce eddy current losses, their properties have not been analyzed in terms of their microstructure.

A benchmark for soft magnetic materials is the total power loss,  $P_{tot}$ , as the material is magnetized and demagnetized. It depends on the hysteresis loss, losses due to the eddy currents created by the changing magnetic field, and anomalous losses associated with domain wall motion [8]. These contributions have different frequency dependencies:

$$P_{tot} = P_{hys} + P_{eddy\ current} + P_{anom} = \\ W_{hys} f + A f^2 / \rho + P_{anom}(f) \quad (2)$$

$P_{hys}$  varies linearly with the frequency  $f$  and the area within the hysteresis curve  $W_{hys}$ .  $P_{eddy\ current}$  is quadratic

in frequency and inversely proportional to the resistivity  $\rho$ .  $A$  is a constant. The anomalous loss  $P_{\text{anom}}$  has no fixed power law dependence on the frequency.

The AC magnetic properties of ferrofluids, which are small ( $< 10$  nm) magnetic particles dispersed in a liquid, show distinctly different behavior from that of bulk materials. There are two characteristic relaxation times, one due to Brownian relaxation caused by rotation of the particles in the liquid, and the other due to Néel relaxation caused by coherent rotation of the atomic spins within the particle [9, 10]. Both processes occur at frequencies well below the Larmor frequency  $f_o$ .

Nanocomposites have potential for two niche applications of soft magnetic materials. In low frequency applications, amorphous materials should continue to dominate, since they have the smallest hysteretic losses. Without significant eddy currents, only the small percentage of atoms required for glass forming do not contribute to the magnetization. However, at higher temperatures amorphous materials crystallize. In the current nanocrystalline materials [1-5], grain growth is limited by precipitation of additional phases, and a larger fraction of nonmagnetic atoms is needed. At higher frequencies, nanocomposites have potential advantages because they can have higher resistivity to reduce eddy current losses. While ferrites are currently used for high frequency applications because of their high resistivities, they have much lower magnetizations than iron-based alloys.

Iron-cobalt alloys are of interest for high temperature soft magnets because they have a high Curie temperature, high magnetization, and low coercivity. The value of the Curie temperature depends on the relative Co abundance. Iron-cobalt alloys have the largest magnetic moment per atom, and therefore large saturation magnetizations [11]. They have a low coercivity due to the low magnetocrystalline anisotropy  $K$  of the body-centered cubic structure. There is a zero crossing of the anisotropy near the equiatomic composition [12].

We investigate nanolaminates formed by compaction of FeCo nanoparticles with a very thin coating of a protective carbon or oxide. By choosing a particle or grain diameter well below the maximum monodomain size, the coercivity and hysteretic power losses can be minimized [1-3]. The coatings act as a barrier to eddy currents, reducing the eddy current power losses at high frequency. The goals are to minimize the portion of nonmagnetic atoms while retaining a stable nanocrystalline structure at high temperature, and to determine the degree of coating which retains significant exchange coupling for minimum  $K_{\text{eff}}$  while creating significant barriers to eddy currents.

## 2. EXPERIMENTAL

**Particle Synthesis.** Here the alloy nanoparticles were synthesized by the polyol method [13], a chemical route which leads to highly monodisperse metal particles. Iron chloride tetrahydrate and sodium hydroxide were dissolved in ethylene glycol and heated to 110 °C while stirring. A second solution of cobalt hydroxide in ethylene glycol at the same temperature was added, and the mixture was heated to 195 °C, where a precipitate formed. The total metal ion concentration was 0.2 M, and the hydroxide concentration was 2.0 M. Water and other reaction products were distilled off, and the solvent was refluxed for one hour at the maximum temperature. The precipitate was thoroughly washed with methanol, and dried.

While the particle size can be varied by changing the metal salt concentration and reaction time, the average grain diameter was roughly constant and approximately 20 nm. The composition was determined from electron energy loss spectroscopy [14]. The average grain size was obtained from Scherrer analysis of the x-ray diffraction peaks, and the particle size was found from transmission electron microscopy. The exchange length in magnetically soft materials like FeCo is large, and here is comparable to the grain size. Adjacent grains can then be exchange coupled to each other, leading to a further reduction in the anisotropy and coercivity, as explained by the random anisotropy model [1-3, 6].

**Compaction.** A nanocomposite has nanoparticle-sized grains, which may be dispersed in a matrix that mediates their coupling. The coupling strength depends on the magnetic behavior of the matrix and on the degree of coherence at the interface between the nanoparticles and the matrix. Exchange interactions may couple nanoparticles together. We worked with Dr. S. Sudarshan and Mr. Sang Yoo of Materials Modification, Inc., on plasma pressure compaction, which has the advantage of being able to reduce or remove the thin coating surrounding FeCo nanoparticles under ambient conditions. Powders were compacted by a combination of pressure and an electric arc in a two stage process. First a voltage pulse established a continuous current path across the sample in a graphite mold under a pressure of 10 MPa. This generated a plasma in the voids, and partly removed surface impurities such as oxides. In the second stage a continuous current path led to resistive sintering. The pressure was increased to 70 MPa to deform and compact the particles. The entire process required only a few minutes, thereby limiting grain growth. The resistive heating concentrated in the “necks” forming as the particles sinter, making them deform more

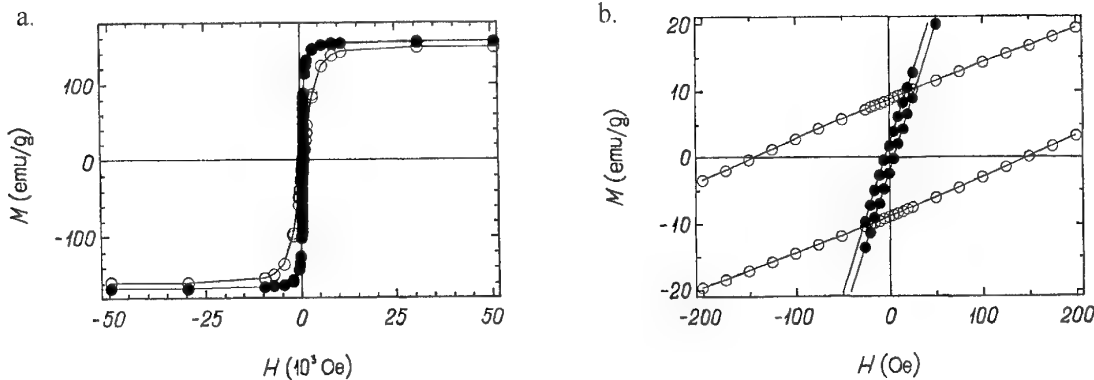


**Fig. 1.** a.) Comparison of  $\text{Fe}_{10}\text{Co}_{90}$  nanoparticles made by the polyol method (open circles), and a compact made from them (filled circles); b.) An expanded region shows the coercivity of the pellet is on the order of 5 Oe, much less than that of the precursor particles, which is approximately 150 Oe.

readily. Compacts with over 90% theoretical density were made from the nanoparticle powders.

**Magnetic Properties.** There was a substantial amount of magnetic characterization, including SQUID magnetometry (with a Quantum Design MPMS) to determine the coercivity, and AC permeametry (with a Walker Scientific AC Hysteresisgraph) on toroidal compacts to measure the frequency dependence of the permeability  $m$  and the power loss. For the AC measurements, the toroid outer diameter was 2.54 cm, and it had a square cross section with dimensions  $3.0 \times 4.1$  mm. There were 154 primary turns and 11 turns in the pickup coil. The amplitude of the AC magnetic field applied was 125 Oe, and the frequency ranged from 100 to 100,000 Hz. The temperature of the toroid was controlled by placing it in thermal contact with an ice bath ( $0^\circ\text{C}$ ), or with it inserted in a furnace ( $100^\circ\text{C} - 500^\circ\text{C}$ ). At elevated temperatures the coils were sheathed with fiberglass sleeving (Omega Engineering, Inc.).

### 3. EXPERIMENTAL RESULTS

Fig. 1 shows a comparison of the DC hysteresis loops for the powder and compacted pellet of a typical sample. Compaction significantly reduces the coercivity, indicating that the exchange coupling is increased, as predicted by the random anisotropy model.

The AC hysteresis loops were measured for toroids cut from the same compressed pellets, for a range of frequencies. With AC excitation, the pickup loop measures the magnetic induction  $B = 4\pi M \cdot H$ . Fig. 2 illustrates the characteristic behavior as a function of frequency. At low frequencies (Fig. 2a) the applied field  $H$  was sufficient to saturate the sample, reaching the single-valued region of  $B(H)$ . As the frequency was raised, the width of the hysteresis loop and therefore the coercivity increased, but the maximum induction remained approximately the same, up to a characteristic

frequency (Fig. 2b). Approaching this frequency, the sample was no longer saturated at the maximum applied field, and the maximum magnetic induction dropped (Fig. 2c).

The permeability as a function of the maximum applied field is illustrated in Fig. 3, for several representative frequencies. Defining the permeability as the maximum value of  $B/H$ , it is expected to vary depending on the magnitude of  $H_{\max}$ . If  $H_{\max}$  is small and the sample is not saturated,  $B$  increases approximately linearly with  $H$ , and  $\mu$  is large. If  $H_{\max}$  is large and the sample is never saturated,  $B$  increases more slowly with increasing  $H$  and  $\mu$  is reduced. In order to understand the fundamental physics of the AC excitation of the nanocomposites, a value of  $H_{\max} = 125$  Oe was selected for further measurements so that the samples were saturated at low frequency.

Several important quantities for soft magnetic materials were measured as a function of frequency. The real (in-phase) and imaginary (out-of-phase) parts of the permeability  $\mu = B/H$  were also measured as a function of frequency (Fig. 4). In the low frequency range, the phase lag between  $B$  and  $H$  is small, and  $\mu''$  is negligible.  $\mu'$  is roughly constant up to the characteristic frequency, where it drops off sharply.  $\mu''$  peaks as  $\mu'$  drops off, and the critical frequency  $f_c$  is determined from the position of the peak in  $\mu''$ . The characteristic frequency of the permeability varied with temperature (Fig. 5). While the low frequency magnitude of  $m$  dropped off slightly with increasing temperature, due to a reduction in the magnetization,  $f_c$  rose substantially, from 1400 Hz at  $0^\circ\text{C}$  to 6000 Hz at  $500^\circ\text{C}$ . As noted in the hysteresis loops, the coercivity rose with increasing frequency (Fig. 6). It peaked at a frequency approximately 2-3 times  $f_c$ , and decreased somewhat at high frequencies. The overall power loss per cycle is shown in Fig. 7. At low frequencies it rises linearly, as expected from Eq. 2 if hysteretic losses are dominant.

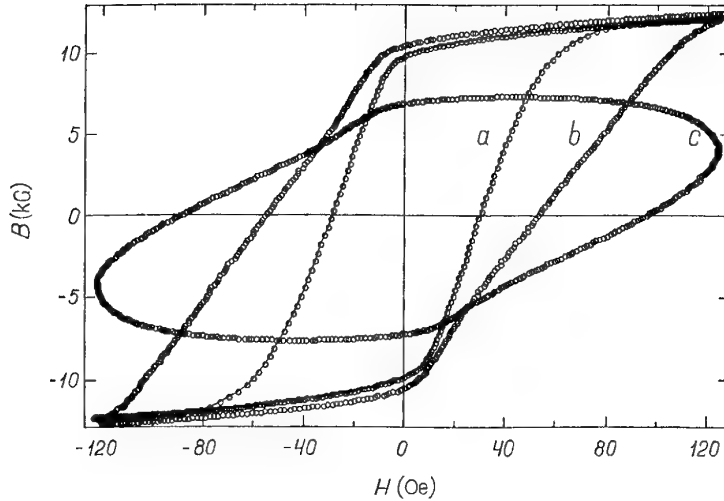


Fig. 2. AC Hysteresis loops for Fe<sub>10</sub>Co<sub>90</sub>, at 0 °C. a.) 100 Hz, b.) 800 Hz, c.) 5000 Hz.

At frequencies above  $f_c$  a weaker dependence is observed, closer to  $f^{0.5}$ . As the temperature is increased the power loss per cycle decreases somewhat, due mainly to the reduction in the coercivity.

#### 4. MODEL OF AC MAGNETIC PROPERTIES

Our model of the AC properties of nanocomposites is based on a monodomain magnetic particle in an oscillating magnetic field. For a uniaxial particle with the applied field parallel to the easy axis, the energy  $E$  is given by

$$E = KV \sin^2 \theta - M_s H \cos \theta, \quad (3)$$

where  $K$  is the magnetocrystalline anisotropy,  $V$  is the particle volume,  $\theta$  is the angle between the magnetization direction and the applied field  $H$ , and  $M_s$  is the saturation magnetization. Stoner-Wohlfarth theory [15-17] has shown that energy minima occur at  $\theta = 0^\circ$  or  $180^\circ$ , and a maximum exists where  $\cos \theta = -HM_s/2K$ .

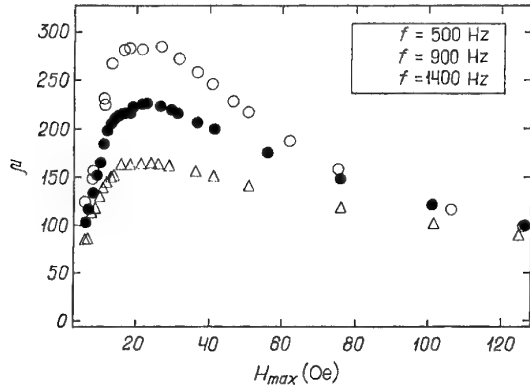


Fig. 3. Overall permeability for Fe<sub>10</sub>Co<sub>90</sub>, as a function of  $H_{max}$ , at 0 °C, for 500, 900, and 1400 Hz. The peak permeability at 22 Oe reflects where the slope of the  $B(H)$  starts to decrease.

In order to reverse the magnetization direction, the energy barrier must be overcome. If this does not occur within the measurement time, then hysteresis is observed. The rate of going over the barrier  $\tau_0^{-1}$  is given by

$$\tau_0^{-1} = \tau_0^{-1} \exp\left(-\frac{\Delta E}{kT}\right), \quad (4)$$

where  $\tau_0^{-1} = f_0$  is the Larmor frequency,  $\Delta E$  is the magnitude of the energy barrier,  $k$  is the Boltzmann constant, and  $T$  is the temperature.

If the magnetic field oscillates in time,  $H(t) = H_0 \cos(2\pi ft)$ , then the positions of the energy minima and maxima will also change with time, as shown in Fig. 8. Early in the cycle state 1 is the global minimum and state 2 is a local minimum, but later the roles are reversed. The height of the energy barrier which must be over-

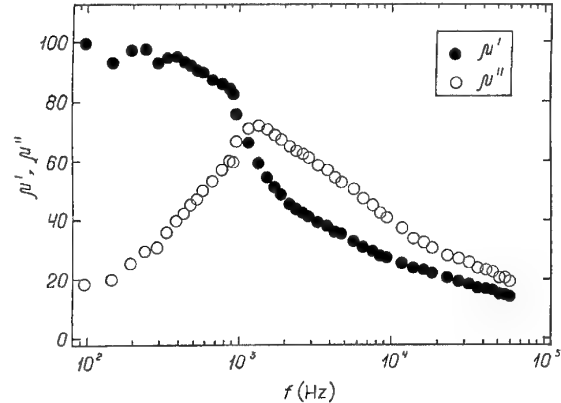


Fig. 4. The real ( $\mu'$ ) and imaginary ( $\mu''$ ) parts of the permeability for Fe<sub>10</sub>Co<sub>90</sub>, at 0 °C, as a function of frequency.

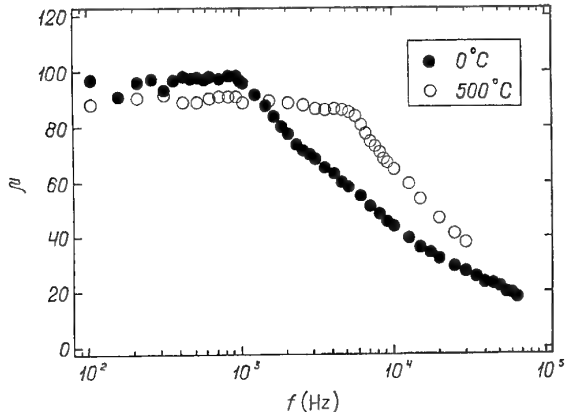


Fig. 5. Overall permeability as a function of frequency for  $\text{Fe}_{10}\text{Co}_{90}$ , at 0 °C and 500 °C.

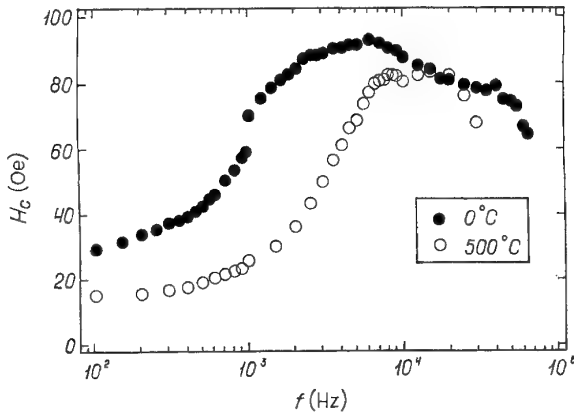


Fig. 6. Coercivity as a function of frequency for  $\text{Fe}_{10}\text{Co}_{90}$ , at 0 °C and 500 °C.

come for the particle to switch from the local to the global minimum also oscillates in time and is greatest at zero applied field.

Given an ensemble of particles and monitoring the population  $N_1$  in state 1 and  $N_2$  in state 2 as a function of time, the magnetization can be determined:

$$M(t) = M_s(N_1(t) - N_2(t)) = M_s(2N_1(t) - 1). \quad (6)$$

Here we assume that population is conserved, and that at all times

$$N_1 + N_2 = 1. \quad (7)$$

The population in state 1 as a function of time depends on the rate  $\tau_{bkw}^{-1}$  at which particles get over the barrier from state 2, and on the rate  $\tau_{fwd}^{-1}$  that they leave state 1 in the forward direction over the barrier:

$$\frac{dN_1}{dt} = -\frac{dN_2}{dt} = \tau_{bkw}^{-1}N_2 - \tau_{fwd}^{-1}N_1. \quad (8)$$

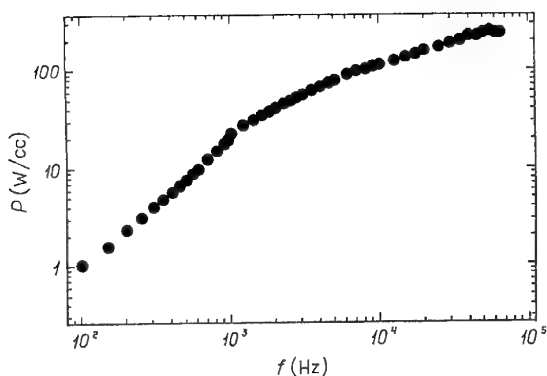


Fig. 7. Power Loss per unit volume as a function of frequency for  $\text{Fe}_{10}\text{Co}_{90}$ , at 0 °C.

Substituting for the rates using Eq. 4,

$$\frac{dN_1}{dt} = \tau_0^{-1} \left[ (1 - N_1) \exp\left(\frac{-\Delta E_{bkw}}{kT}\right) - N_1 \exp\left(\frac{-\Delta E_{fwd}}{kT}\right) \right]. \quad (9)$$

Substituting for the forward  $\Delta E_{fwd}$  and reverse  $\Delta E_{bkw}$  energy barriers,

$$\Delta E_{fwd} = E_{max} - E_1 = KV \left[ 1 + \frac{HM_s}{2K} \right]^2 \quad (10a)$$

$$\Delta E_{bkw} = E_{max} - E_1 = KV \left[ 1 + \frac{HM_s}{2K} \right]^2 \quad (10b)$$

the differential equation becomes

$$\frac{dN_1}{dT} = \tau_0^{-1} \left[ (1 - N_1) \exp\left(\frac{-KV}{kT} \left[ 1 + \frac{HM_s}{2K} \right]^2\right) - N_1 \exp\left(\frac{-KV}{kT} \left[ 1 + \frac{HM_s}{2K} \right]^2\right) \right]. \quad (11)$$

In an oscillating magnetic field  $H(t)$ , Eq. 11 must in general be solved numerically.

This problem has many similarities to that of an electric dipole in an AC electric field, which was originally solved by Peter Debye [18,19], with two main differences. In the electric dipole model, there was no equivalent to magnetocrystalline anisotropy, so the solution corresponds to the superparamagnetic limit. Also, in the electric dipole model, the factor equivalent to  $x = M_s VH/kT$  is much less than one, and when  $e^x$  is approximated by  $1+x$ , the equation corresponding to Eq. 11 can be solved analytically.

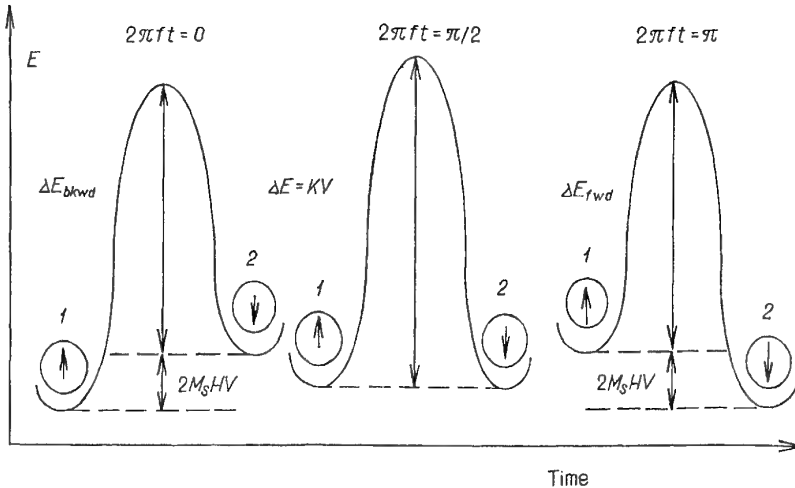


**Fig. 8.** Energy levels as a function of time, for different parts of the cycle of  $H(t)$ . Here  $E_1$  is the energy of a particle in state 1,  $E_2$  is the energy of a particle in state 2, and  $\Delta E$  is the magnitude of the barrier between the local minimum and the maximum energy states.

Equation 11 can be solved analytically in the limit of large  $K$ , where  $\Delta E_{fwd} \approx \Delta E_{bkwd}$ . With the substitution

$$y = \frac{KV}{kT} \quad (12)$$

Eq. 11 then simplifies to

$$\frac{dN_1}{dt} \approx \tau_0^{-1} e^{-y} (1 - 2N_1). \quad (13)$$

The solution to Eq. 13 is given by

$$N_1(t) = \frac{1}{2} \left[ 1 + \exp(-2\tau_0^{-1} y t) \right]. \quad (14)$$

There will be a characteristic or resonant frequency  $f_c$ , where

$$f_c = \frac{\tau_0^{-1} e^{-y}}{\pi} = \left( \frac{\tau_0^{-1}}{\pi} \right) \exp\left( \frac{-KV}{kT} \right), \quad (15)$$

where the population oscillates in resonance with the driving field  $H(t)$ . Above this frequency, the population shifts cannot keep up with the rapidly changing driving field.

The model breaks down for cases where  $HM_s/2K > 1$ , since this requires that  $|\cos\theta| = -HM_s/2K$  be greater than one. To investigate the small  $K$  limit, which is of critical importance for soft magnetic materials, we reduced the amplitude of the magnetic field  $H_0$  where necessary. In experiments it is possible to have large amplitudes of the AC magnetic field when studying materials with very low anisotropy. Here the sample is being driven past the high slope portion of the hysteresis

curve during each half-cycle. In applications of soft magnetic materials, this is undesirable since the permeability  $\mu = B/H$  is reduced. Therefore the model can be used to understand the AC magnetic behavior in situations of greatest technological importance.

## 5. MODELING RESULTS AND COMPARISON WITH EXPERIMENT

The simulation results show the same characteristics as the experimental data, and provide insight about the mechanism responsible for the frequency dependent behavior.

Fig. 9 illustrates the connection between the time-dependence of  $M$  and the  $B(H)$  curves for driving fields of different frequencies  $H = H_0 \cos(2\pi ft)$ . If the frequency is low enough (Fig. 9a) the sample has time to equilibrate with the slowly varying field and superparamagnetism is observed. There is a negligible phase lag  $\theta$  between  $M(t)$  and  $H(t)$ . Because of this  $M(t)$  reaches its maximum value well below the maximum amplitude of the driving field  $H_0$ . At somewhat higher frequencies  $M(t)$  starts to lag behind  $H(t)$  significantly, leading to hysteresis (Fig. 9b). However  $M(t)$  still reaches its maximum value before  $H(t)$  starts to decrease. At the critical frequency  $f_c$  this is no longer true (Fig. 9c), and the shape of  $M(t)$  and the hysteresis loop change noticeably.  $B(H)$  no longer contains single valued regions, and the maximum value of  $B$  starts to decrease relative to its value at lower frequencies. At the highest frequencies  $M(t)$  and  $B(H)$  are almost completely out of phase and the maximum values of  $M(t)$  and  $B(H)$  are very small (Fig. 9d). The model simulates characteristics of the experimental results shown in Fig. 2, and shows that the shape and magnitude of

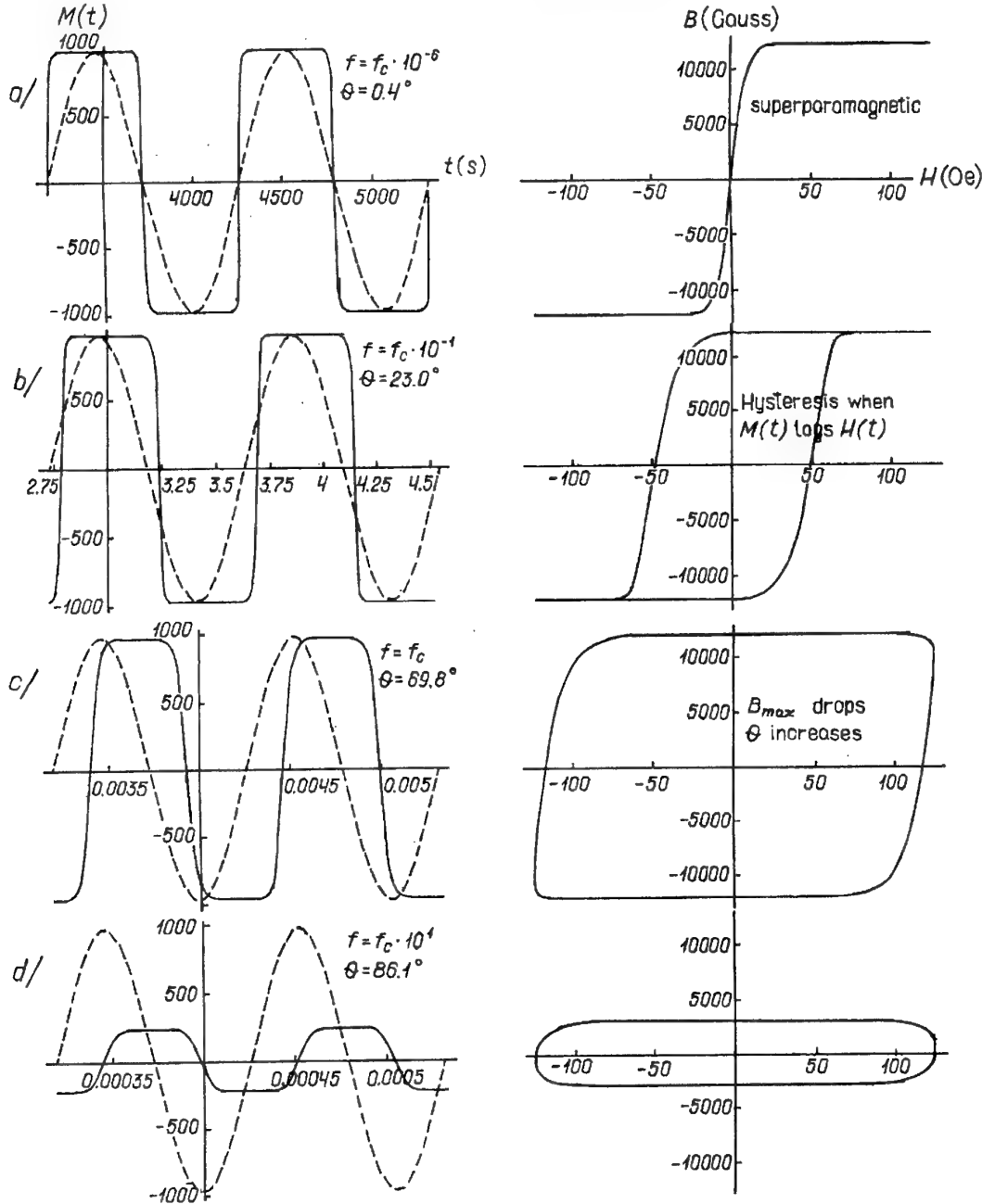


Fig. 9.  $M(t)$  and  $H(t)$ , and the corresponding  $B(H)$  curves for a sphere of exchange coupled volume  $V$  and effective anisotropy  $K$ . a.) for a superparamagnetic particle, b.) for a monodomain but not superparamagnetic particle at low frequency  $f$ , c.) at med.  $f$ , and d.) at high  $f$ . Note that in a.) and b.)  $B(H)$  appears to saturate, but this is because  $4\pi M$  is so much larger than  $H$ . These simulations used the following parameters:  $M_s = 1000$  emu/cc,  $H_0 = 125$  Oe,  $K = 1.95 \cdot 10^5$  erg/cc,  $T = 273$  K, and  $V = 1.47 \cdot 10^{-18}$  cc. The critical frequency  $f_c$  was 1400 Hz.

$B(H)$  depend on whether the magnetization of the exchange coupled volume within the sample can equilibrate with the changing external magnetic field.

Figure 10 shows the corresponding trend in the permeability  $\mu$  as a function of frequency. At low frequencies it is constant and equal to the DC value, but as soon as  $M(t)$  is unable to reach its maximum value,  $B_{max}$  and therefore  $\mu$  begin to drop, approaching zero

in the high frequency limit. This is in contrast to the experimental results shown in Fig. 5, where  $\mu$  decays more slowly. Such a difference would arise if the sample contained a distribution of characteristic frequencies  $f_c$ , perhaps related to a distribution of grain sizes.

Fig. 11 reveals the behavior of the simulated coercivity as a function of frequency. At low frequencies it follows Sharrock's Law [20]:

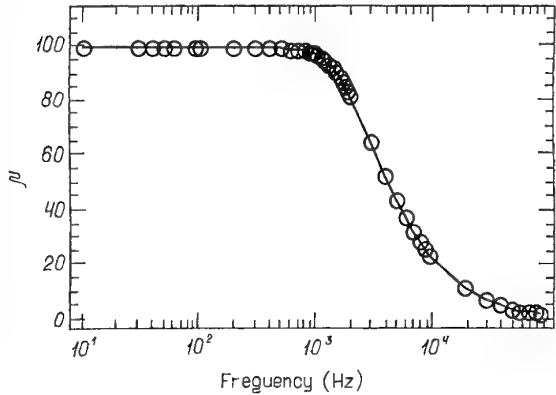


Fig. 10. The permeability  $\mu = B_{max}/H_{max}$  as a function of frequency, for the same parameters as in Fig. 9.

$$H_c(f) = \left( \frac{2K}{M_s} \right) \left[ 1 - \left( \frac{kT \ln(f_0/f)}{KV} \right)^{1/2} \right], \quad (16a)$$

or

$$H_c(f) = \left( \frac{2K}{M_s} \right) \left[ 1 - \left( \frac{kT}{KV} \right)^{1/2} \left( \frac{1}{2} \right) \ln f_0 \right] + \left( \frac{2K}{M_s} \right) \left[ \left( \frac{kT}{KV} \right)^{1/2} \left( \frac{1}{2} \right) \ln f_0 \right] \quad (16b)$$

rising with the log of the frequency. The peak in  $H_c$  occurs between two and three times  $f_c$ , and then  $H_c$  begins to decrease. This occurs when the magnetization due to the driving field is low enough, and the value of  $H(t)$  needed to make  $M(t)$  equal to zero is reduced. The experimental coercivity shown in Fig. 6 also rises and peaks at roughly the same frequency, but the rise is not proportional to  $\ln f$ . While there may be a region where  $H_c$  obeys this functional dependence, there appears to be a low frequency contribution to the coercivity from a factor not included in the model. This could arise from particles not exchange coupled to their neighbors, possibly from a thicker coating.

Fig. 12 shows the hysteretic power loss  $P_{hys}$  found from the area of the hysteresis loop  $B(H)$ , as a function of frequency. This rises linearly at low frequencies, as expected from Eq. 2, but then it levels off at  $f_c$ . At very high frequency it should decrease when both  $M_{max}$  and  $H_c$  are decreasing.

In comparison, Fig. 7 shows the total experimental power loss. At frequencies below  $f_c$ , hysteretic power losses dominate. This is expected for frequencies below 10,000 Hz.

The qualitative behavior illustrated in Fig. 9-12 is similar for a wide range of input parameters; only the magnitudes of  $\mu$ ,  $H_c$  and  $P_{hys}$  vary, along with the critical

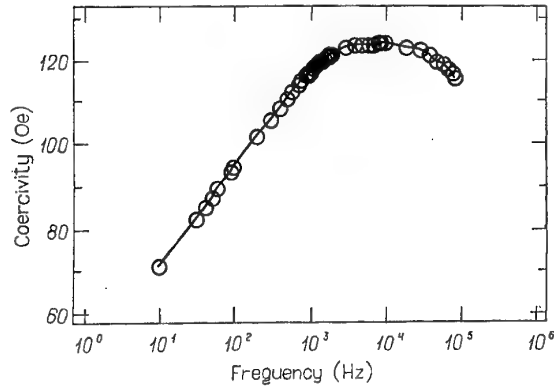


Fig. 11. The coercivity  $H_c$  as a function of frequency, for the same parameters as in Fig. 9.

frequency  $f_c$ . The dependence of  $f_c$  on the anisotropy, volume, and temperature is summarized in Fig. 13. From the simulated data, an empirical functional form for  $f_c(K, V, T)$  was obtained:

$$f_c = 10^{-9} \tau_0^{-1} \exp \left[ -(5.88 \cdot 10^{15} K / \text{erg}) \left( \frac{KV}{T} \right) - (4.33 \cdot 10^{-6} cc / \text{erg}) K + (4.11 \cdot 10^{20} K / cc) \right. \\ \left. \times \left( \frac{V}{T} \right) + 18.98 \right]. \quad (17)$$

Note that this formula is considerably more complex than Eq. 15, which was valid only in the limit of large  $K$ . For soft magnetic materials  $K$  is small, and numerical simulations are the only way to predict the cutoff frequency.

For the experimental grain size,  $r = 10$  nm, and an effective anisotropy equal to  $1.5 \cdot 10^5$  erg/cc would be needed to fit the observed room temperature value of  $f_c$ . This is a much larger value of the anisotropy estimated from the experimental coercivity and Sharrock's Law. Presumably the physically relevant volume  $V$  is not that of a single grain, but of a small number of coupled grains.

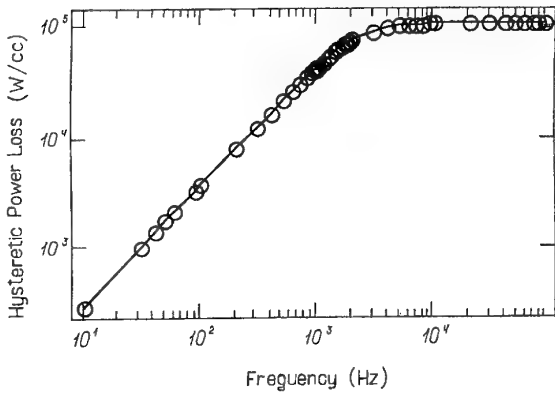


Fig. 12. The hysteretic power loss as a function of frequency, for the same parameters as in Fig. 9.

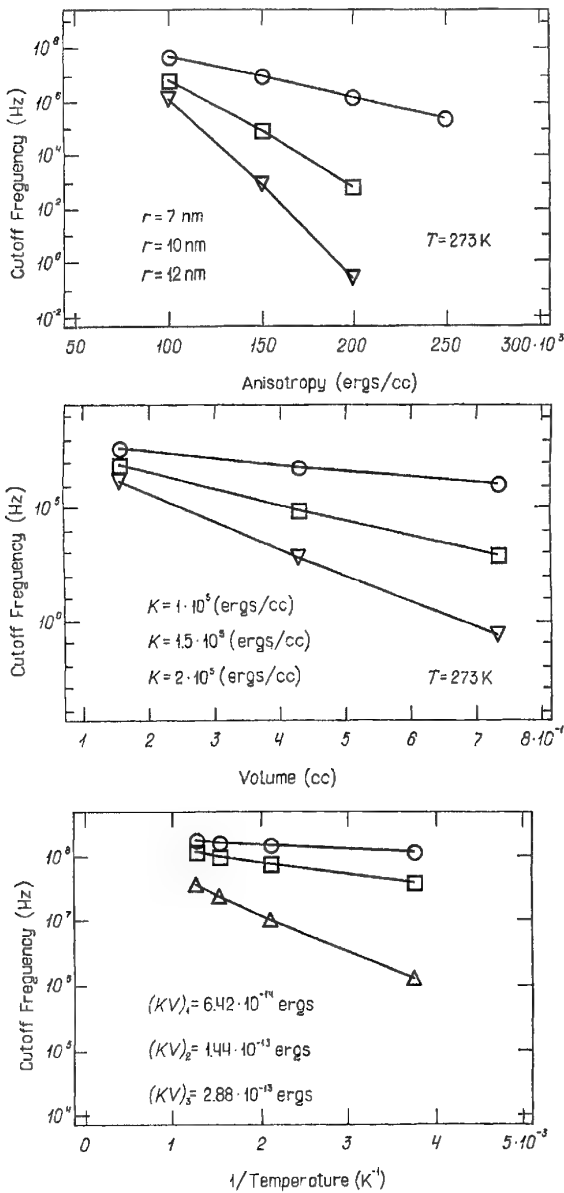


Fig. 13 a.)  $f_c$  as a function of the anisotropy for spheres of different radii. Here  $V = (4\pi/3)r^3$ ; b.)  $f_c$  as a function of the volume; c.)  $f_c$  as a function of the inverse temperature.

## 6. CONCLUSIONS

The AC magnetic properties of soft magnetic nanocomposites made from compaction of  $Fe_{10}Co_{90}$  nanoparticles can be understood in terms of an effective anisotropy and a related exchange coupled volume. The permeability is constant and equal to the DC value for low frequencies, but drops off above a characteristic frequency  $f_c$ . For bulk materials such as ferrites the cutoff frequency can be extremely high, and the behavior is understood in terms of the Landau-Lifshitz-Gilbert equation [21-23]. However for compacted nanocomposites the cutoff frequency is much lower,

and depends on the sample microstructure. The value of this frequency can be increased by raising the temperature, or by reducing the anisotropy and grain size. Experiments are in progress to prepare samples to further test this model.

## ACKNOWLEDGMENTS

This work was supported in part by the National Science Foundation under Grant numbers DMR-9900550 and ECD-8907068, and by the Air Force Office of Scientific Research under grant number F49620-96-1-0454. The assistance of K. Humfeld and N. Ide in the simulations is greatly appreciated.

## REFERENCES

- [1] G. Herzer // *IEEE Trans. Mag.* **25** (1989) 3327.
- [2] G. Herzer // *IEEE Trans. Mag.* **26** (1990) 1397.
- [3] G. Herzer // *J. Magn. Magn. Mater.* **112** (1992) 258.
- [4] Y. Yoshizawa, S. Oguma and K. Yamauchi // *J. Appl. Phys.* **64** (1988) 6044.
- [5] A. Makino, T. Hatani, Y. Naitoh, T. Bitoh, A. Inoue and T. Masumoto // *IEEE Trans. Mag.* **33** (1997) 3793.
- [6] R. Alben, J. J. Becker and M. C. Chi // *J. Appl. Phys.* **49** (1978) 1653.
- [7] N. Ashcroft and D. Mermin, *Solid State Physics* (Harcourt Brace, NY, 1976).
- [8] R. A. McCurtie, *Ferromagnetic Materials: Structure and Properties* (Academic Press, NY, 1994).
- [9] J. Zhang, C. Boyd and W. Luo // *Phys. Rev. Lett.* **77** (1996) 390.
- [10] M. I. Shliomis and V. I. Stepanov, in *Advances in Chemical Physics*, ed. W. Coffey (Wiley, NY, 1987) **87** 1.
- [11] C. W. Chen, *Magnetism and Metallurgy of Soft Magnetic Materials* (Dover, NY, 1986).
- [12] F. Pfeifer and C. Radloff // *J. Magn. Magn. Mat.* **19** (1980) 190.
- [13] G. Vieu, F. Fievet-Vincent and F. Fievet // *J. Mater. Chem.* **6** (1996) 1047.
- [14] J. H. J. Scott, Z. Turgut, K. Chowdary, M. E. McHenry and S. A. Majetich // *Mat. Res. Soc. Symp. Proc.* **501** (1998) 121.
- [15] E. C. Stoner and E. P. Wohlfarth // *Phil. Trans. Roy. Soc. A* **240** (1948) 599.
- [16] W. F. Brown, Jr. // *J. Appl. Phys.* **29** (1958) 470.
- [17] W. F. Brown, Jr. // *J. Appl. Phys.* **30** (1959) 130.
- [18] A. K. Jonscher, *Dielectric Relaxation in Solids* (Chelsea Dielectrics Press, Ltd., London, 1983).
- [19] P. Debye, *Polar Molecules* (Chemical Catalog Co., NY, 1929).

[20] M. P. Sharrock // *IEEE Trans. Mag.* **26** (1990) 193.

[21] L. Landau and E. Lifshitz // *Phys. Z. Sowjetunion* **8** (1936) 153.

[22] T. L. Gilbert, *Ph. D. thesis*, Illinois Institute of Technology, Chicago, IL, June 1956.

[23] H. B. Callen // *J. Phys. Chem. Solids* **4** (1958) 256.

## NANOSTRUCTURED Ni FILMS BY POLYOL ELECTROLESS DEPOSITION

J. Zhang<sup>1</sup>, G.M. Chow<sup>1</sup>, S.H. Lawrence<sup>2</sup> and C.R. Feng<sup>2</sup>

<sup>1</sup>Department of Materials Science, National University of Singapore, Kent Ridge,  
Singapore 117543, Republic of Singapore

<sup>2</sup>Naval Research Laboratory, Washington, DC 20375, USA

Received: November 17, 1999

**Abstract.** Nanostructured Ni films were deposited on Cu by reducing nickel acetate tetrahydrate in refluxing ethylene glycol at about 194 °C. The effects of deposition time (*t*) and Pt as nucleating aid were investigated in this polyol process. The solution chemistry varied with *t*. At longer *t*, corrosive attack of the solvent on deposited films led to dissolution and re-deposition of Ni. Saturation magnetization increased with *t* and decreased with increasing Pt precursors. The deposited Ni films were magnetically saturated. They showed in-plane magnetization anisotropy and perpendicular coercivity anisotropy. The use of Pt caused rapid powder precipitation but did not enhance film deposition. The Pt-catalyzed Ni films showed a (200) texture and a higher squareness ratio.

### 1. INTRODUCTION

Nanostructured films have attracted much attention because of their unique properties that arise from effects of size reduction and large amount of interfaces [1]. These films can be prepared by many methods, for example, sputtering, laser ablation, electrodeposition and electroless deposition. For uniform metallization of non-planar and/or hidden surfaces, solution chemistry is better suited than the physical vapor methods, since it is not limited by the line-of-sight deposition.

An electroless polyol method, which has been mainly used to synthesize micron, submicron and nanostructured powders [1-8], has been recently applied for deposition of nanostructured metal films, for example, Cu film on AlN substrate [9] and  $Ni_xCo_{100-x}$  film on Cu substrate [10]. The  $Ni_xCo_{100-x}$  films exhibited good magnetic properties with perpendicular coercivity anisotropy [10]. The structure of these films have been recently investigated using anomalous x-ray scattering to determine if a solid solution or phase-separated composite was formed and the element-selected long range order [11]. To date, the film deposition chemistry and mechanisms of this polyol process are not yet well understood. Unlike physical vapor deposition where the flux of atoms can be maintained constant, the solution chemistry (thus deposition

chemistry) may vary as a function of deposition (reaction) time.

In this paper, we report our investigation of the magnetic properties of polyol-deposited Ni films and their dependence on the deposition time (*t*). The effects of increasing *t* on crystallite size, film thickness, microstructures and magnetic properties were studied. The influence of Pt as nucleating aid, which has been used in polyol synthesis of powders [12], on Ni film deposition was also studied.

### 2. EXPERIMENTAL

Polycrystalline, coarse-grained copper with (200) texture was used as substrates without any pre-deposition surface treatment or polishing. 0.1 M nickel acetate tetrahydrate was suspended in 200 ml ethylene glycol. Hexachloroplatinic acid in small quantity was added in reactions where the effects of nucleating aid were investigated. The ratio of concentration of Pt to Ni ( $[Pt]/[Ni]$ ) was estimated from the starting precursors. The substrate was vertically suspended in the mixture, which was brought to reflux at about 194 °C. Deposition time (*t* = 0.5, 1, 2 and 3 h) was taken on the base of the time required to reach the the refluxing temperature. After each deposition, the coated sample was immediately removed from the mixture, rinsed with

Corresponding author: G.M. Chow, e-mail: [mascgm@nus.edu.sg](mailto:mascgm@nus.edu.sg)

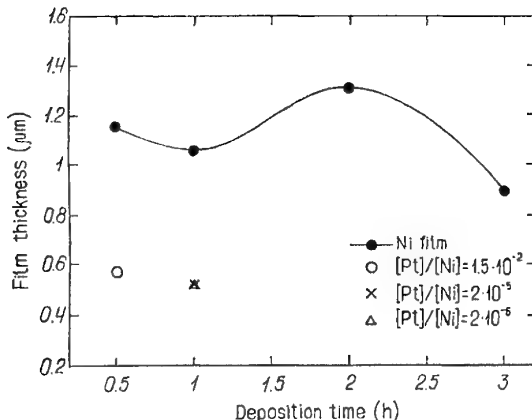


Fig. 1. Dependence of Ni film thickness on deposition time.

distilled water and acetone or 2-propanol, and subsequently air-dried for characterization.

The structure of the films was studied using x-ray diffraction (XRD) in the  $\theta$ - $2\theta$  mode. The diffraction peaks were analyzed using a profile fit routine and the FWHM of the specular peaks were used for estimation of average crystallite size and strain of these films. It was assumed that the total line broadening ( $B_{\text{total}}$ ) was the linear sum of that due to size and strain. A plot of  $(B_{\text{total}} \cos \theta) \text{ vs } \sin \theta$  yielded the strain and the size from the slope and intercept, respectively. The microstructure was investigated using scanning electron microscopy (SEM) and transmission electron microscopy (TEM). Cross-sectioned samples were checked with SEM for film thickness determination. The hysteresis loops were measured using vibrating sample magnetometry (VSM) in the parallel ( $\parallel$ ) and perpendicular ( $\perp$ ) directions to the film plane using a maximum magnetic field of  $\pm 50$  kOe.

### 3. RESULTS AND DISCUSSIONS

The dependence of film thickness on  $t$  and the  $[\text{Pt}]/[\text{Ni}]$  is shown in Fig. 1. For  $t = 3$  h, the decrease in film thickness may be related to the corrosive attack of ethylene glycol on deposited Ni films. It has been reported for other systems involving chemical oxidation of ethylene glycol at elevated temperatures, oxalic acid was identified as a product. Both it and various organic acids that were formed as intermediates are corrosive to metals [13]. Nickel and Pt are miscible below 200 °C. When Pt was used as nucleating aid, the reaction completed at about 0.5 h for  $[\text{Pt}]/[\text{Ni}]$  of  $1.5 \cdot 10^{-2}$ . When  $[\text{Pt}]/[\text{Ni}] \leq 2 \cdot 10^{-3}$ , the reaction took about 1 h to finish. The use of Pt precursors for aiding nucleation of Ni nanocrystals has been reported [12]. The similar results were reported for Pd(II) and Cu(II) acetates in 2-ethoxyethanol at 135 °C, in which initial Pd reduction assisted the reduction of copper [14]. In this work, Pt

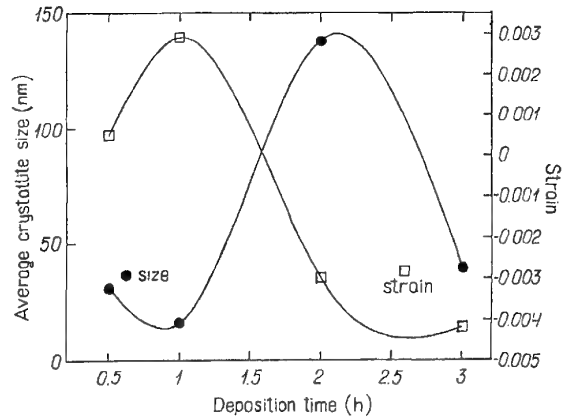


Fig. 2. Dependence of crystallite size and strain on deposition time.

precursor only promoted rapid precipitation of Ni powder but it did not enhance film deposition, since thinner films were obtained compared to those deposited without Pt (Fig. 1). The undesirable competition between powder precipitation and film formation can be minimized by application of electric field during deposition and lower deposition temperature [15].

The XRD results showed that Ni was polycrystalline fcc. The average crystallite size and strain of Ni films are shown in Fig. 2. The crystallite size reached a maximum of about 138 nm at  $t = 2$  h, but it significantly decreased to 40 nm at  $t = 3$  h. The decrease in crystallite size and film thickness at longer  $t$  was the result of corrosive attack of the solvent on the deposited films, leading to dissolution and re-deposition of finer particles. The micro-strain of these films changed from tensile to compressive with increasing  $t$ . Fig. 3 shows the SEM micrographs of Ni films deposited at  $t = 2$  and 3 h, respectively. It can be seen that sintering of films occurred (thus largest crystallite size as shown in Fig. 2) at  $t = 2$  h, whereas finer particles were observed in film deposited at  $t = 3$  h. Note that the particles seen in SEM consisted of nanostructured crystallites (measured by x-ray line broadening). Fig. 4 shows a TEM micrograph of Ni crystallites on Cu substrate deposited at  $t = 2$  h.

The XRD patterns of Ni films prepared using Pt catalysts only showed only Ni, without any evidence of Pt as a separate phase. The average crystallite size (estimated from (111) line broadening) increased with decreasing  $[\text{Pt}]/[\text{Ni}]$  precursor molar ratio from 33 to about 70 nm. The similar results of dependence of Ni particle size on Pt nucleating aid was reported in the polyol synthesis of Ni powders [12].

The Ni films were magnetically saturated. Both Ni and Pt-catalyzed Ni films exhibited in-plane magnetization anisotropy. Fig. 5 shows the  $M_{s\parallel}$  and  $M_{s\perp}$  for Ni films deposited at 0.5 and 3 h. Fig. 6 shows the depen-

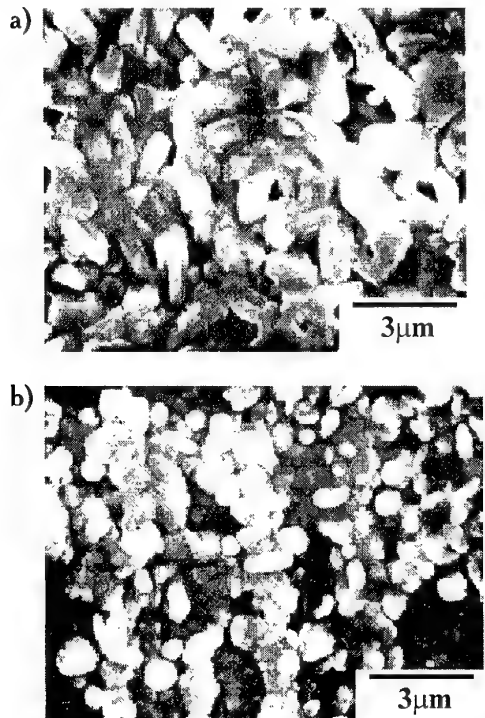


Fig. 3. SEM micrographs of Ni films deposited at : a) 2 h, b) 3 h.

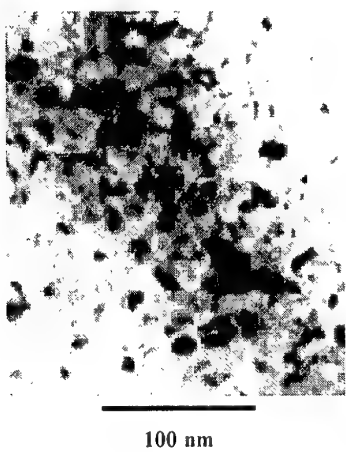


Fig. 4. TEM bright field micrograph of Ni film on Cu substrate deposited at 2 h. Dark particles are Ni.

dence of  $M_s$ ,  $H_c$ , and  $H_{c1}$  of Ni films on  $t$ . The  $M_s$  of bulk fcc Ni is about  $M_s$  is 484 emu/cm<sup>3</sup>. The values of  $M_s$  increased with  $t$  and reached 405 emu/cm<sup>3</sup> for the Ni film deposited 3 h. This may be due to the increased film density at longer  $t$ . For films consisting of randomly oriented crystallites, the squareness ratio (ratio of remanent magnetization,  $M_r$ , to saturation magnetization,  $M_s$ ) is typically about 0.5. This ratio was between 0.4 and 0.5 for Ni films, except it was higher for that deposited at 1 h (about 0.6). Fig. 7 shows  $M_{s//}$  and the squareness ratio of Ni films deposited with Pt catalysts.  $M_s$  increased whereas squareness ratio

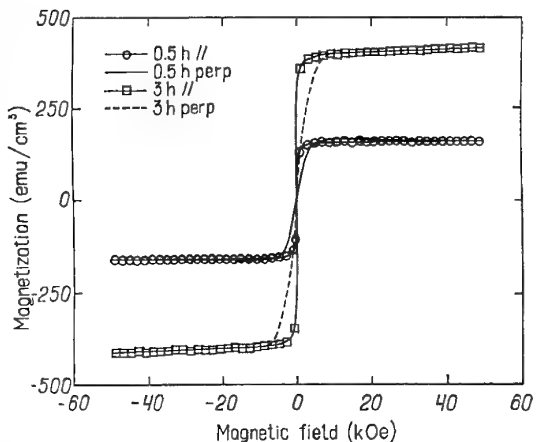


Fig. 5. Hysteresis loops of Ni films deposited at 0.5 h and 3 h, showing magnetic saturation and in-plane anisotropy.

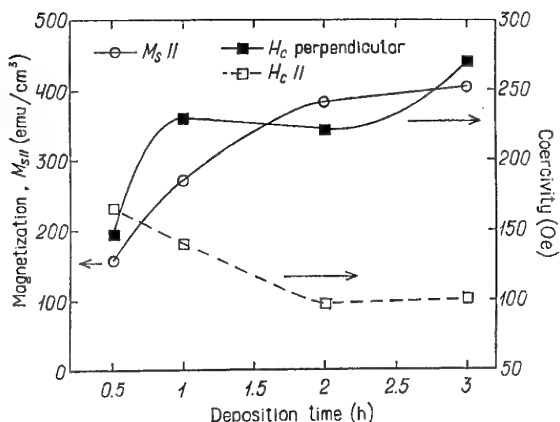


Fig. 6. Dependence of saturation magnetization and coercivity of Ni films on deposition time.

decreased with decreasing [Pt]/[Ni]. The deposition time for Ni films using [Pt]/[Ni] of  $2 \cdot 10^{-5}$  and  $2 \cdot 10^{-6}$  was about 1 h, and was 0.5 h for [Pt]/[Ni] of  $1.5 \cdot 10^{-2}$ . Pt had a predominant effect on  $M_{s//}$  and a lower [Pt]/[Ni] ratio led to a higher  $M_s$  as expected. Lower  $M_s$  may be related to alloying of Pt with Ni. Examination of XRD data of these films showed a (200) texture. This is consistent with the higher squareness ratio (between 0.56 to 0.65) of these films. Fig. 8 shows that the films deposited with Pt catalysts also had higher perpendicular coercivity. The coercivity anisotropy may be related to the microstructures of deposited film [15]. The work is currently underway to investigate the structure and microstructure of these films by transmission electron microscopy.

#### 4. SUMMARY

Nanostructured Ni films were deposited by the polyol method on Cu substrates with or without Pt as nucleating aid. The solution chemistry varied with  $t$ . At longer

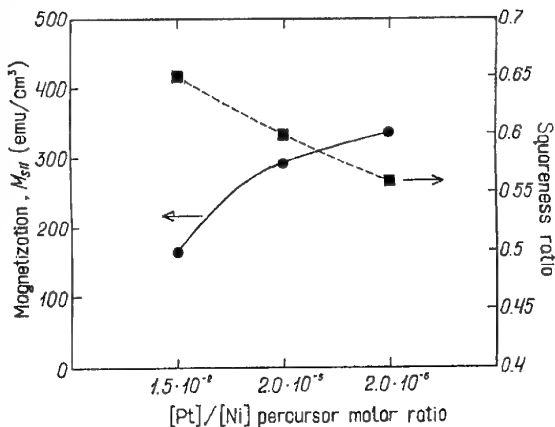


Fig. 7. Dependence of saturation magnetization and square ratio of Ni films on  $[Pt]/[Ni]$  precursor molar ratio.

$t$ , corrosive attack of the solvent on deposited films led to dissolution and re-deposition of Ni. Saturation magnetization increased with  $t$  and decreased with increasing Pt precursor concentration. The magnetically saturated films showed in-plane magnetization anisotropy and perpendicular coercivity anisotropy. The use of Pt favored rapid powder precipitation but did not enhance film deposition. The Pt-catalyzed Ni films showed a (200) texture and a higher squareness ratio. Further work is needed to understand the solution chemistry and film deposition chemistry in the polyol process.

## ACKNOWLEDGMENTS

GMC thank the support of this work by the Academic Research Grant of the National University of Singapore and the US Office of Naval Research. J. Zhang was supported by the NUS postgraduate research scholarship.

## REFERENCES

- [1] G.M. Chow, I. Ovid'ko and T. Tsakalakos (eds.), *Nanostructured Films and Coatings*, NATO Advanced Research Workshop, Santorini, Greece (Kluwer Publications, the Netherlands, 2000, in press).
- [2] F. Fiévet, J.P. Lagier and M. Figlarz // *Mater. Res. Soc. Bull.* (1989) 29.
- [3] F. Fiévet, J.P. Lagier, B. Blin, B. Beaudoin and M. Figlarz // *Solid State Ionics* **32/33** (1989) 198.
- [4] G. Viau, F. Ravel, O. Acher, F. Fiévet-Vincent and F. Fiévet // *J. Appl. Phys.* **76** (1994) 6570.
- [5] L.K. Kurihara, G.M. Chow and P.E. Schoen // *Nanostructur. Mater.* **5** (1995) 607.
- [6] G.M. Chow, L.K. Kurihara, K.M. Kemner, P.E. Schoen, W.T. Elam, A. Ervin, S. Keller, Y.D. Zhang, J. Budnick and T. Ambrose // *J. Mater. Res.* **10** (1995) 1546.
- [7] G. Viau, F. Fiévet-Vincent, and F. Fiévet // *Solid State Ionics* **84** (1996) 259.
- [8] G. Viau, F. Fiévet-Vincent and F. Fiévet // *J. Mater. Chem.* **6** (1996) 1047.
- [9] G.M. Chow, L. K. Kurihara, D. Ma, C. R. Feng, P.E. Schoen and L.J. Martinez-Miranda // *Appl. Phys. Lett.* **70** (1997) 2315.
- [10] G.M. Chow, J. Ding, J. Zhang, K.Y. Lee, D. Surani and S.H. Lawrence // *Appl. Phys. Lett.* **74** (1999) 1889.
- [11] G.M. Chow, W.C. Goh, Y.K. Hwu, T.S. Cho, J.H. Je, H.H. Lee, H.C. Kang, D.Y. Noh, C.K. Lin and W. D. Chang // *Appl. Phys. Lett.* **75** (1999) 2503.
- [12] M.S. Hedge, D. Larcher, L. Dupont, B. Beaudion, K. Tekaia-Elhsissen and J.-M. Tarascon // *Solid State Ionics* **93** (1997) 33.
- [13] C.B. Jordan, *Engine Coolant Testing*, Second Symposium, (American Society for Testing of Metals, 1986), p. 249.
- [14] J.S. Bradley, E.W. Hill, C. Klein, B. Chaudret, and J. Duteil // *Chemistry of Materials* **5** (1993) 254.
- [15] G.M. Chow, J. Zhang, Y.Y. Li, J. Ding and W.C. Goh // *Mat. Sci. Eng. A*, in press.

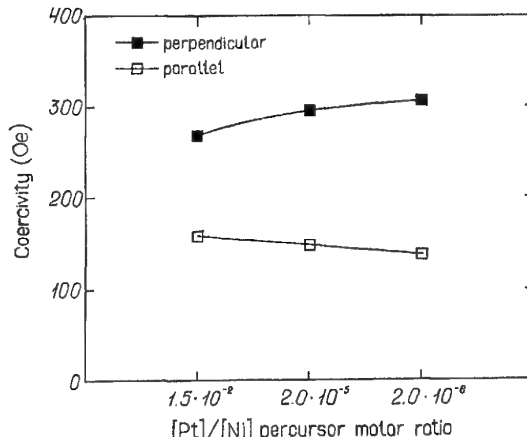


Fig. 8. Dependence of coercivity of Ni films on  $[Pt]/[Ni]$  precursor molar ratio.

## HETEROEPITAXIAL GROWTH OF InAs ON Si: THE NEW TYPE OF QUANTUM DOTS

**G.E. Cirlin<sup>1,2</sup>, N.K. Polyakov<sup>1,2</sup>, V.N. Petrov<sup>1</sup>, V.A. Egorov<sup>1</sup>, D.V. Denisov<sup>2</sup>, B.V. Volovik<sup>2</sup>, V.M. Ustinov<sup>2</sup>, Zh.I. Alferov<sup>2</sup>, N.N. Ledentsov<sup>2,3</sup>, R. Heitz<sup>3</sup>, D. Bimberg<sup>3</sup>, N.D. Zakharov<sup>4</sup>, P. Werner<sup>4</sup>, U. Gösele<sup>4</sup>**

<sup>1</sup> Institute for Analytical Instrumentation RAS, Rizhskiy pr. 26, 198103, St.Petersburg, Russia

<sup>2</sup> A.F.Ioffe Physico-Technical Institute RAS, Polytechnicheskaya 26, 194021, St.Petersburg, Russia

<sup>3</sup> Technical University, Hardenbergstraße 36, 10623, Berlin, Germany

<sup>4</sup> Max-Plank-Institute for Microstructure Physics, Weenbergs 2, D-06120, Halle/Saale, Germany

*Received: October 11, 1999*

**Abstract.** Under certain growth conditions InAs/Si heteroepitaxial growth proceeds via Stranski-Krastanow or Volmer-Weber growth modes depending on the growth parameters. The critical thickness at which three dimensional InAs islands start to appear at the Si(100) surface is within the range of 0.7–4.0 monolayers (substrate temperature range is 350 °C – 430 °C). Their size depends critically on the growth conditions and is between 5 nm and 80 nm (uncapped islands). Critical lateral size of the coherent (Si capped) dislocation-free island is equal to 2–5 nm depending on the island height. Islands having larger size are dislocated. Optical properties of InAs nanoscale islands capped with Si reveal a luminescence band in the 1.3 μm region.

### 1. INTRODUCTION

Self-organisation effects on semiconductor surfaces which occur in the course of molecular beam epitaxy (MBE) have attracted much attention over the last ten years. A particular interest was shown in the quantum dots (QDs) in III/V – III/V (e.g., InAs – GaAs) [1, 2], II/VI – II/VI (e.g., CdSe – ZnSe) [3] or IV – IV (Si – Ge) [4] materials systems. This system stimulates much investigations because silicon remains a key material in the modern microelectronics industry. For optoelectronic applications silicon is not well suitable because of its indirect band gap nature. Attempts to improve the situation using SiGe – Si QDs did not lead to a significant progress as these nanostructures provide indirect band alignment both in  $k$  – and in real space. In order to increase luminescence efficiency of silicon-based structures we propose to insert direct bandgap InAs QDs in a Si matrix using MBE growth [5]. We emphasize that this approach is different from the growth utilizing InAs QDs on thick GaAs buffers [6]. Small coherent InAs islands additionally enable a possibility to overcome the problems of strong lattice mismatch and formation of antiphase domains inherent for the growth of thick III – V epilayers (e.g. GaAs) on Si.

In this paper we report on the MBE growth and properties of the InAs nanoscale islands formed on sili-

con. We have found that under certain growth conditions InAs/Si heteroepitaxial growth proceeds via Stranski-Krastanow or Volmer-Weber growth modes depending on the growth parameters leading to the formation of nanoscale islands. The lateral size depends critically on the growth conditions and is in the range of 2–80 nm. Optical properties of InAs QDs capped with Si reveal a luminescence band in the 1.3 μm region. A pronounced excitation density dependence of the photoluminescence (PL) peak position and a decay time of approximately 400 ns were observed.

### 2. EXPERIMENTAL DETAILS

The growth experiments were carried out using EP1203 (Russia) or Riber Supra (France) MBE machines on exactly oriented Si(100) substrates. The Si(100) surface was prepared in a way similar to that described in [7]. Thermal desorption of silicon native oxide was performed in a growth chamber at the substrate temperature of 830 °C – 870 °C during 15 min. Afterwards, well-resolved (2×1) or mixed (1×2) and (2×1) surface reconstructions typical for cleaved Si(100) surface were observed. Then the substrate temperature was smoothly reduced to the desired value and the InAs deposition was initiated at a conventional MBE mode. The InAs deposition rate was typically 0.1 monolayer (ML) per

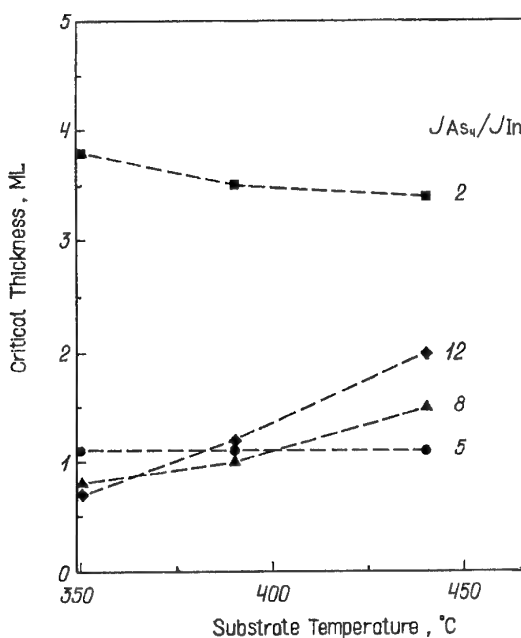


Fig. 1. Critical thickness dependence on substrate temperature and  $J_{As_4}/J_{In}$  fluxes ratio during InAs/Si growth.

second. When the deposition of the desired average thickness of InAs had been completed, the sample was immediately quenched to the room temperature and removed from the growth chamber in order to perform scanning tunnelling microscopy (STM) and scanning electron microscopy (SEM) studies. SEM measurements were performed using CamScan setup. Pieces for STM studies were covered with silicon vacuum oil immediately after exposure to the atmosphere, a procedure used before in our studies of InAs QDs on GaAs surfaces [8]. A calibration of the growth rate, III – V flux ratio, and monitoring of the surface morphology during growth was performed using reflection high energy electron diffraction (RHEED) system composed of a high sensitivity video camera, a video tape recorder and a computer, all interconnected via specially-designed interface [9]. Transmission electron microscopy (TEM) images were obtained on the samples when InAs islands were covered with 30–50 nm of silicon using JEOL 4000EX microscope. The same structures were used for luminescence experiments. A 514.5 nm line of the Ar<sup>+</sup> laser was used as an excitation source and a Ge photodiode as a detector. The excitation density was 5–100 W/cm<sup>2</sup>. The structures for TEM and PL studies were grown in a following manner. Just after InAs deposition, a 10–20 nm Si cap layer was grown at the same substrate temperature  $T_s$  as for InAs deposition followed by a 10 min annealing procedure at 650 °C – 700 °C. Then 20–40 nm of Si was grown at the same temperature with optional

consequent 10 min annealing at 700 °C – 800 °C in order to smooth the resulting surface.

### 3. RESULTS AND DISCUSSION

In Fig. 1 we summarise RHEED data of the dependences of the substrate temperatures and  $As_4/In$  fluxes ratio in the ranges 350 °C – 450 °C and 2 – 12, respectively, on the critical thickness  $d_{crit}$  (mean thickness at which 3D nanoscale islands start to appear at the surface). The lowest limit of  $T_s$  was chosen for two reasons: first, determination of  $T_s$  at very low temperatures is difficult and second, because of poor quality of Si cap layer grown at too low temperatures. Poor quality of the Si cap layer may hinder the device applications. On the other hand, we have found that at temperatures higher than 450 °C *no nanoislanding is observed on the surface* independently on the V/III flux ratio, total arsenic overpressure, *etc.* limiting the range for the highest  $T_s$  as indicated in Fig. 1. (At higher  $T_s$  only mesoscopic dislocated clusters with lateral size of ~400 nm appeared on the Si(100) surface [10]). Following the data presented in Fig. 1 one can conclude that depending on the growth conditions, 2D–3D transition can be tuned in the thickness range of 0.7–4.0 ML. On the other hand, we have observed two different growth modes for the InAs/Si heteroepitaxial growth. First, Volmer–Weber growth mechanism could be realised when InAs nanoscale islands are formed on the bare Si substrate (i.e. for  $d_{crit} < 1$  ML). Typical RHEED pattern for this case is presented in Fig. 2,a. At higher  $T_s$  (400 °C – 450 °C) we observed Stranski–Krastanow growth mechanism when  $d_{crit}$  exceeded 1.0 ML and the formation of InAs nanoscale islands occurs on the top of the wetting layer. RHEED pattern for this particular case is presented in Fig. 2,b. These results are in agreement with the 2D – 3D transition intervals observed by other groups [11, 12].

Typical surface morphology extracted from the STM images for these cases revealed high density arrays of nanoscale islands (with surface density of the order of  $((1/6) \times 10^{11} \text{ cm}^{-2}$ ) and the lateral sizes of 10–20 nm [13, 14]. These islands are basically pyramidal in shape with rectangular or triangular base.

We have found that the growth conditions (the amount of InAs deposited, fluxes ratio influenced greatly the arrangement, sizes and surface density of InAs/Si islands [15]. In order to clarify how growth parameters influence the surface morphology we grew three samples, labelled 1–3. Their MBE growth conditions and geometrical characteristics measured with SEM are presented in the Table 1.

The main trends for the uncapped InAs/Si island formation are the following. At higher As pressure and

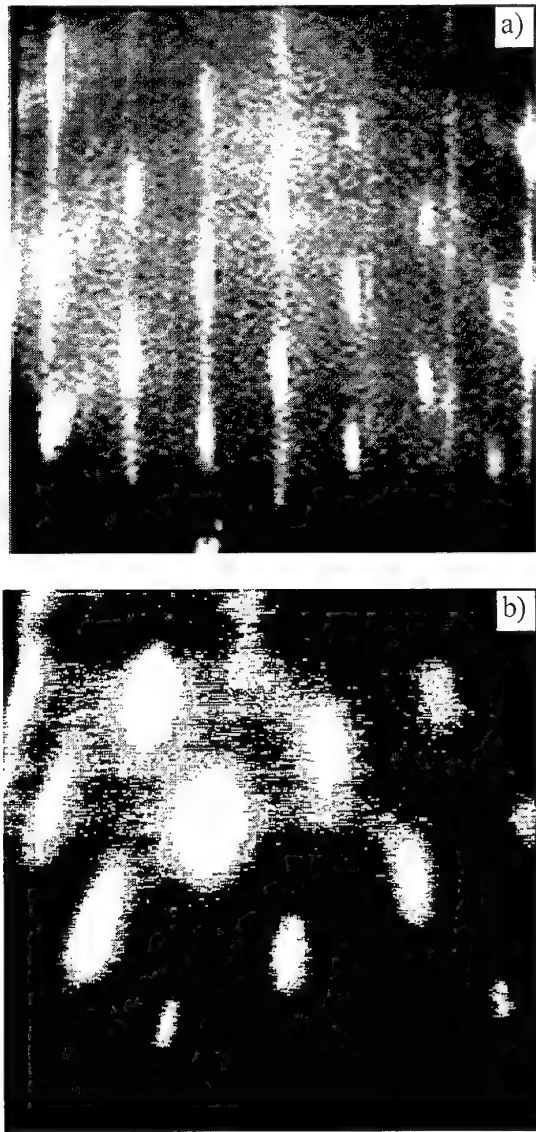


**Fig. 2.** Typical RHEED patterns in [011] direction taken after the formation of InAs 3D islands in Si(100) surface via (a) Volmer-Weber and (b) Stranski-Krastanow growth modes.

the same InAs mean thickness the island size drops as compared to the case of the decreased As/In fluxes ratio (samples 1 and 3). We believe that this is due to the suppressing of the surface migration length. The density of the islands for the sample 3 is four times higher

than that of the sample 1. The islands size distribution becomes narrower, too. With increasing the average InAs thickness (sample 2) the islands start to form large conglomerates. These clusters are elongated and exhibit crystallographic shape with the base oriented along [011] and [011] directions. The similar situation was observed in [11] where such clusters were formed during the InAs growth on Si(100) passivated (hydrogen-terminated) surfaces with approximately same size and surface density. We note that for the sample 2 the critical thickness is larger by the value of 1.8 ML, *i.e.* 2.5 times higher. In InAs/GaAs heteroepitaxial system such large sizes should lead to the formation of the dislocations. In order to check the crystalline quality we studied the same uncapped samples with cross-sectional TEM.

Most of the islands exhibited considerably good crystalline quality although misfit dislocations appeared at the InAs/Si interface. In Fig. 3 typical cross-section TEM image for single InAs nanoscale island is presented. Using high resolution TEM data taken from the Si capped samples we have found that the critical lateral size of the coherent dislocation-free islands is equal to 2-5 nm depending on the island height. Islands of

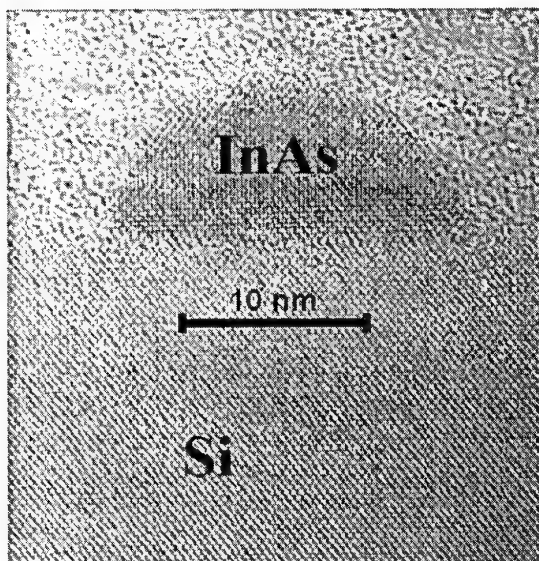


**Fig. 3.** Typical high resolution cross-section TEM image of the single InAs nanoscale island at Si(100) surface.

**Table.** MBE growth conditions and geometrical characteristics of the InAs/Si(100) quantum dot samples

Sample No.	InAs thickness, ML	As/In fluxes ratio	Island lateral size, nm	Surface density of islands, $10^{10} \text{ cm}^2$
1	1.2	3	15-50	4
2	2.5	3	20-80	1.6
3	1.2	10	3-15	16

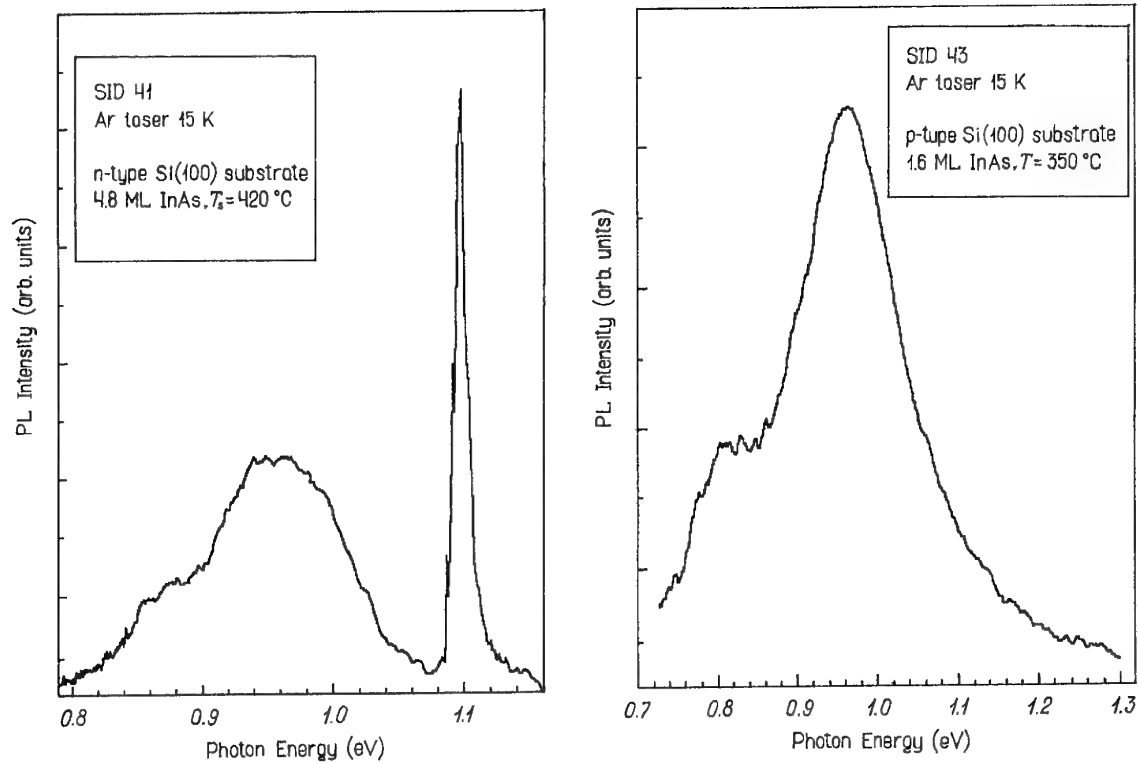


**Fig. 4.** PL data for the InAs nanostructures embedded in Si matrix: (a) InAs grown via Stranski-Krastanow, (b) InAs grown via Volmer-Weber growth modes.

larger size are defected due to misfit dislocations or twins. We also suggested that most of the InAs reevaporated during the deposition (or annealing) of the cap layer. Fig. 3. shows typical high resolution cross-section TEM image of the single InAs nanoscale island at Si(100) surface.

The samples with such InAs quantum dots capped with 30–50 nm Si layer show a luminescence band in the 1.3  $\mu$ m region for temperatures up to ~170K. The PL exhibited a pronounced blue shift with increasing the excitation density and decays at the time constant of ~400 ns [16]. Fig.4 compares low temperature PL spectra of the 4.8 ML with the 1.6 ML InAs samples deposited in different growth modes (Stranski-Krastanow for 4.8 ML and Volmer-Weber for 1.6 ML\*). These spectra reveal TO-phonon assisted exciton emission of the Si substrate and barrier at ~1.11 eV. The broad emission band in the 0.9 to 1.05 eV region was observed for both InAs deposition thickness suggesting its origin to be associated with the InAs nanoobjects embedded in Si matrix. This broad line was not observed for the samples with InAs insertions smaller than the critical thickness or on a Si substrate. However, the size of these insertions evaluated using TEM measurements does not exceed 5 nm [16] which

is definitely not enough for charge localisation and quantum confinement.

Our very recent detailed TEM investigation of these samples shows that besides a random distribution of InAs molecules, two kinds of ordering were detected. Such regions ( $\phi < 6$  nm) are characterised by larger InAs concentration. The first kind shows an ordering of InAs molecules in (101), (101) planes inclined to the [001] growth direction, while in the second one the ordered (110), (110) planes are parallel to the [001] growth direction. The formation of such a structure results in energy lowering due to the decrease of the number of mixed Si-As and Si-In bonds. We believe that the appearance of the broad PL peak is the result of solid solution formation and/or ordering, because the incorporation of InAs molecules into Si matrix changes the band gap of material and possibly shifts the relative positions of conduction and valence bands. Detailed results on TEM study will be presented in a separate paper [17].

#### 4. CONCLUSIONS

We have demonstrated that InAs/Si(100) heteroepitaxial growth might proceed via Stranski-Krastanow or Volmer-Weber growth modes depending on the MBE growth parameters. Critical thickness at which three dimensional InAs islands start to ap-

\* InAs critical thickness for both samples was exceeded by the value of 0.8 ML.

pear at the Si(100) surface varies within the range of 0.7–4.0 monolayers (substrate temperature is 350 °C – 430 °C, As/In fluxes ratio is 2–12). Their size depends critically on the growth conditions and is between 5 nm and 80 nm (uncapped islands). Critical lateral size for Si capped InAs coherent dislocation-free islands is equal to 2–5 nm depending on the island height. Islands of larger size are dislocated. Optical properties of the InAs nanoscale islands capped with Si reveal a luminescence band in the 1.3 μm region independently on the growth mode used for InAs deposition. The appearance of this peak can be caused by the solid solution formation and/or ordering due to the incorporation of InAs molecules into Si matrix during post growth annealing which changes the band gap of material and possibly shifts the relative positions of conduction and valence bands. InAs/Si heteroepitaxial system seems to be promising for Si-based optoelectronic applications, in particular for short distance fiber optics and integration of microelectronics and optical parts at the same silicon wafer.

## ACKNOWLEDGEMENTS

The authors thanks to N.P. Korneeva, V.N. Demidov, S.A. Masalov and V.M. Busov for their kind assistance during experiments. This work was supported by INTAS Grant No. 96-0242, Russian Foundation for Basic Research Grant No. 98-02-18317 and Grant No. 99-02-16799, Russian Scientific Programmes “Physics of Solid State nanostructures” Grant No. 98-2029 and “Methods and Devices of Micro- and Nanoelectronics” Grant No 02.04.5.1.40.E.46.

## REFERENCES

- [1] L. Goldstein, F. Glas, J.Y. Marzin, M.N. Charasse, and G. Le Roux // *Appl. Phys. Lett.* **47** (1985) 1099.
- [2] D. Leonard, M. Krishnamurthy, C.M. Reaves, S.P. Denbaars and P.M. Petroff // *Appl. Phys. Lett.* **63** (1993) 3203.
- [3] M. Strassburg, V. Kutzer, U.W. Pohl, A. Hoffmann, I. Broser, N.N. Ledentsov, D. Bimberg, A. Rosenauer, U. Fischer, D. Gerthsen, I.L. Krestnikov, M.V. Maximov, P.S. Kop'ev and Zh.I. Alferov // *Appl. Phys. Lett.* **72** (1998) 942.
- [4] Feng Liu and M.G. Lagally // *Surf. Sci.* **386** (1997) 169.
- [5] N.N. Ledentsov in: Proceedings of the 23rd International Conference on the Physics of Semiconductors, Berlin, Germany, July 21-26, 1996, edited by M. Scheffler and R. Zimmermann (World Scientific, Singapore, 1996) 1 p. 19.
- [6] J.M. Gerard, O. Cabrol and B. Sermage // *Appl. Phys. Lett.* **68** (1996) 3123.
- [7] A. Ishisaka and Y. Shiraki // *J. Electrochem. Soc.* **133** (1986) 666.
- [8] G.E. Cirlin, G.M. Guryanov, A.O. Golubok, S.Ya. Tipishev, N.N. Ledentsov, P.S. Kop'ev, M. Grundmann and D. Bimberg // *Appl. Phys. Lett.* **67** (1995) 97.
- [9] G.M. Gur'yanov, V.N. Demidov, N.P. Korneeva, V.N. Petrov, Yu.B. Samsonenko and G.E. Tsyrin // *Tech. Phys.* **42** (1997) 956.
- [10] G.E. Cirlin, V.N. Petrov, V.G. Dubrovskii, S.A. Masalov, A.O. Golubok, N.I. Komyak, N.N. Ledentsov, Zh.I. Alferov and D. Bimberg // *Tech. Phys. Lett.* **24** (1998) 290.
- [11] T. Mano, H. Fujioka, K. Ono, Y. Watanabe and M. Oshima // *Appl. Surf. Sci.* **130—132** (1998) 760.
- [12] P.C. Sharma, K.W. Alt, D.Y. Yeh and K.L. Wang // *Appl. Phys. Lett.* **75** (1999) 1273.
- [13] G.E. Cirlin, V.G. Dubrovskii, V.N. Petrov, N.K. Polyakov, N.P. Korneeva, V.N. Demidov, A.O. Golubok, S.A. Masalov, D.V. Kurochkin, O.M. Gorbenko, N.I. Komyak, V.M. Ustinov, A.Yu. Egorov, A.R. Kovsh, M.V. Maximov, A.F. Tsatsul'nikov, B.V. Volovik, A.E. Zhukov, P.S. Kop'ev, Zh.I. Alferov, N.N. Ledentsov, M. Grundmann and D. Bimberg // *Semicond. Sci. Technol.* **13** (1998) 1262.
- [14] G.E. Cirlin, V.N. Petrov, V.G. Dubrovskii, Yu.B. Samsonenko, N.K. Polyakov, A.O. Golubok, S.A. Masalov, N.I. Komyak, V.M. Ustinov, A.Yu. Egorov, A.R. Kovsh, M.V. Maximov, A.F. Tsatsul'nikov, B.V. Volovik, A.E. Zhukov, P.S. Kop'ev, N.N. Ledentsov, Zh.I. Alferov and D. Bimberg // *Semiconductors* **33** (1999) 972.
- [15] G.E. Cirlin, N.K. Polyakov, V.N. Petrov, V.A. Egorov, Yu.B. Samsonenko, B.V. Denisov, V.M. Busov, B.V. Volovik, V.M. Ustinov, Zh.I. Alferov, N.N. Ledentsov, D. Bimberg, N.D. Zakharov and P. Werner // *Czech. J. Phys.* **49** (1999) 1547.
- [16] R. Heitz, N.N. Ledentsov, D. Bimberg, A.Yu. Egorov, M.V. Maximov, V.M. Ustinov, A.E. Zhukov, Zh.I. Alferov, G.E. Cirlin, I.P. Soshnikov, N.D. Zakharov, P. Werner and U. Gösele // *Appl. Phys. Lett.* **74** (1999) 1701.
- [17] N.D. Zakharov et.al., in: MRS'99 Fall meeting proceedings, in press.

## FABRICATION OF 2-D AND 3-D PHOTONIC BAND-GAP CRYSTALS IN THE GHz AND THz REGIONS

G. Kiriakidis and N. Katsarakis

Institute of Electronic Structure and Laser (IESL), Foundation for Research and Technology-Hellas (F.O.R.T.H.), P.O. Box 1527, Heraklion 711 10, Greece

Received: October 1999

**Abstract.** Two- and three-dimensional dielectric and metallic structures exhibiting photonic band-gaps in a broad frequency range were fabricated by deep X-ray lithography and laser micro-machining. These techniques seem promising for mass production of photonic structures with full band-gaps in a spectrum ranging from the millimeter wave up to the far infrared regime. Deep X-ray lithography was applied to produce periodic 3-D photonic band-gap structures based on the "three-cylinder" model with mid-gap frequencies up to 2.4 THz. Metallic 3-D structures with incorporated point and linear defects are currently under development. Layered metallic and metallo-dielectric structures exhibiting a cutoff frequency in the microwave regime were fabricated by laser precision machining. The observed cutoff frequency can be easily tuned by varying the interlayer distance or the filling fraction of the metal. Combinations of layers with different metal filling fractions create defect modes with relatively sharp peaks, which are also tunable. The metallo-dielectric structures are significantly smaller than the simple metallic ones. The experimental measurements seem to be in good agreement with theoretical calculations.

### 1. INTRODUCTION

Over the last decade, a new brand of artificial structures has raised the excitement of scientists. In analogy to electrons in a crystal, the propagation of electromagnetic waves travelling in periodic dielectric structures can lead to the formation of stop bands [1,2]. When these stop bands are wide enough to overlap for both polarization states along all crystal directions, the material displays a complete Photonic Band-Gap (PBG), that is, a frequency range where the propagation of electromagnetic waves is forbidden, irrespective of the propagation direction. These effects lead to some novel applications in quantum optics in the frequency range from microwave to the optical regime such as low-cost efficient microwave antennas, low-loss cavities and resonators and zero-threshold lasers [3-7]. Photonic crystals represent also a novel and promising improvement on the operating efficiency of either Laser Diodes or Light Emitting Diodes (LEDs). They have already been recognized for their ability to control the flow of light and their capacity to modulate, suppress, concentrate and direct it, in an enhanced light-matter interaction manner.

The potential of these artificial structures has been exploited by theoretical and experimental studies mainly on 2-D and 3-D photonic crystals operating from

the microwave to the optical regime utilizing a number of diverse fabrication techniques and materials. It is the purpose of this work to present an inside of two selected fabrication techniques for 2-D and 3-D crystals, namely LIGA [8] and laser machining [9], and explore their potentials, limitations and applications utilizing both dielectric and metallic materials.

### 2. 2-D PHOTONIC CRYSTALS

The critical factors to control the properties of 2-D photonic crystals are the refractive index contrast, the arrangement of the lattice elements and the fraction of high and low index materials in the lattice. In principle, the higher the refractive index contrast the stronger the expected effects and the larger the band-gap achievable. Fabrication of 2-D structures has flourished due to the fact that they are relatively easy to make utilizing tools and techniques borrowed from the silicon microelectronics industry. The most significant progress so far has been reported with planar structures patterned by standard photolithography or electron-beam lithography, generating patterns in the visible and near-IR ranges [10-12]. More recently, multiple exposure holography, a technique well established for some time, has been applied successfully to fabricate advanced structures [13]. The importance of

Corresponding author: G. Kiriakidis, e-mail:kiriakid@iesl.forth.gr

producing low dimensionality structures relates to the ease of manipulating for the photonic lattice particularly in as far as interfacing with optical elements such as fibres, light sources, detectors and waveguides are concerned. A typical 2-D photonic lattice consists of holes etched into a semiconductor substrate. One type of lattice is triangular, self-similar upon 60° rotations with two main directions of symmetry in the “honeycomb” configuration [14]. This, along with the “graphite” type have demonstrated the widest band-gaps when regions of semiconductors are surrounded by large regions of air, i.e. when the area fill-factor is low [15]. Under the above configurations the criterion for maximum effect is achieved when the optical path length in both materials is roughly equal. However, an additional important factor that determines the properties of 2-D PBGs is that of light confinement in the third dimension. Most successful structures presented to date utilize some forms of waveguide confinement. In such configurations there are a number of obvious advantages related with the application of epitaxial layer growth techniques and compatibility with established planar optoelectronic elements [16]. Advanced configuration designs have recently demonstrated PBG structures with high transmission, reflection and very sharp filtering characteristics, promising interesting future optoelectronic applications [17,18].

### 3. 3-D PHOTONIC CRYSTALS

The first experimental evidence of a 3-D photonic crystal was presented by E. Yablonovitch and co-workers [4,5] following the theoretical work of K. M. Ho and co-workers [6] in 1990. This was an array of holes drilled into high refractive index material (since called the “Yablonovite”) showing a stop band for the transmission of microwave radiation that extended from 10 to 13 GHz irrespective of the direction of propagation. Furthermore, it was demonstrated that by including a defect either by adding or removing material, localized states in the band-gap were created, in direct analogy to “doping” effects for semiconductors. For the microwave regime the immediate application for such an effect could be related to couple a PBG crystal with an antenna and allowing more flexibility and enhancement of the radiation process in point-to-point communications. The above proof-of-concept demonstration by E. Yablonovitch is known today as the “three-cylinder” model and presents a structure with the symmetry of the diamond. A corresponding diamond structure was also proposed by C. T. Chan and co-workers [19]. Later, the same group from Iowa State University designed a novel three-dimensional “layer-by-layer” structure demon-

strating again a full 3-D PBG over a wide range of structural parameters. This structure consisted of layers of one-dimensional dielectric rods of rectangular, circular or elliptical cross section. The band-gap is optimized by controlling the dielectric contrast of the materials been used, the filling factor of the dielectric and, of course, the lattice constant of the PBG structure. Although it was fundamentally important to demonstrate the existence of a full 3-D PBG in the microwave regime, the drive was soon focused towards the fabrication of truly “photonic” 3-D structures that operate in the near IR and eventually the visible regime of the electromagnetic spectrum. The obvious approach was to scale down fabrication techniques successfully employed in the microwave regime. Indeed, a significant improvement was first demonstrated by G. Feiertag and co-workers [8], showing the potential of combining deep X-ray lithography (LIGA technique) with the “three-cylinder” model to produce 3-D structures with lattice constants of 227 and 114  $\mu\text{m}$ , corresponding to mid-gap frequencies of 0.75 and 1.5 THz respectively. Detailed account of the LIGA processing results will be presented in the following section. Since then, the “layer-by-layer” model was matured further to a point of reaching into the far-IR producing structures displaying a stop-band between 1.35 and 1.95  $\mu\text{m}$  [20]. The use of microfabrication techniques to produce structures in the 1.5  $\mu\text{m}$  window has failed to show yet the expected sharp spectral response. However, the technique has been very useful in the fabrication of Metallic Photonic Band-Gap (MPBG) structures and is presented in details in the subsequent chapters. Finally, novel concepts that are based upon the self-organization of structures show the promise of the approach rather than providing a fully convincing demonstration.

### 4. The LIGA technique for PBG structures in the far infrared frequency range

LIGA is a well established technique for the production of high aspect ratio microstructures [21,22]. It combines deep X-ray lithography (DXRL) with synchrotron radiation, electroforming and ceramic moulding. Deep X-ray lithography with synchrotron radiation is used to transfer an absorber pattern from an X-ray mask into a thick resist material deposited on a substrate. The mask consists of an X-ray transparent membrane (e.g. Be, Si, Ti) with absorber structures made of gold. By shadow printing the mask pattern is transferred into the resist using X-rays. Synchrotron radiation is applied because of its high intensity and small divergence. In this way, extremely precise microstructures with high aspect ratios can be realized. Due to the extremely high depth of focus the lateral

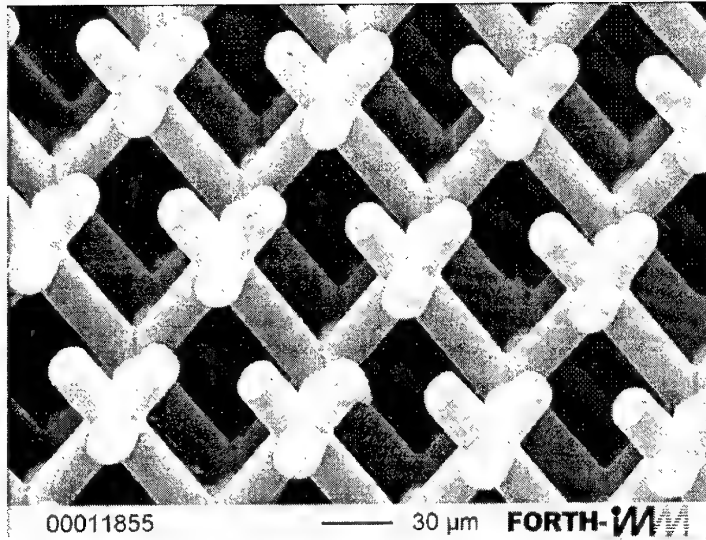


Fig. 1. 3-D photonic band-gap structure fabricated by LIGA according to the "three-cylinder" model.

deviations of the resist walls are as small as 0.05  $\mu\text{m}$  per 100  $\mu\text{m}$  thickness. PMMA is usually applied as resist material. It has very good properties to achieve vertical walls with a roughness of less than 50 nm. Through exposure, the resist undergoes a decrease in molecular weight and becomes soluble in an organic developer, if the deposited dose is above 2  $\text{kJ}/\text{cm}^2$ . After development of the exposed resist, the gaps of the resist relief are filled with metal via electroforming. The extremely accurate metal form can be used, e.g., for plastic moulding, offering inexpensive microstructure replication. A melted thermoplastic or a casting resin is injected through holes in a conducting gate plate, yielding a corresponding plastic structure which is fixed on by the remaining resin in the holes of the gate plate after cooling and separating the mold from the mold insert. The plastic structure obtained in the moulding process can be used as well as a "lost form" for the fabrication of ceramic microstructures. After filling the plastic form with a ceramic paste, a dense ceramic structure is formed by following conventional drying and firing processing. LIGA is a generic technology and therefore has a wide range of applications in fields such as sensors and actuators, optical engineering (integrated optics, nonlinear optics, fibre optics), electrical connectors, instrumentation for minimal-invasive surgery, biomedical and fluid-dynamical engineering and micro-filtration systems.

The "three-cylinder" model was selected for the fabrication of 3-D PBGs using LIGA. It is easily realized by three tilted irradiations of a PMMA slab using an X-ray mask with a triangular array of holes. Mask and resist are tilted 35° with respect to the synchrotron radiation beam. Between the irradiations, the tilted

arrangement of mask and resist must be rotated each time by 120°.

A process that comprises two main steps has been chosen for the fabrication of three-dimensional PBG structures in the far-IR [8]. Deep X-ray lithography is used to produce a mold which is then filled with a ceramic or pre-ceramic material (Fig. 1). It was first tried to fill the holes with a ceramic paste but the resist mold could not be filled completely. Therefore, it was decided to use a pre-ceramic polymer (polyvinylsilazane) that can be transformed into a silicon-carbonitride ceramic by a subsequent pyrolysis process.

The transmission characteristics of a structure with a lattice constant of 85  $\mu\text{m}$  and rod diameter of 22  $\mu\text{m}$  have been measured. The filling ratio of the ceramic rods in this structure was 35% and the total thickness of the structure 450  $\mu\text{m}$ . There is a constant drop of the transmission which is attributed to the absorption of the ceramic. The experimental results are in agreement with theoretical calculations (Fig. 2). There is also a well-defined drop of the transmission at around 80  $\text{cm}^{-1}$  (2.4 THz) which is related with the first band-gap created due to the periodicity of the structure. The gap over the mid-gap ratio for this stop band is  $\Delta\omega/\omega_g = 0.35$ . Transmission measurements for a similar photonic structure with rods diameter of 31  $\mu\text{m}$ , which corresponds to a filling ratio of 57%, show a gap at around 70  $\text{cm}^{-1}$  (2.1 THz) with  $\Delta\omega/\omega_g = 0.32$ .

Recent efforts are targeting the fabrication of metallic 2-D and 3-D structures with different kind of defects in the far-IR range of the electromagnetic spectrum. New photosensitive materials, like SU-8, are applied in order to achieve even higher aspect ratios for both 2-D and 3-D structures.

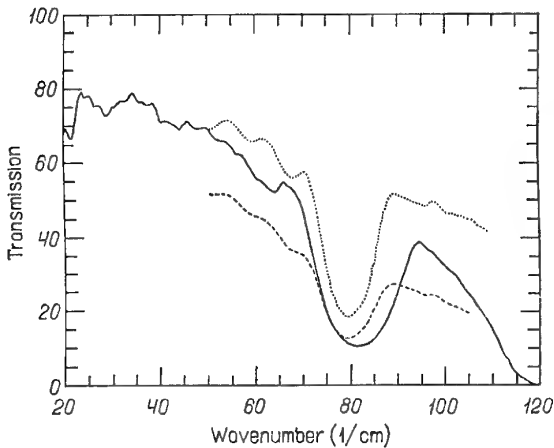


**Fig. 2.** Measured (solid line) and calculated results for a photonic structure with 85  $\mu\text{m}$  lattice constant and 22  $\mu\text{m}$  rods diameter. In the calculations, a dielectric constant of the rods with real part equal to 3 and imaginary part 0.1 and 0.2 was used (dotted and dashed lines respectively).

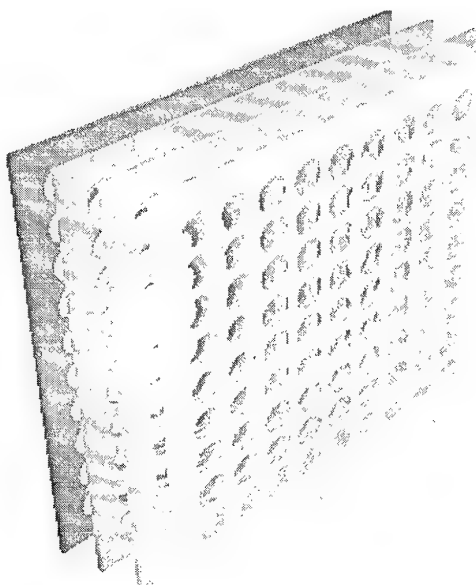


**Fig. 3.** A three-dimensional image of a layer-by-layer metallic photonic band-gap structure.

## 5. LASER-MACHINED METALLIC AND METALLO-DIELECTRIC PBG STRUCTURES

Most of the earlier research work was concentrated on the development of PBG crystals built from frequency-independent dielectrics. At lower microwave and millimeter wave frequencies, however, metals act like nearly perfect reflectors, no absorption problems occur, and there are certain advantages of introducing metals to photonic crystals. These include reduced size and weight, easier fabrication and lower costs.

Metallic photonic band-gap crystals (MPBG) operating in the microwave frequency range were fabricated by laser precision machining [9]. They consist of stainless steel plates with a tetragonal lattice of holes and a lattice constant of 15 mm. Transmission measurements show that periodic crystals exhibit a cutoff frequency in the 8-18 GHz range, below which no propagation is allowed. The cutoff frequency can be easily tuned by varying the interlayer distance or the filling fraction of the metal. Combinations of plates with different hole-diameters create defect modes with relatively sharp peaks, which are tunable.

In particular, stainless steel plates of 1 mm thickness were drilled using a Nd:YAG laser with a wavelength of 1064 nm and an output power of 100 W at a CNC working station with four degrees of freedom. The laser was operated in pulsed mode with a repetition rate of 120 Hz. Oxygen flow was necessary to prevent deposition of debris on the metal surface. The distance of the laser focusing system from the sample surface was 0.5 mm and the cutting velocity

600 mm/min. Holes with diameters of 8, 10, 12 and 14 mm were drilled on each plate in a square arrangement with a centre-to-centre distance of 15 mm (10·10 array). Four layers of each specific structure were fabricated. Consequently, periodic structures of up to 4 layers, as shown in Fig. 3, could be built and measured while combinations of layers with different hole-diameters could also be used to study defects.

All periodic structures behave like high-pass filters. They exhibit a cutoff frequency in the 8-18 GHz frequency range, below which there are no propagating modes. Within the band-gap, the rejection rate of the transmitted EM signal ranges between 5 and 10 dB per layer. The transmission characteristics of periodic structures consisting of three or four metallic layers with a tetragonal lattice of 12 mm-diameter holes at a distance of 7 mm are presented in Fig. 4. It can be seen that a structure with three layers exhibits a cutoff frequency at 12 GHz.

The cutoff frequency of the MPBG structures can be easily tuned by varying the distance between the metallic layers. In particular, by increasing the interlayer distance the gap-edge shifts to lower frequencies. In Fig. 5, it is demonstrated that the cutoff frequency is linearly related to the interlayer distance. These results are in good agreement with theoretical calculations that are shown in Fig. 6. The filling fraction of the metal also affects the observed cutoff frequency. A decrease in the hole-diameter, which corresponds to an increase in the filling ratio of the metal, shifts the gap-edge to higher frequencies. This behaviour is shown in Fig. 7, where it can be seen that

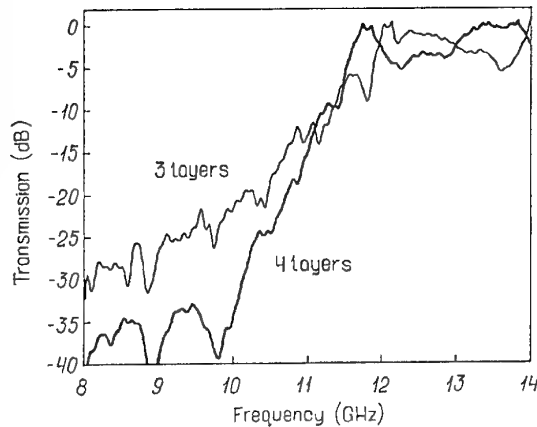


**Fig. 4.** Transmission profile for a periodic structure with three or four layers. The lattice constant (within one layer) is 15 mm, the diameter of the holes is 12 mm, and the distance between the layers is 7 mm.

indeed the cutoff frequency increases as the hole-diameter drops.

Defects are created easily by replacing the middle layer of a periodic structure with a layer having larger holes. Thus, in this way, metal deficiency is created in the middle layer. All defect structures show sharp transmitted modes in the prohibited frequencies of the periodic counterparts. The quality factor  $Q$  of the defect modes is about 70. Additionally, the introduction of a defect in the MPBG structure shifts the gap-edge to higher frequencies. In Fig. 8, defect structures consisting of three layers with hole-diameters of 8-12-8 mm and 8-14-8 mm are compared to the fully periodic one (8-8-8 mm). The removal of more metal from the middle layer (hole-diameters of 8-14-8 mm instead of 8-12-8 mm) moves the defect mode to lower frequencies while the position of the gap-edge is not affected.

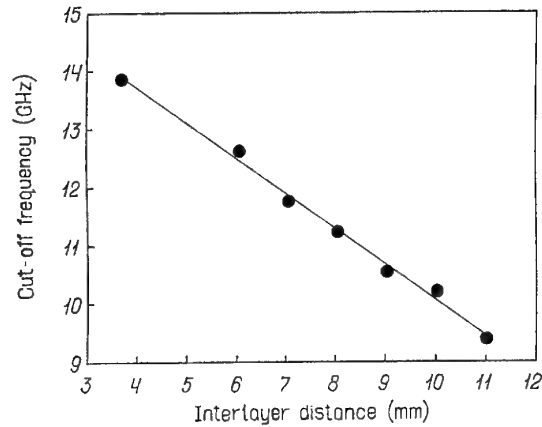


**Fig. 5.** Cutoff frequency as a function of the interlayer distance for a periodic structure similar with the one described in Fig. 2.

This demonstrates that not only the cutoff frequency but also the frequency of the defect modes can be tuned.

By changing the interlayer distance of the defect structure with hole-diameters of 8-12-8 mm from 7 mm to 9 mm, a shift of the total frequency spectrum to lower frequencies occurs, as has been also observed for the periodic counterparts. It is important to note that this effect does not change the distance between the defect peak and the gap-edge. The above observations have been also demonstrated on different arrangements such as the 12-12-14-12-12 mm structure.

However, the size of the simple metallic PBGs is restrictive for their application in microwave technology. Therefore, it is essential to reduce their size by introducing other dielectrics rather than air. Metallo-dielectric PBG structures operating in the microwave frequency range and especially between 10

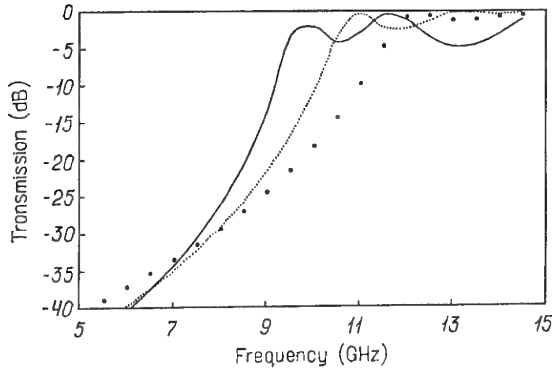


**Fig. 6.** Calculated transmission profiles for periodic structures consisting of three layers with hole-diameters of 12-12-12 mm at a distance of 11, 9, and 7 mm (solid, dashed and dotted line respectively). The lattice constant within one layer is 15 mm for all structures.

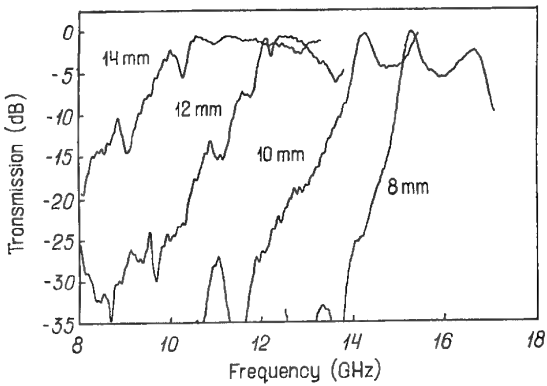


**Fig. 7.** Cutoff frequency as a function of the hole-diameter.

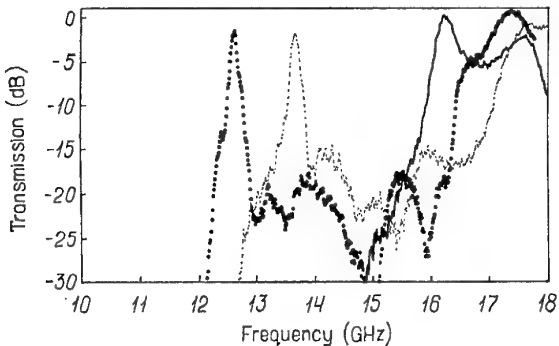


Fig. 8. Transmission profiles for defect structures consisting of three layers with hole-diameters of 8-12-8 mm and 8-14-8 mm (dashed and dotted line respectively) as well as for the periodic structure with hole-diameters 8-8-8 mm (solid line). In all cases, the lattice constant within one layer is 15 mm and the interlayer distance is 7 mm.

and 18 GHz were fabricated according to the layer-by-layer model. In particular, a metal (aluminum) pattern was applied onto  $\text{Al}_2\text{O}_3$  wafers. The pattern consists of a square lattice of metal grids with a lattice constant of 5 mm. Transmission measurements show that periodic structures, consisting of up to four wafers laterally aligned to each other, exhibit a cutoff frequency in the 10-18 GHz frequency range, below which no propagation is allowed (Fig. 9). The cutoff frequency can be easily tuned by varying the interlayer distance or the width of the metallic grids. Combinations of wafers with grids of different width create defect modes with relatively sharp peaks, which are tunable. The size of the PBG structures was strongly reduced compared to the simple metallic meshes, for the same frequency characteristics, by using a supporting dielectric substrate for the metallic grids. The application of  $\text{Al}_2\text{O}_3$  wafers as a supporting material for a metallic grid pattern leads to a reduction of the size of the simple MPBG structure by a factor of 3. This can be further improved by using high dielectric microwave materials. Dielectric materials with tunable properties may open new perspectives for the application of "clever" PBG structures in microwave technology.

Recent activities are targeting the fabrication of monolithic MPBG structures consisting of microwave dielectrics patterned with metallic grids for applications in microwave technology.

## 6. CONCLUSIONS

Laser micro-machining and LIGA are two very useful techniques for the fabrication of PBG structures. LIGA has been selected for its ability to produce accurate and reproducible 3-D PBGs up to the THz spectral range, while laser machining has been selected for its versatility to producing effective tuneable 2-D metallic structures in the millimeter wave regime. Results presented

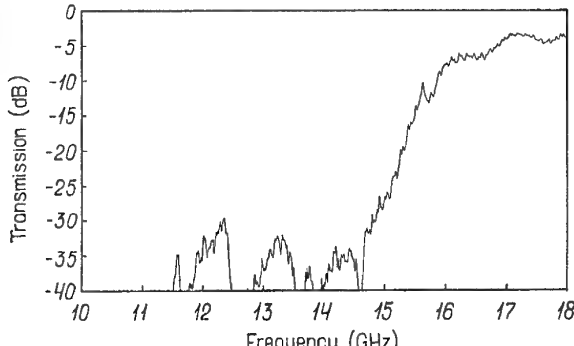


Fig. 9. Transmission profile for a periodic structure with four  $\text{Al}/\text{Al}_2\text{O}_3$  layers. The lattice constant of the structure is 5 mm, and the width of the Al wires is 2 mm.

have demonstrated the advantages of these two techniques for high quality, reproducible and low-cost PBGs and their potential for immediate application in the production of novel components in quantum optics.

## REFERENCES

- [1] *Photonic Band Gaps and Localization*, ed. C.M. Soukoulis, (Plenum: New York 1993), Proceedings of the NATO ARW.
- [2] *Photonic Band Gap Materials*, ed. C.M. Soukoulis, NATO ASI, Series E, vol. 315.
- [3] S. John // *Phys. Rev. Lett.* **58** (1987) 2486.
- [4] E. Yablonovitch, T.J. Gmitter and K.M. Leung // *Phys. Rev. Lett.* **67** (1991) 2295.
- [5] E. Yablonovitch and K.M. Leung // *Nature* **351** (1991) 278.
- [6] K.M. Ho, C.T. Chan and C.M. Soukoulis // *Phys. Rev. Lett.* **65** (1990) 3152.
- [7] W. Robertson, G. Arjavalingan, R.D. Meade, K.D. Brommer, A.M. Rappe and J.D. Joannopoulos // *Phys. Rev. Lett.* **68** (1992) 2023.
- [8] G. Feiertag, E. Ehrfeld, H. Freimuth, H. Kolle, H. Lehr, M. Schmidt, M.M. Sigalas, C.M. Soukoulis, G. Kiriakidis, T. Pedersen, J. Kuhl and W. Koenig // *Appl. Phys. Lett.* **71** (1997) 1441.
- [9] N. Katsarakis, E. Chatzitheodoridis, G. Kiriakidis, M.M. Sigalas, C.M. Soukoulis, W.Y. Leung and G. Tuttle // *Appl. Phys. Lett.* **74** (1999) 3263.
- [10] M.D.B. Charlton, S.W. Roberts and G.J. Parker // *Materials Science and Engineering B-Solid State Materials for Advanced Technology* **49** (1997) 155.
- [11] J.M. Gerard, A. Izrael, J.Y. Marzin, R. Padjen and F.R. Ladan // *Solid State Electronics* **37** (1994) 1341.

- [12] T. Krauss, Y.P. Song, S. Thoms, C.D.W. Wilkinson and R.M. Delarue // *Electronic Letters* **30** (1994) 1444.
- [13] V. Berger, O. Gauthier Lafaye and E. Costard // *Electronic Letters* **33** (1997) 425.
- [14] R.D. Meade, K.D. Brommer, A.M. Rappe and J.D. Joannopoulos // *Appl. Phys. Lett.* **61** (1992) 495.
- [15] D. Cassagne, C. Jouanin and D. Bertho // *Phys. Rev. B* **53** (1996) 7134.
- [16] H.W. Lau, G.J. Parker, R. Greef and M. Hoelling // *Appl. Phys. Lett.* **67** (1995) 1877.
- [17] D. Labilloy, H. Benisty, C. Weisbuch, T.F. Krauss, R.M. Delarue, V. Bardinal, R. Houdre, U. Oesterle, D. Cassagne and C. Jouanin // *Phys. Rev. Lett.* **79** (1997) 4147.
- [18] T.F. Krauss, B. Vogeles, C.R. Stanley and R.M. Delarue // *IEEE Photonics Technology Letters* **9** (1997) 176.
- [19] C.T. Chan, K.M. Ho and C.M. Soukoulis // *Europhys. Lett.* **16** (1991) 563.
- [20] J.G. Fleming and S.Y. Lin // *Optics Letters* **24** (1999) 49.
- [21] W. Ehrfeld and H. Lehr // *Radiat. Phys. Chem.* **45** (1995) 349.
- [22] F.J. Pantenburg and J. Mohr // *Nuclear Instruments and Methods in Physics Research B* **97** (1995) 551.

# A MATHEMATICAL MODEL OF METAL FILMS DEPOSITION FROM PHOTOACTIVE COMPOUND SOLUTIONS ON SOLID-LIQUID INTERFACE

S.A. Kukushkin and S.V. Némenat

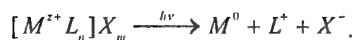
Institute of Problems of Mechanical Engineering, RAS, Vas. Ostrov, Bolshoj pr. 61, 199178, St-Petersburg, Russia

Received: October 18, 1999

**Abstract.** The kinetics of the growth of thin metal films from solutions of photoactive chemical coordination compounds irradiated by light at a certain wavelength has been theoretically investigated. In the framework of our mathematical model the time dependencies of the basic characteristics of the film growth process (size distribution function, density of nucleation, concentration of metal on the surface) have been computed. They proved to be in accordance with the experimental data. It is shown that the flux of metal (substance) from the solution onto the surface of the substrate can be derived from the stationary diffusion equation with the added term taking into account the influence of the photochemical substance source. It may be inferred that the variation of light intensity, in great range, keeps the kinetics of the process of film deposition out of the drastic changes.

## 1. INTRODUCTION

The processes of metal films formation and growth on solid substrates are of great importance from both theoretical and practical viewpoints [1]. In the papers [2-5], the process of obtaining Ag, Au, Cu films on flat quartz substrates in the solutions of photoactive chemical coordination compounds was investigated experimentally. The essence of this method is the following. Let us consider a solution of the coordination compound  $[M^{z+}L_n]X_m$ , where  $M^{z+}$  is the central metal atom ( $z^+$  is the oxidation level); L denotes innersphere ligands; X denotes outersphere counterions. If ligand to metal charge transfer ( $L \rightarrow M$ ) occurs in this compound, the irradiation of solution by light at the wavelength  $\lambda = \lambda_{L \rightarrow M}$  results in the reduction of the metal atom. By carrying the irradiation on, the central metal atom can be reduced to the zeroth valence state. Thus, we can write the scheme of the entire process as



One should put the substrate to be deposited on the bottom of the vessel filled with the solution. If we direct a light beam from above, its intensity decreases according to the Lambert-Buger-Behr law (Fig. 1).

Zeroth valence metal atoms generated by light will diffuse towards the substrate and be adsorbed on it. When the critical concentration of metal on the substrate surface is reached, the growth of new crystal metal phase starts.

It was noted in [2-5], that the essential feature of films obtained in this way is the narrow size distribution of grains in the film. In those papers, on the basis of the Volmer-Weber theory [6] the qualitative explanation of results was proposed. The process of formation and growth of a new phase on the surface is the complicated multistage one [7], and the Volmer-Weber theory does not provide any exact quantitative description.

In our opinion, the method described above is very constructive and interesting for problems of films growing. In this work, we investigated theoretically the time dependencies of the basic characteristics of the growing film, on the basis of modern film growth ideas, presented in the publications [1, 7].

## 2. FLUX OF METAL ATOMS ONTO THE SUBSTRATE

In this work, the initial stage of the film condensation on the solid substrate was investigated. The substrate is considered to be a homogeneous continuous surface. Thermal effects of crystallization and adsorption are neglected. Passing through the solution, the light interacts with molecules of coordination compounds. That results in the formation of zeroth valence metal atoms. The power of metal atoms source is given by

$$g(x) = I_0 \varphi \alpha \exp[-\alpha x], \quad (1)$$

Corresponding author: S.V. Némenat, e-mail: nem@ipme.ru

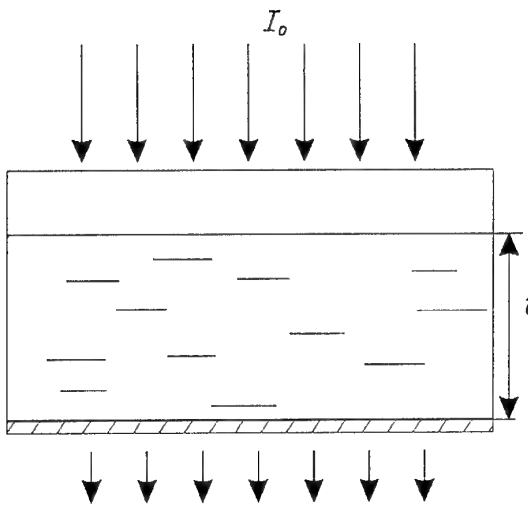


Fig. 1. The scheme of the process of photochemical film deposition;  $l$  — the thickness of the solution layer,  $I_0$  — the incident light intensity.

where  $I_0$  is the incident light intensity;  $\alpha$  is the absorption coefficient;  $\gamma$  is the quantum yield. The absorption coefficient  $\alpha$  can be represented by  $\alpha = 2.3\epsilon c_{\text{complex}}$ , where  $\epsilon$  is the extinction;  $c_{\text{complex}}$  is the concentration of absorbing centres in the solution. Here, we suppose that  $c_{\text{complex}}$  is constant. If the height of solution  $l$  (Fig. 1) is small, the probability of the formation of metal clusters in the bulk of solution (homogeneous nucleation) vanishes. In this case, the flux of metal onto the substrate can be derived from the 1D stationary diffusion equation written by

$$D\Delta c(x) + g(x) = 0, \quad (2)$$

where  $\Delta$  denotes the Laplacian;  $D$  is the diffusion coefficient; the power of source is given by the Eq. 1. We make use of the stationary diffusion equation for the following reasons:

1. the source of metal atoms is stationary
2. we suppose that the characteristic time of photochemical reaction is much less than that of diffusion and, i.e. the photochemical reaction is not the ratelimiting stage.

The boundary conditions to the Eq. 2 are

$$\left. \frac{dc}{dx} \right|_{x=0} = 0, \quad (3)$$

$$c(l) = c_s^*. \quad (4)$$

It means that the flux of metal into the system at the upper boundary of solution ( $x=0$ ) misses and the concentration of metal on the surface ( $x=l$ ) is constant and equal to  $c_s^*$ .

In fact, some average time-dependent concentration of adsorbed atoms on the substrate exceeding  $c_s^*$  exists. It is the reduced difference of these concentrations being referred to as the supersaturation

$$\xi(t) = \frac{c_v(t) - c_s^*}{c_s^*}, \quad (5)$$

that is the driving force for the phase transformation on surface. However, due to the growth is carried out at room temperature and the solubility of metal is very low, the equilibrium concentration of metal  $c_s^*$  is also low. This results in formation of surface metal islands at small supersaturations. Therefore, following [1, 7, 8], we assume that the application of the boundary condition (4) is enough satisfactory. By differentiation of the solution of the Eq. 2 with the boundary conditions (3) and (4), we can derive the form of the flux of metal to the surface

$$J_s = I_0 \phi(1 - \exp(-\alpha l)). \quad (6)$$

### 3. METAL ISLANDS FORMATION PROCESSES

According to the paper [7], a process of new phase formation goes through three basic stages. The first stage is the fluctuation formation of new phase nuclei. It is described by the Zeldovich theory, modified for the formation on the surface [7]. During this stage, the stationary flux of nuclei, which are spherical segments, has the form [7]:

$$I(\xi) = K(\xi + 1) \ln(\xi + 1) \exp\left(-\frac{b}{\ln^2(\xi + 1)}\right), \quad (7)$$

where  $\xi$  is the supersaturation;  $b = (\sigma / (kT))^3 4\pi v$ ,  $\sigma$  is the surface tension;  $v$  is the volume per atom in nucleus;  $K$  is the proportionality coefficient depending on the diffusion coefficient of adatoms. The time lag is estimated by:

$$t_s = \frac{1}{-F'(n_{cr}) W(n_{cr})}, \quad (8)$$

where  $n_{cr}$  is the number of atoms in critical nucleus;  $F(n)$  is the Helmholtz energy of nucleus taking form of a spherical segment;  $W(n)$  is the diffusion coefficient in the size space taking into account the probability of random eliminating or joining atoms to nucleus (the fluctuations of nucleus in the size space) [9].

$$F(n_{cr}) = \frac{b}{\ln(\xi + 1)} \quad (9)$$

At  $t > t_s$  the second stage starts. This is the process of formation of new phase islands in the system. This stage is described by the system of equations:

$$\frac{\partial f(n; t)}{\partial t} + \frac{\partial(\nu(n; t) f(n; t))}{\partial n} = 0, \quad (10)$$

where  $\nu(n; t) \equiv \frac{dn}{dt}$  is the linear rate of nucleus growth, written as

$$\nu(n; t) = a \xi(t) n^{-m}, \quad (11)$$

where  $a$  and  $m$  are coefficients depending on the mechanism of nuclei growth,

$$\frac{\xi_0}{\xi(t)} - 1 = \int_0^t J_s dt - k \int_0^\infty \int f(n; t) n dndt, \quad (12)$$

where  $k$  is the coefficient depending on the metal under investigation. The equation above represents the matter conservation. The equation (10) should be complemented by the initial and boundary conditions [7, 10]

$$f(n; 0) = 0, \quad f(n_c; t) = \frac{I(\xi(t))}{\nu(n; t)_{n=n_c}}. \quad (13)$$

The method of solution of this equations system was developed in the paper [10]. The solution of the system allows us to derive the time dependencies of the basic characteristics of the film growth process:

1. the supersaturation  $\xi(t)$  is as

$$\xi(t) = \xi_0 \frac{1}{1 + \frac{1}{\Gamma} T^k(t) \phi_k(T(t))} \quad (14)$$

2. the frequency of nuclei formation  $I(t)$  is as

$$I(t) = I(\xi_0) \frac{\exp[-T^k(t) \phi_k(T(t))]}{1 + \frac{1}{\Gamma} T^k(t) \phi_k(T(t))} \quad (15)$$

3. the size distribution function  $f(n; t)$  is as

$$f(n; t) = \frac{1}{k+1} n^{-\frac{k}{k+1}} \frac{I(\xi_0)}{\alpha \xi_0} \times \exp\left(-(T(t) - \frac{\rho(n)}{\alpha t_k \xi_0})^k \phi_k(T(t) - \frac{\rho(n)}{\alpha t_k \xi_0})\right), \quad (16)$$

where the auxiliary function is  $\rho(n) = \frac{n^{m+1} - n_c^{m+1}}{m+1}$ .

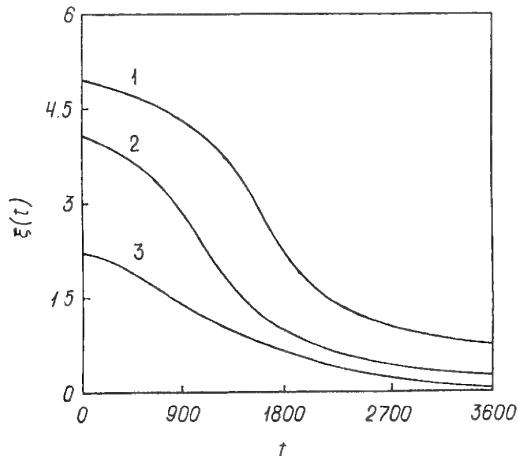


Fig. 2. The time dependence of supersaturation on the surface at different values of the incident light intensity: curve 1 –  $10^{20}$  quantum·m<sup>-2</sup>·s<sup>-1</sup>; curve 2 –  $10^{19}$  quantum·m<sup>-2</sup>·s<sup>-1</sup>; 3 –  $10^{18}$  quantum·m<sup>-2</sup>·s<sup>-1</sup>;  $t$  – time (s),  $\xi(t)$  – supersaturation (non-dimensional quantity).

The formulae (14–16) contain the parameter  $\Gamma$  – quantity, which is inverse with respect to the expansion small parameter. This parameter has the very important property:  $\Gamma \approx n_{cr}$ . All other symbols in these formulae correspond to those in the origin paper [10].

#### 4. RESULTS OF CALCULATIONS AND CONCLUSIONS

Assuming that the growing film is determined by the following constants:  $I_0 = 10^{20}$  quantum·m<sup>-1</sup>·s<sup>-1</sup>,  $\gamma = 0.8$ ,  $\alpha = 50$  m<sup>1</sup>,  $l = 2 \cdot 10^{-4}$  m [2–5],  $D = 10^{-9}$  m<sup>2</sup>·s<sup>-1</sup>,  $\nu = 10^{-30}$  m<sup>3</sup>,  $c_s^* = 10^{20}$  atoms·m<sup>-2</sup>,  $\sigma = 1$  J·m<sup>-2</sup>,  $k = 1$ ,  $a = 10^{14}$ ,  $K = 10^{32}$ ,  $\tau_r = 10^{-2}$  s [11],  $S_{surf} = 10^{-4}$  m<sup>2</sup>,  $T = 298$  K.

Thus the value of the steady flux (Eq. 6) is  $2 \cdot 10^{18}$  atoms·m<sup>-2</sup>·s<sup>-1</sup>.  $n_{cr} \approx \Gamma = 53$ . That criterium proves that the solution obtained by the small parameter method sufficiently describes the kinetics of the film growth. The time lag value is  $t_s = 1.8 \cdot 10^{-6}$  s.

The results of calculations are presented in Figs. 2–5.

It is seen from Fig. 4, the size distribution takes the form of a bell. It is the form which is predicted by the theory [1, 7].

We have calculated the time dependencies of the size distribution function, the frequency of nucleation and the supersaturation on the surface at three different values of the incident light intensity of  $10^{20}$ ,  $10^{19}$  and  $10^{18}$  quantum·m<sup>-1</sup>·s<sup>-1</sup>. The variation of light intensity, in great range, keeps the kinetics of the process of film deposition out of the drastic changes.

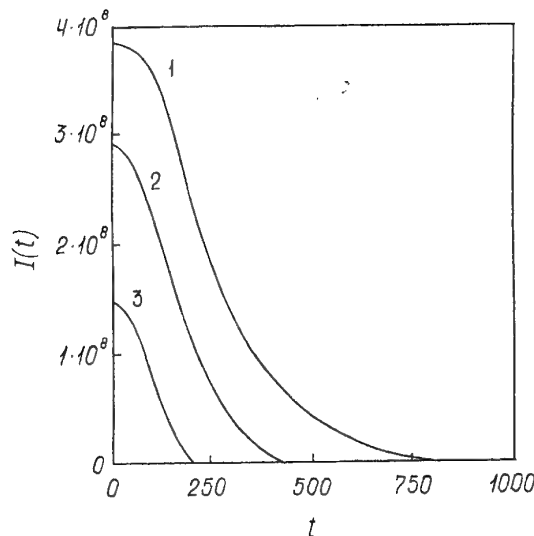


**Fig. 3.** The time dependence of nucleation frequency on the surface at different values of the incident light intensity: curve 1 —  $10^{20}$  quantum· $m^{-2}\cdot s^{-1}$ ; curve 2 —  $10^{19}$  quantum· $m^{-2}\cdot s^{-1}$ ; 3 —  $10^{18}$  quantum· $m^{-2}\cdot s^{-1}$ ;  $t$  — time (s),  $I(t)$  — nucleation frequency ( $s^{-1}$ ).

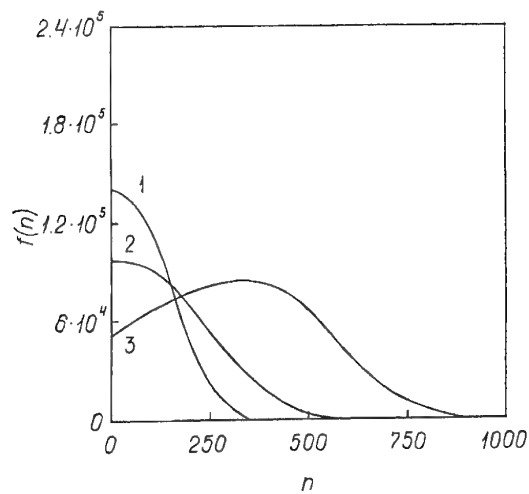


**Fig. 4.** The size distribution function at the incident light intensity of  $I_0 = 10^{20}$  quantum· $m^{-2}\cdot s^{-1}$  and the irradiation time: curve 1 — 5 min; curve 2 — 10 min; curve 3 — 40 min;  $n$  — the number of nuclei (non-dimensional quantity),  $f(n)$  — the size distribution function (non-dimensional quantity).

## ACKNOWLEDGMENTS

This work was supported by Russian Found for Basic Research (grant № 99-03-32768). We would like to thank Prof. I.P. Kalinkin for helpful discussions.

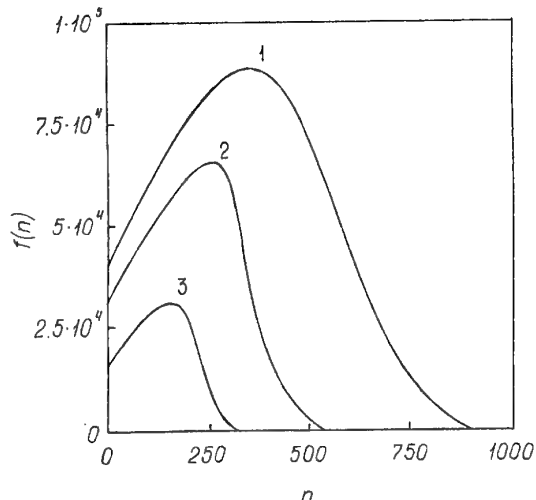


**Fig. 5.** The size distribution function at the irradiation time of 40 min and the incident light intensity: curve 1 —  $10^{20}$  quantum· $m^{-2}\cdot s^{-1}$ ; curve 2 —  $10^{19}$  quantum· $m^{-2}\cdot s^{-1}$ ;  $10^{18}$  quantum· $m^{-2}\cdot s^{-1}$ ;  $n$  — the number of nuclei (non-dimensional quantity),  $f(n)$  — the size distribution function (non-dimensional quantity).

## REFERENCES

- [1] S.A. Kukushkin and V.V. Slyozov, *Disperse Systems on the Surface of Solids (Evolution Approach): Mechanisms of Thin Films Formation* (Nauka, St.-Petersburg, 1996), (in Russian).
- [2] T.B. Boitsova, A.V. Loguinov and V.V. Gorbunova // *Zhurnal Prikladnoi Khimii* **70** (1997) 1585.
- [3] A.V. Loguinov, L.V. Alexeeva, V.V. Gorbunova, G.A. Shaguisultanova and T.B. Boitsova // *Zhurnal Prikladnoi Khimii* **67** (1994) 803.
- [4] T.B. Boitsova, V.V. Gorbunova and A.V. Loguinov // *Zhurnal Obshchei Khimii* **67** (1997) 1741.
- [5] A.V. Loguinov, T.B. Boitsova and V.V. Gorbunova // *Macromolecular Symposia* **136** (1998) 103.
- [6] M. Volmer, *Kinetik der Phasenbildung* (Steinkopf, Dresden, 1939).
- [7] S.A. Kukushkin and A.V. Osipov // *Physics-Uspekhi* **41** (1998) 983.
- [8] S.A. Kukushkin and A.V. Osipov // *Technical Physics* **40** (1995) 615.
- [9] V.V. Slyozov and S.A. Kukushkin // *Physics of the Solid State* **38** (1996) 239.
- [10] S.A. Kukushkin and A.V. Osipov // *Journal of Chemical Physics* **107** (1997) 3247.
- [11] A.V. Osipov // *Physics of the Solid State* **36** (1994) 664.

# ENHANCED DIFFUSION NEAR AMORPHOUS GRAIN BOUNDARIES IN NANOCRYSTALLINE AND POLYCRYSTALLINE SOLIDS

R.A. Masumura<sup>1</sup> and I.A. Ovid'ko<sup>2</sup>

<sup>1</sup>Naval Research Laboratory, Washington, DC 20375, USA

<sup>2</sup>Institute of Problems of Mechanical Engineering,

Russian Academy of Sciences, Bolshoi 61, Vas. Ostrov, St. Petersburg, 199178, Russia

Received: September 23, 1999

**Abstract.** A theoretical model is constructed that describes diffusion processes enhanced by the elastic interaction of the diffusing species and amorphous grain boundaries in nanocrystalline and polycrystalline solids. A partial differential equation governing evolution of the spatially inhomogeneous concentration of the diffusing species near amorphous grain boundaries is numerically solved. It is shown that the enhanced diffusion essentially influences the growth of amorphous grain boundaries in solids under irradiation and thermal treatment as well in sintered ceramics and is capable of contributing to the anomalously fast diffusion in nanocrystalline solids.

## 1. INTRODUCTION

The process of the diffusion, where one species rearranges its configuration in a lattice (a solid in this case) in response to an external force, is an attempt to approach equilibrium. When a concentration gradient exists as the only driving force, this irreversible process can be concisely formulated leading to a second order parabolic partial differential equation (PDE). The solution of this PDE has been determined for many types of boundary and initial conditions and geometries.

If additional driving forces are present due to electrical, magnetic, thermal or elastic fields, the appropriate PDE can be formulated subject to simplifying assumptions. The question now becomes, whether this additional driving force will enhance or retard the flow of diffusing species thorough the lattice. In particular, we are interested in the effect of an amorphous intergranular boundary dislocation stress field has on the diffusion of various species in nanocrystalline and polycrystalline solids. Such boundaries frequently exist in sintered nanostructured and polycrystalline ceramics [1-5] as well in monophase and composite solids under irradiation and thermal treatment, where diffusion- and irradiation-induced amorphization processes often start to occur at grain boundaries [6,7]. Amorphous grain boundaries in sintered ceramics are characterized by a chemical composition that is different from that of adjacent crystalline grains as well by a nano-scaled

thickness whose value is essentially constant within a ceramic sample. These grain boundaries are dependent on only the chemical composition and insensitive to misorientation parameters of the boundaries (see [1,8] and references therein). Amorphous grain boundaries in monophase and composite solids under irradiation and thermal treatment play the role as nuclei for enhanced diffusion- and irradiation-induced amorphization, where the boundaries transform into extended amorphous layers with the meso- and macro-scale thickness growing parallel with the diffusion and irradiation processes [6,7]. Recently, a model [9,10] has been suggested describing the role of elastic distortions in the formation of amorphous grain boundaries. This model, however, does not quantitatively take into account the effect of diffusion on evolution of amorphous grain boundaries after they have been formed. At the same time, this effect is important for an adequate description of both the structural features and the properties of nanocrystalline and polycrystalline solids containing amorphous grain boundaries.

The model presented here is an initial attempt to understand the role of enhanced diffusion in evolution of amorphous grain boundaries in (i) sintered ceramics and (ii) monophase and composite solids under irradiation and thermal treatment. The model also is concerned with the contribution of amorphous grain boundaries to enhanced diffusion in nanostructured solids (often exhibiting the outstanding diffusional

Corresponding author: I.A. Ovid'ko, e-mail: ovidko@def.ipme.ru

properties [11,12]), which is related to elastic interaction of amorphous grain boundaries and the diffusing species. As such, we have assumed that the crystalline grains are separated by an amorphous grain boundary layer that provides the source of the diffusing species. To retain the flavor of dislocation model of a simple tilt boundary, we will consider that a double wall of dislocations separate the amorphous layer. We further assume that dislocations do not interact with each other.

We will discuss the development of the appropriate PDE and the elastic interaction from a double wall of dislocations. This will lead to the formulation of the interaction energy that will be used in the PDE whose solution is determined numerically. Finally, we will discuss the results of the numerical analysis.

## 2. MATHEMATICAL FORMULATION

The flux or current density of a diffusing species in the presence of a concentration gradient is given as,

$$\vec{j} = -D \nabla C, \quad (1)$$

where  $D$  is the diffusivity and  $C$  is the concentration. If there is an elastic interaction between the diffusing species and a stress field in a homogenous, linear and isotropic solid, Eq. 1 is modified as [13]

$$\vec{j} = - \left[ D \nabla C + \frac{C}{kT} \nabla \varepsilon \right], \quad (2)$$

where  $\varepsilon$  is the interaction energy,  $k$  is Boltzmann's constant and  $T$  is the absolute temperature of the diffusion process. It is assumed that the mobility  $\mu$ , caused by the force from the strain gradient is the same as in the chemical potential force,

$$\mu = \frac{D}{kT}. \quad (3)$$

It will be assumed that the diffusivity is constant and independent of both concentration and strain.

Using the continuity equation, Eq. 2 can be recast as

$$\frac{\partial C}{\partial t} = D \left( \nabla^2 C + \frac{1}{kT} \nabla C \cdot \nabla \varepsilon \right), \quad (4)$$

since

$$\nabla^2 \varepsilon = 0, \quad (5)$$

due to the absence of any internal body forces. Eq. 4 along with the appropriate initial and boundary conditions will be solved to determine how the concentration is affected by the elastic interaction.

A formulation for the interaction energy based upon a grain boundary model is required. For nanocrystalline and polycrystalline materials, an appropriate model is the one proposed by Kolesnikova et al. [9] and Ovid'ko and Reizis [10] where an amorphous grain boundary layer occurs as described below between the nanosized grains.

## 3. DOUBLE WALL MODEL

In the framework of dislocation-structural-unit models [14,15], a conventional tilt grain boundary in a crystal can be treated as a periodic wall array of edge grain boundary dislocations whose spatial positions and Burgers vectors are strictly determined by parameters (misorientation, etc.) of the boundary. In this model representation, the elastic fields and the elastic energy density of a tilt boundary are those of the corresponding array of grain boundary dislocations [16,17]. Following [9,10], transformation of a conventional tilt grain boundary into an amorphous grain boundary is associated with a re-arrangement of its grain boundary dislocation ensemble. In doing so, due to the fact that the amorphous disordered structures do not impose strict limitations on both spatial positions and Burgers vectors of grain boundary dislocations, such dislocations in a new, amorphous boundary are arranged in the way decreasing their elastic energy density. The discussed decrease of the elastic energy density causes the basic driving force  $F_e$  for the transformation of a conventional tilt boundary into an amorphous boundary. This force is calculated in the model [9,10] which to a first approximation describes the amorphous boundary to be of finite width,  $\lambda$ , with dislocation arrays at each of the interfaces between amorphous and the crystalline grain as shown in Fig. 1. Following the

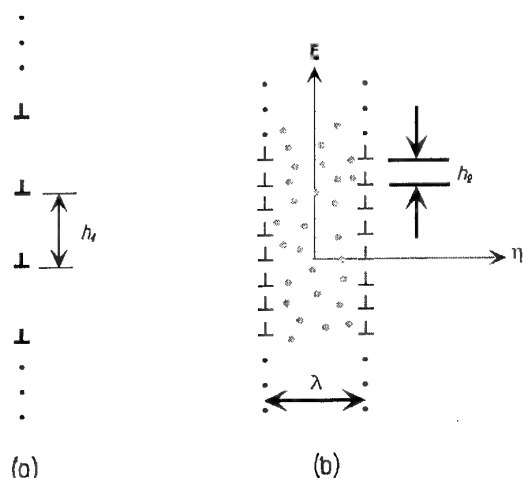


Fig. 1. (a) Single dislocation array and (b) double wall with amorphous grain boundary of width  $\lambda$ .

calculations of references [9] and [10], the driving force  $F_{el}$  is large at  $\lambda \leq h_2$ , and  $\approx 0$  at  $\lambda > h_2$ , where  $h_2$  is the period of the dislocation walls (Fig. 1). The elastic interaction between the two dislocation walls exists in only the range of  $\lambda \leq h_2$ ; the walls, in general, do not interact elastically at  $\lambda > h_2$ . As a corollary, evolution of the amorphous grain boundary at  $\lambda = h_2$  is caused by the thermodynamic force  $F'$  related to other factors other than the decrease of the elastic energy density. More precisely, the force  $F'$  is as follows [10]:

$$F' = -\varepsilon_{a-c}(\lambda) - (2\kappa + \lambda) \frac{d\varepsilon_{a-c}}{d\lambda}, \quad (6)$$

where  $\varepsilon_{a-c}$  denotes the difference between the free energy densities of the amorphous and crystalline phases, and  $\kappa$  the characteristic spatial scale of structural inhomogeneities in the amorphous phase. The term  $\varepsilon_{a-c}$  strongly depends on the chemical composition which, in general, is spatially inhomogeneous in the vicinity of the amorphous boundary and can evolve in time due to diffusion. In these circumstances, the  $F'$ -induced evolution of the amorphous grain boundary is sensitive to the diffusion processes in its vicinity. On the other hand, the stress field of the boundary influences the diffusion processes and, as a corollary, evolution of the boundary. The elastic interaction between the diffusing species and the stress field is related to the sum of the normal stresses. For a double wall of non-interacting dislocation infinite arrays a distance  $\lambda$  apart the sum of the normal stresses is,

$$\sigma_n = -\frac{Gb_2(1+\nu)}{2(1+\nu)h_2} \omega(2\pi\xi), \quad (7)$$

where

$$\omega(\eta, \xi) = \frac{\sin(2\pi\xi)}{\cosh\{2\pi(\eta - \frac{\lambda^*}{2})\} - \cos(2\pi\xi)} + \frac{\sin(2\pi\xi)}{\cosh\{2\pi(\eta + \frac{\lambda^*}{2})\} - \cos(2\pi\xi)}, \quad (8)$$

and letting  $\eta = x/h_2$ ,  $\xi = y/h_2$  and  $\lambda^* = \lambda/h_2$  for the coordinate system given in Fig. 1 where the dislocation walls are symmetrical located at  $x = \pm\lambda/2$ . The shear modulus and Poisson's ratio are denoted by  $G$  and  $\nu$ , respectively.

#### 4. INTERACTION ENERGY

We assume the volume of the diffusing and host species are different and thus giving rise to an elastic interaction. On the average, let  $\Delta V$  be the volume change

and this volume difference interacts with a homogenous applied stress field. It can be shown that the elastic interaction is given as

$$\varepsilon = (\Delta V)\Theta, \quad (9)$$

where  $\Theta = -\sigma_{ii}/3$ , the hydrostatic component of the stress field. This interaction will alter the total energy of the system depending upon the sign of the product.

In Fig. 2a is plotted the contours of constant normalized interaction energy (i.e.,  $\omega(\eta, \xi)$ ) for a strip  $|\xi| \leq 0.5$ . As expected, a large energy gradient exists near the dislocation,  $\xi = 0$  due to the elastic singularity of the dislocation core. Depending upon the volume change, this elastic interaction will enhance diffusion. For illustrative purposes, it will be assumed that  $\Delta V > 0$ . In Fig. 2a, from a qualitative viewpoint, the diffusing species would tend to migrate below the extra dislocation half plane to lower their total energy. A spherical point defect interacting with a single edge dislocation also exhibits this behavior [18].

The force,  $\bar{f}$ , on the migrating species is determined from  $-\nabla\varepsilon$  and the results are shown in Fig. 2b for the corresponding interaction energy of Fig. 2a. The diffusing species will tend to move away from above the dislocation and migrate to the edge of the extra half plane of the dislocation. This periodic case of a tilt boundary is different from that for an isolated edge dislocation in that the diffusing species in the upper one fourth of the strip diffuses to the next strip above. This is only a qualitative assessment and should serve as guide when a concentration gradient is not considered.

#### 5. NUMERICAL SOLUTION

Before solving Eq. 4, the initial and boundary conditions must be specified. We need to only consider one strip,  $|\xi| < 1/2$ , since we assume the grain boundary to be modeled by an infinite array of dislocations and can utilize a periodic boundary condition,  $C(\eta, -1/2, t) = C(\eta, 1/2, t)$  for  $\eta \geq 0$ . We will assume that the amorphous layer in between the nanosized grains will be an undiminished source of the diffusing species, thus,  $C(0, \xi, t) = 1.0$  for  $|\xi| < 1/2$ . Since the dislocation stresses from a regular array are short range in nature, it is reasonable to utilize  $C(\infty, \xi, t) = 0$  in each and every strip. The above boundary conditions are valid for  $t > 0$ . For an initial condition, we will assume that each strip is devoid of any of the diffusing species at  $t = 0$  leading to  $C(\eta, \xi, 0) = 0$ .

Eq. 4 is normalized for computational purposes by rescaling time and letting the material coefficients become  $\tau = Dt$  and  $\gamma^* = \frac{DGb_2(1+\nu)}{2kt(1-\nu)h_2}$ . The normalized computational form becomes

The normalized computational form becomes

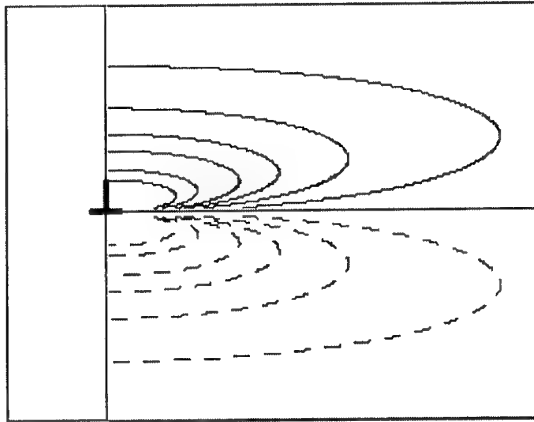


Fig. 2(a) shows the normalized interaction energy,  $\omega$ . Above the dislocation,  $\omega > 0$  (solid) while below  $\omega < 0$  (dashed) for  $\Delta V > 0$ . The area to the left of the dislocation is one half of the amorphous layer.

$$\frac{\partial C}{\partial \tau} = \nabla^2 C + \gamma^* \nabla C \cdot \nabla \omega \quad (11)$$

with the boundary conditions for  $t > 0$ ,

$$C(\eta, -1/2, \tau) = C(\eta, 1/2, \tau) \text{ for } \eta \geq 0, \quad (12)$$

$$C(0, \xi, \tau) = 1.0 \text{ for } |\xi| < 1/2, \quad (13)$$

$$C(\infty, \xi, \tau) = 0 \text{ for } |\xi| < 1/2, \quad (14)$$

and the initial condition at  $\tau = 0$ ,

$$C(\eta, \xi, 0) = 0 \text{ for } \eta > 0 \text{ and } |\xi| < 1/2. \quad (15)$$

An alternating-direction-implicit (ADI) method is utilized to obtain a numerical solution of Eq. 11. Each time step is divided equally in half. In the first half, a partial solution is determined by reducing the PDE to a one-dimensional problem in one of the orthogonal coordinates while keeping the other fixed. In the second half, the PDE is now solved in the other coordinate direction using the partial results obtained in the first half time step. This algorithm has the advantage of requiring a tridiagonal equation solver and is relatively stable (unconditionally if the coefficients of the PDE are constant). The  $\eta$ -direction partial solution requires a slight modification to the tridiagonal solver to account for periodic nature of the boundary conditions but it still retains the usual banded form. We have chosen to do the analysis first in the  $\eta$ -direction since the elastic fields are short-ranged in  $\xi$ .

The finite difference equations are based upon the usual five atom centered-computational molecule to approximate the Laplacian (spatial coordinates) and a two point approximation for the temporal first deriva-

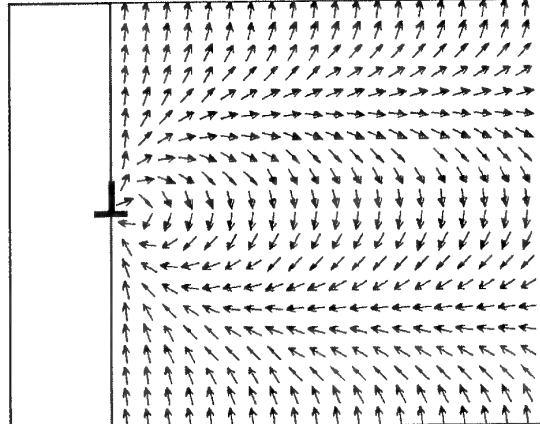


Fig. 2(b) indicates the flow of diffusant ( $\Delta V > 0$ ) corresponding to interaction energy shown in Fig. 2a as determined from  $-\nabla \omega$ . For clarity, each vector is normalized to one. The forces away from the dislocation are greatly attenuated. The area to the left of the dislocation is one half of the amorphous layer.

tive. Using equal increments for the spatial coordinates,  $\Delta \xi = \Delta \eta$  and utilizing a normalized time increment  $\Delta \tau$ , and rescaling  $\gamma$  for computation clarity,

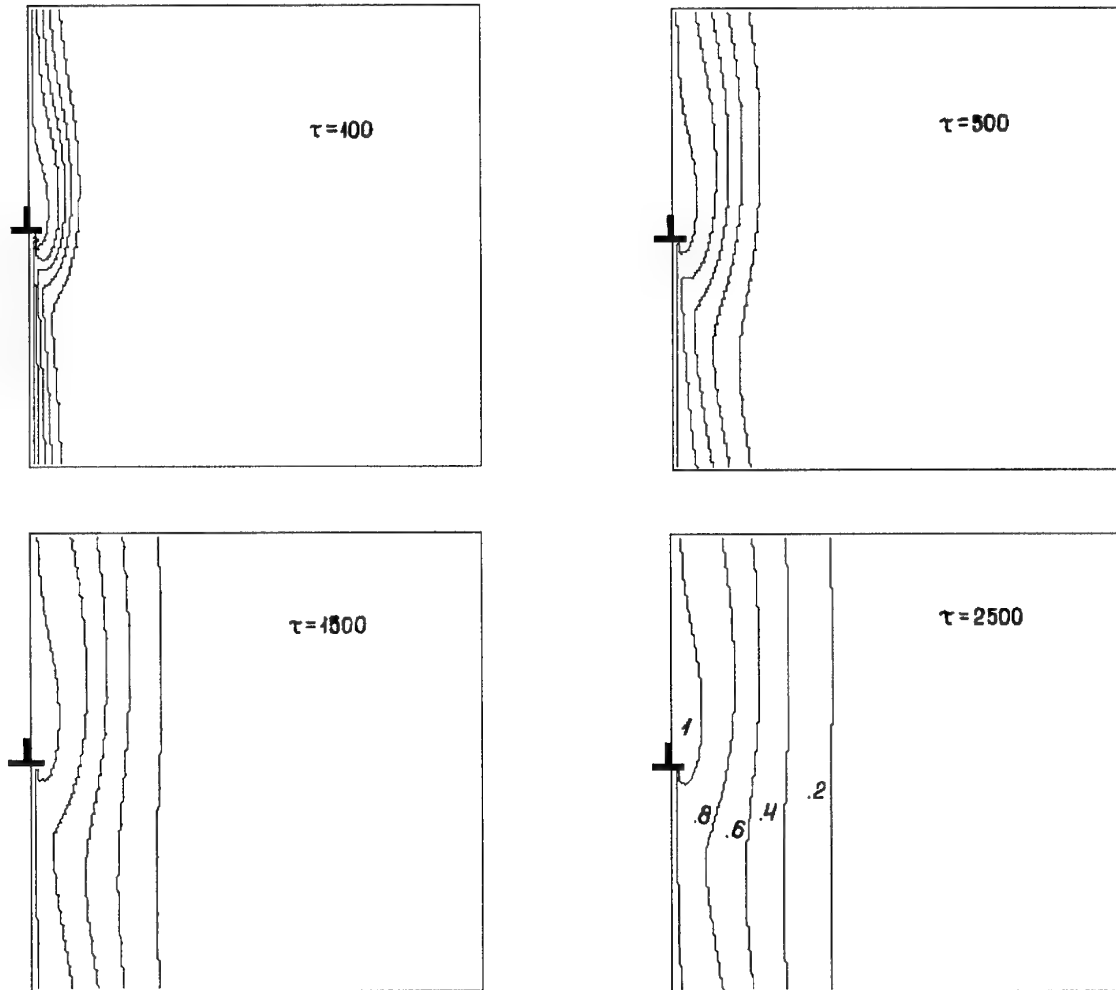
$$\gamma^* = 4\gamma(\Delta \xi), \quad (16)$$

Eq. 12 can be approximated by finite difference form amenable for numerical computation.

For the actual computation, a strip  $|\xi| \leq 1/2$  high and  $0 \leq \eta \leq 3$  was used. The grid for this rectangle was divided into 100 and 300 equal increments for the  $\xi$ - and  $\eta$ -directions, respectively. The singularity of stress field was avoided by placing the dislocation in between the grid points. For each time step, the mass accumulation,  $M(t)$ , was determined by numerically integrating the normalized concentration over the computational rectangle.

To check the accuracy of the numerical scheme, an initial run was made with the interaction set to zero. This case corresponds to diffusion between two planes (one-dimensional problem). These results agreed with the analytical solution lending confidence to the numerical algorithm. Runs were made to explore the effect of the elastic interaction between grain boundary dislocations and diffusing species. First was to determine the role of the "strength" of the interaction as manifested through  $\gamma^*$  and second was to determine the effect of spacing between the dislocations (width of amorphous layer) in the wall,  $\lambda$ , on the diffusion process.

A typical run for values of  $\gamma^* = 3$  and  $\lambda = 1$  is shown in Fig. 3 for various normalized times. The concentration is larger above the dislocation since the flow lines from Fig. 2a indicate diffusion away from this area



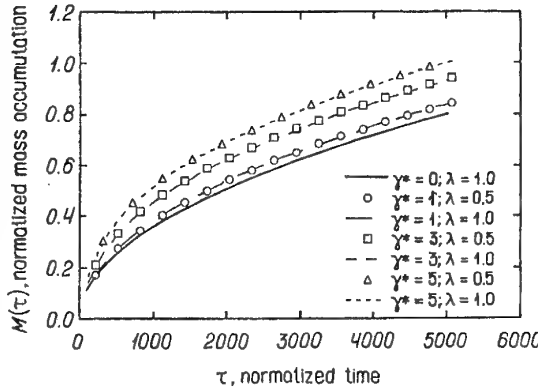


Fig. 4. Normalized mass accumulation for several values of  $\gamma^*$  and  $\lambda$ .

is plotted the mass accumulation for several combinations of  $\gamma^* = 0, 1, 3$  and  $5$  and  $\lambda = 0.5$  and  $1$ . There are several salient features to note. First, as expected, the amount of mass diffusion is increases with increasing elastic interaction, i.e., larger  $\gamma^*$ . Second there is very little discernable difference between  $\lambda = 0.5$  and  $\lambda = 1$  indicating that the short-range field effects are limited at these widths. Third, there is an enhanced diffusion over the base line case of  $\gamma^* = 0$  of the order of 20% at the later times. Given the little effect of  $\lambda$  on the mass diffusion, the baseline results for  $\gamma^* = 0.5$  or  $1$  should be about the same. For that reason, we have shown only  $\lambda = 1$  for  $\gamma^* = 0$ .

The width effect, e.g., the spacing between the dislocation walls has a marginal effect as the spacing,  $\lambda$ , becomes smaller. In Fig. 5,  $\lambda$  is varied from  $0.1, 0.5$  and  $1$  for two values of  $\gamma = 1$  and  $5$ . There is a slight increase in mass accumulation as the width is decreased to a value of  $0.1$  (recall this means that the spacing of the dislocation in each wall or array is 10 time larger than the separation distance between the walls). This analysis should be treated only as an indication of effect of the elastic interaction because this analysis uses the assumption of non-interacting dislocations.

#### 4. DISCUSSION

We discuss the evolution of amorphous grain boundaries in (i) sintered ceramics and (ii) solids under irradiation and thermal treatment based on the role of enhanced diffusion. To do so, we assume that the species diffusing from a pre-existent amorphous grain boundary into adjacent crystalline regions are capable of inducing the amorphization of these regions. This corresponds to experimentally observed situations (i) [1-5] and (ii) [6,7] where diffusion mixing causes growth of the amorphous phase at grain boundaries. With the above taken into account, the following scenario of the evolution is suggested which takes into

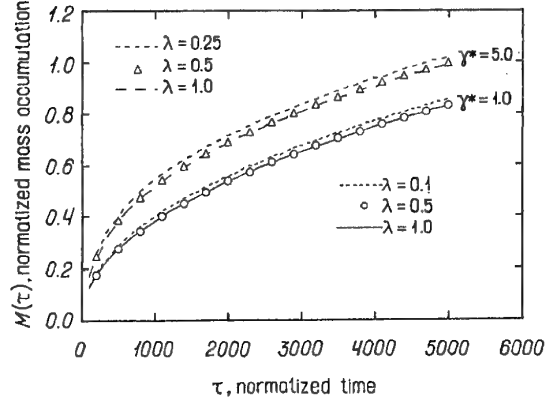


Fig. 5. Effect of width of dislocation wall spacing on mass accumulation.

consideration the role of enhanced diffusion in amorphizing transformations at grain boundaries. Penetration of the "amorphizing" diffusing species from an amorphous grain boundary to adjacent crystalline regions occurs in a spatially inhomogeneous way (see previous sections and Fig. 6a) and leads to change of  $\epsilon_{a-c}$  in the regions with a high density of the amorphizing diffusing species. This induces amorphization (crystal-to-glass transition) in these regions (Fig. 6b). The spatially inhomogeneous growth of the amorphous phase (Fig. 6b) forces crystalline-amorphous interface to be curved and, therefore, results in an increase of its contribution to the total energy density of the amorphous boundary. The crystalline-amorphous interface can straighten out and, as a corollary, decrease the total energy density in the following two-step way. First, grain boundary dislocations, due to absence of structure-imposed limitations on their spatial positions, move to new positions (Fig. 6c). The dislocations located in new positions create a new stress

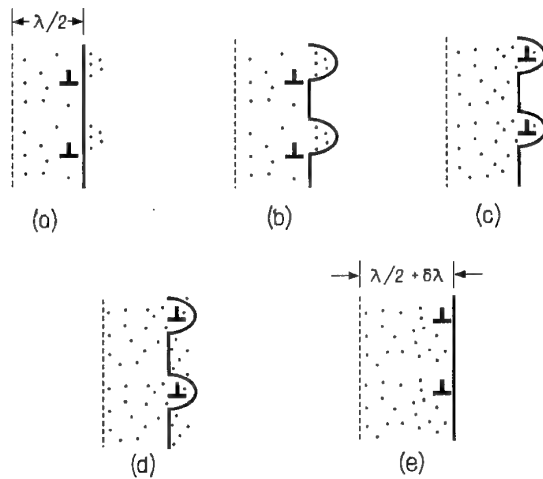


Fig. 6. Increased width of layer,  $\delta\lambda$ , by amorphization due to enhanced diffusion.

field distribution which, in its turn, enhances penetration of the amorphizing diffusing species from the amorphous grain boundary to new crystalline regions located between the "bugles" of the boundary (Fig. 6d). The diffusion is followed by amorphization of these new regions, in which case the crystal/glass interface becomes planar (Fig. 6e).

If there is a permanent "supply" of the amorphizing diffusing species to the amorphous grain boundary due to grain boundary diffusion (which quickly transfers the amorphizing diffusing species from some remote permanent source, e.g. a second phase region consisting of chemical elements that serve as the amorphizing diffusing species) or irradiation (see situation (ii)), then the boundary plays the role as a permanent source of the amorphizing diffusing species that penetrate into the adjacent crystalline grains. In these circumstances, the process shown in Fig. 6 is permanently repeated resulting in diffusion- or irradiation-induced permanent growth of the amorphous grain boundary. This corresponds to experimentally observed [6,7] situation (ii) where the diffusion- and irradiation-induced growth of the amorphous phase starts occurring at grain boundaries, which then gradually extend to amorphous regions of macro-scale extent.

If the quantity of the amorphizing diffusing species is limited, as in situation (i) with sintered ceramics, the process shown in Fig. 6 results in formation of an amorphous boundary of finite width. The boundary width is determined only by the sum (finite) quantity of the amorphizing diffusing in a sample. Since grain boundary diffusion is faster by several orders than bulk diffusion (that controls the growth of amorphous grain boundaries; see Fig. 6), basically, the same quantities of the amorphizing diffusing species are distributed along all the grain boundaries within a sample. This explains the experimentally observed (see [1,8] and references therein) specific feature of amorphous grain boundaries in sintered ceramics, which is a finite boundary width whose value is tentatively the same for all amorphous grain boundaries within a ceramic sample and depends on only the chemical composition.

The diffusion processes enhanced due to the elastic interaction of the diffusing species and amorphous grain boundaries represent an example of diffusion processes dependent on stress field distributions in polycrystalline and nanocrystalline solids. The contribution of such processes to the macroscopic diffusional properties is significant in solids with evolving defect structures and, therefore, evolving stress field distributions. In particular, the enhanced diffusion which accompanies transformations of amorphous grain boundaries (Fig. 6) is capable of essentially contributing to the anomalously fast diffusion in nanocrystalline solids where evolving

(amorphous and conventional) grain boundaries are inherent structural elements.

#### 4. CONCLUSIONS

As an initial attempt to understand the role of grain boundaries and their effect in nanosized materials, we have modeled a simple case of two non-interacting grain boundary arrays or walls separating an amorphous layer that provides a source for the diffusing species. A simple elastic interaction is considered and inserted into the diffusion equation that is solved for the time dependent behavior of the concentration. The mass accumulation is enhanced due to the elastic interaction and that until the spacing becomes small, the second dislocation array or wall has a minimal effect. And lastly, the static information derived from the interaction energy and its gradient, e.g. force on the diffusing species, will only yield qualitative information and that time dependent analysis is required. The enhanced diffusion essentially influences the growth of amorphous grain boundaries in solids under irradiation and thermal treatment as well in sintered ceramics and is capable of contributing to the anomalously fast diffusion in nanocrystalline materials.

#### ACKNOWLEDGEMENTS

We wish to thank the Office of Naval Research Headquarters (ONR) and Office of Naval Research International Research Field – Europe (ONR-Europe) for their generous support. One of us, (I.A.O.) was the recipient of ONR grant N00014-99-1-0569 and of ONR-Europe grant N00014-99-1-4016. The other author, (R.A.M.), was supported by ONR grant N0001499AF00002.

#### REFERENCES

- [1] Y.Kinemuchi, T.Yanai and K.Ishizaki // *Nanostr. Mater.* **9** (1997) 23.
- [2] X.Pan // *J. Am. Ceram. Soc.* **79** (1997) 2975.
- [3] H.Gu, X.Pan, I.Tanaka, R.M.Cannon, M.J.Hoffmann, H. Mullejans and M.Ruhle // *Mater. Sci. Forum* **207-209** (1996) 729.
- [4] X.Pan, M.Ruhle and K.Nihara // *Mater. Sci. Forum* **207-209** (1996) 761.
- [5] H.-J.Kleebe, G.Pezzotti and T.Nishida // *J. Mater. Sci. Lett.* **16** (1997) 453.
- [6] M.A.Hollanders, B.J.Thijssse and E.J.Mittenmeijer // *Phys. Rev. B* **42** (1990) 5481.
- [7] W.L.Gong, L.M.Wang and R.C.Ewing // *J. Appl. Phys.* **81** (1997) 2570.
- [8] D.R.Clarke // *J. Am. Ceram. Soc.* **70** (1987) 15.

[9] A.L.Kolesnikova, I.A.Ovid'ko and A.B.Reizis // *J. Mater. Proc. Manuf. Sci.* **7** (1999) 5.

[10] I.A.Ovid'ko and A.B.Reizis // *J. Phys. D: Appl. Phys.* **32** (1999) 2833.

[11] J.Horvath // *Defects and Diffusion Forum* **66-69** (1989) 207.

[12] H.-J.Hofler, H.Hahn and R.S.Averbach // *Defects and Diffusion Forum* **75** (1991) 195.

[13] L.A. Girifalco and D.O. Welch, *Point Defects and Diffusion in Strained Metals* (Gordon and Breach, 1967).

[14] A.P.Sutton and V.Vitek // *Phil. Trans. Roy. Soc. London A* **301** (1983) 1.

[15] A.P.Sutton and R.W.Balluffi, *Interfaces in Crystalline Materials* (Clarendon Press, Oxford, 1995).

[16] G.-J.Wang and V.Vitek // *Acta Metall.* **34** (1986) 951.

[17] K.N.Mikaelyan, I.A.Ovid'ko and A.E.Romanov // *Mater. Sci. Eng. A* **259** (1999) 132.

[18] F.R.N. Nabarro, *Theory of Crystal Dislocations* (Clarendon Press, Oxford, 1967).

# CORRELATION BETWEEN SUPERCONDUCTING TRANSPORT PROPERTIES AND GRAIN BOUNDARY MICROSTRUCTURE IN HIGH- $T_c$ SUPERCONDUCTING CERAMICS

T.S. Orlova<sup>1</sup>, J.Y. Laval<sup>2</sup> and B.I. Smirnov<sup>1</sup>

<sup>1</sup>A.F. Ioffe Physico-Technical Institute, Russian Academy of Sciences, Polytechnicheskaya 26, 194021

St.Petersburg, Russia,

<sup>2</sup>Laboratoire de Physique du Solide, CNRS ESPCI, 10 rue Vauquelin, 75231 Paris Cedex 05, France

Received: October 21, 1999

**Abstract.** The superconducting transport properties ( $I-V$ ,  $I_c-B$  and  $I_c-T$ ) were correlated with a systematic characterization of the grain boundary microstructure, via TEM observation and local chemical analysis in STEM by EDX on  $\text{YBa}_2\text{Cu}_{3-x}\text{O}_y$  (D samples),  $\text{YBa}_2\text{Cu}_{3-x}\text{O}_y/\text{Ag}_x$  (S samples) and  $\text{DyBa}_2\text{Cu}_{3-x}\text{O}_y/1\text{wt\% Pt}$  ( $0 \leq x \leq 0.4$ ) ceramics. It was shown that in all samples studied the critical current  $I_c$  is controlled by weak links at grain boundaries. The measurements of  $I_c(T)$  indicated that in copper-deficient yttrium ceramics, Ag-doping leads to change of weak link character from superconductor-insulator-superconductor (SIS) to superconductor-normal metal-superconductor (SNS) type. This SNS behaviour seems to be a result of percolation path of supercurrent through clean boundaries with extremely narrow range ( $\approx 1 \text{ nm}$ ) of Ag segregation on them. Specific Ag precipitates of 2-5 nm size on or near clean boundaries were found in S samples for  $x=0.4$ . This is most likely to be a reason for the improvement of  $I_c$  in these samples by a factor of 3. In copper-deficient dysprosium ceramics doped with Pt, Pt-doping leads to a substantial increase in  $I_c$  and pronounced 'fish-tail' effect in magnetic field at  $T \leq 77 \text{ K}$  in non-stoichiometric composition with  $x=0.2$ . Better behaviour of  $I_c$  in magnetic fields in these samples may be associated with the substantial increase in the proportion of clean boundaries and decrease in twin spacing.

## 1. INTRODUCTION

In the high- $T_c$  granular superconductors, transport properties are mainly controlled by the grain boundary microstructure unlike  $T_c$  which is determined by the crystal structure and oxygen content. Depending on crystallography and structure of boundaries, they can be favourable for the passage of supercurrent or can be weak links (reduced  $I_c$  regions) in the superconducting current path of a ceramic sample. Recently many studies have been directed at investigating the dissipation at a separate boundary of different type [1]. Although studies of separate boundary behaviour highly contribute to understanding transport in superconducting polycrystalline materials, they are rather idealistic models of true polycrystalline materials which contain many boundaries of different types, in parallel and series, simultaneously. So, along with the study of a separate boundary, it is also very important to investigate the relation between transport properties and grain boundary behaviour as a network of boundaries.

The main aim of this work was to find possible correlation between microstructure features and superconducting transport properties. One way for changing intergrain critical current density of polycrystalline materials is doping with different elements. Small deviation from the stoichiometric composition can also lead to a change in structure and distribution of boundaries in a ceramic sample.

So, in this work the superconducting transport properties ( $I-V$ ,  $I_c-B$  and  $I_c-T$ ) were correlated with a systematic characterization of the grain boundary microstructure, via TEM observation and local chemical analysis in STEM by EDX. The following superconducting ceramics were studied.

1.  $\text{YBa}_2\text{Cu}_{3-x}\text{O}_y$  ( $0 \leq x \leq 0.4$ ) – Cu-deficient yttrium ceramics (D samples);  $\text{YBa}_2\text{Cu}_{3-x}\text{O}_y/\text{Ag}_x$  ( $0 \leq x \leq 0.4$ ) ceramics with silver incorporated in amounts equal to the copper deficiency (S samples).
2.  $\text{DyBa}_2\text{Cu}_{3-x}\text{O}_y/1\text{wt\% Pt}$  ( $0 \leq x \leq 0.4$ ) – Cu-deficient dysprosium ceramics doped with 1 wt% Pt.

## 2. EXPERIMENTAL

The YBCO ceramic system was fabricated via the modified citrate gel process [2]. The sol-gel method allows one to achieve highly homogeneous mixing of cations on an atomic scale and produce high-quality powder. Two types of YBCO samples were prepared. In samples of the first type  $\text{YBa}_2\text{Cu}_{3-x}\text{O}_y$  ( $0 \leq x \leq 0.4$ ) (D type) Cu-deficient compositions were obtained. In samples of the second type,  $\text{YBa}_2\text{Cu}_{3-x}\text{O}_y/\text{Ag}_x$  ( $0 \leq x \leq 0.4$ ) (substituted S type), Ag was considered as a substituent for Cu.

The copper deficient ceramics,  $\text{DyBa}_2\text{Cu}_{3-x}\text{O}_y$ , doped by 1wt.% Pt, were prepared by the usual solid state reaction. For comparison two compositions with  $x=0$  and  $x=0.2$  of the copper deficient ceramics  $\text{DyBa}_2\text{Cu}_{3-x}\text{O}_y$  without Pt were also fabricated using the same method.

The phase were characterised by powder X-ray diffraction (XRD) using a Philips automated X-ray diffractometer. Microstructure and chemical compositions were analysed with a Jeol 2000 FX TEM equipped with a Link EXL X-ray selective analyser and with an SEM equipped with an EDAX X-ray selective analyser.

The superconducting properties were studied by measuring the resistivity-temperature ( $R-T$ ) and current-voltage ( $I-V$ ) characteristics using the four-probe technique. The critical current  $I_c$  was determined at various temperatures using the  $1 \mu\text{V}\cdot\text{mm}^{-1}$  criterion, with and without external magnetic field B. The external magnetic field ranged from 0 to 75 G and was perpendicular to the transport current.

## 3. RESULTS AND DISCUSSION

### 3.1 COPPER DEFICIENT YTTRIUM SYSTEM WITH AND WITHOUT AG-DOPING

First we will consider 123-yttrium system with copper deficiency with and without Ag-doping. According to the data in the literature [3-5] distribution of Ag in ceramics and its influence on  $J_c$  are subject to contradictory conclusions and strongly depend on composition of ceramics, processing technology and thermal treatment. Our ceramic samples were prepared via the modified citrate gel process [2] which allows one to achieve highly homogeneous mixing of cations on an atomic scale and produce high-quality homogeneous ceramics.

EDX analysis in TEM showed (Table 1) that the Ag content ( $x$ ) of YBCO grains was lower than the nominal amount of Ag, in spite of the sol-gel method. Ag mainly precipitated as small particles ( $1-2 \mu\text{m}$ ) homogeneously scattered throughout the sample.

**Table 1.** Average concentration of silver in the grains measured by EDX in TEM and STEM for  $\text{YBa}_2\text{Cu}_{3-x}\text{O}_y/\text{Ag}_x$  for all doping levels.

Nominal Ag concentration $x$	Real Ag concentration
0.1	< limit of detection
0.2	$\leq 0.02$
0.4	0.03

X-ray diffraction and SEM analysis showed that all samples had an good orthorhombic structure. For samples with  $x \geq 0.2$ , along with Ag phase (S samples) several nonsuperconducting phases such as  $\text{Y}_2\text{BaCuO}_5$  (211),  $\text{BaCuO}_2$  (011) and  $\text{CuO}$  (D and S samples) were registered. The amount of these nonsuperconducting phases (in D and S samples) and Ag-phase (S samples) increased with increasing  $x$ . Second phases such as  $\text{BaCuO}_2$  and  $\text{CuO}$  were mainly located at grain boundaries and triple junctions. These impurity phases were about  $1-3 \mu\text{m}$  in size, the mean distance between them was comparable with respective grain size. The average grain size dramatically decreased with  $x$  (Fig. 1). The nonsuperconducting phases and Ag precipitates appear to stop grain growth during sintering resulting in fine-grain microstructure for  $x \geq 0.2$ .

For all samples of both type (D and S) the critical temperature was practically the same ( $T_c = 91-92 \text{ K}$ ), but the transport properties were quite different. Fig. 2 shows the measured values of critical current density  $J_c$  at 77 K versus  $x$ . For S samples,  $J_c$  increased only slightly with increase in Ag content from  $x=0$  to  $x=0.2$ , whereas  $J_c$  increased more than threefold (from  $J_c = 50 \text{ A/cm}^2$  for  $x=0$  to  $J_c = 170 \text{ A/cm}^2$ ) for  $x=0.4$ . For D samples with  $x \geq 0.2$ ,  $J_c$  is  $\cong$  twice that obtained for the stoichiometric composition.

It should be specially noted that in samples of both type (D and S), the obtained  $I-V$  curves at 77 K exhibited a power-low behaviour.  $I_c$  was strongly depressed

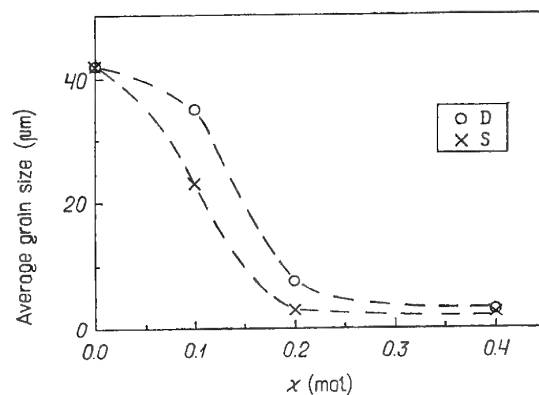


**Fig. 1.** Dependence of the average grain size of  $\text{YBa}_2\text{Cu}_{3-x}\text{O}_y$  (D) and  $\text{YBa}_2\text{Cu}_{3-x}\text{O}_y/\text{Ag}_x$  (S) samples on  $x$ .

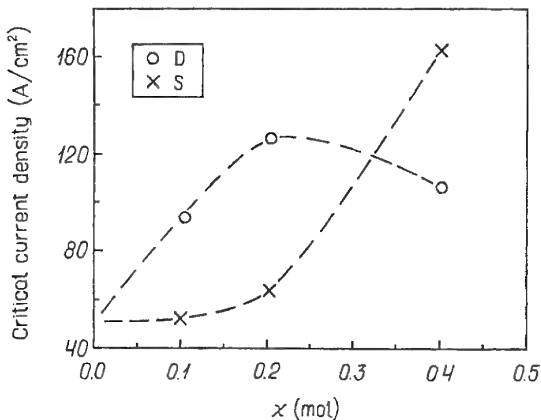


Fig. 2. Variation of the critical current with  $x$  for D and S samples.

by low magnetic fields. Such behaviour is characteristic of granular materials which can be described as a collection of superconducting grains connected by weak links [6].

Thus, in all samples  $I_c$  was controlled by grain boundary weak links which were characterized from  $I_c(T)$  curves. It is known that for a Josephson tunnel (SIS) junction the dependence of  $I_c$  on temperature agrees with the equation  $I_c = \text{const} (1-T/T_c^*)$  for temperature close to the superconducting transition temperature  $T_c^*$  of the intergrain junction [7]. For the SNS-type proximity junctions, close to  $T_c^*$  the  $I_c(T)$  dependence can be written in the form  $I_c = \text{const} (1-T/T_c^*)^2$  [8]. To identify the character of weak links we tried to find the dependence of  $I_c$  on temperature for  $T$  close to the critical temperature  $T_c$  of a sample. The obtained dependence of  $I_c$  on  $(1-T/T_c)$  were plotted on a logarithmic scale in order to determine the value of  $\beta$  in the equation  $I_c = \text{const} (1-T/T_c)^{\beta}$  (Fig. 3). As can be seen, for D samples  $I_c(T)$  corresponds to an SIS junction

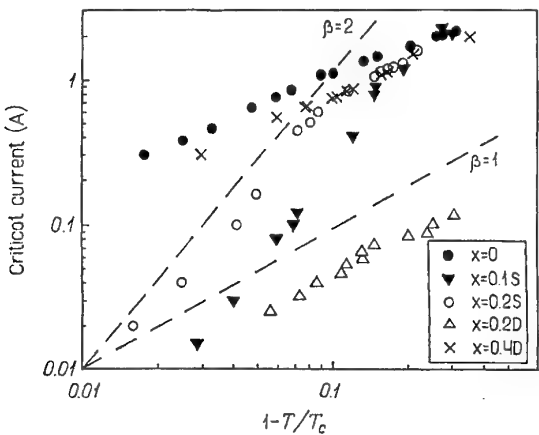


Fig. 3. Critical current versus  $(1-T/T_c)$  plotted for D and S samples in a logarithmic scale to determine the value of  $\beta$  in the equation  $I_c = \text{const} (1-T/T_c)^{\beta}$ .  $\beta=1$  and  $\beta=2$  cases are shown by the dashed lines.

tion ( $\beta \approx 1$ ). On the other hand, for S samples  $I_c(T)$  agrees with an SNS type junction ( $\beta \approx 2$ ) for any  $x$  value.

In this work a systematic statistical study of grain boundaries was made to correlate their distribution to the observed change in  $J_c$  when  $x$  varied from 0 to 0.4. So, 40–50 consecutive boundaries in each sample were characterized by bright field tilting imaging in TEM. The grain boundaries were distributed into 3 types. 'Clean' boundaries correspond to boundaries in which no intergranular phase was detected in TEM bright field. In contrast, 'dirty' boundaries exhibit an intergranular phase (thickness  $> 2$  nm). At last, 'thin-film-coated' boundaries display a thin phase with a thickness  $\leq 2$  nm. For clean boundaries, we paid attention on peculiarities such as dislocations, small facets or fine precipitates on them. One should take into account the fact that clean boundaries are favourable for transmitting the supercurrent only when the orientation crystallographic relationships between adjacent grains are suitable. Usually, no more than 50% of clean boundaries are considered as favourable. According to the data in [9], the percolation threshold is about 12%.

The histogram in Fig. 4 shows the statistical study results. In the D samples, the ratio of clean boundaries was found to remain between 27 and 45%. The proportion of clean boundaries decreased with  $x$ . The observed increase in  $J_c$  with  $x$  in D samples can be explained by the increase in the proportion of the faceted clean boundaries, which can act as pinning centres (Fig. 4). Ag doping resulted in a higher proportion of clean boundaries for  $x \geq 0.2$ , but there were only few faceted boundaries among them. For the composition with  $x=0.4$ , which exhibited 3 times increase in  $J_c$ , a peculiarity in the structure of clean boundaries was found, namely, about half of the clean boundaries contained

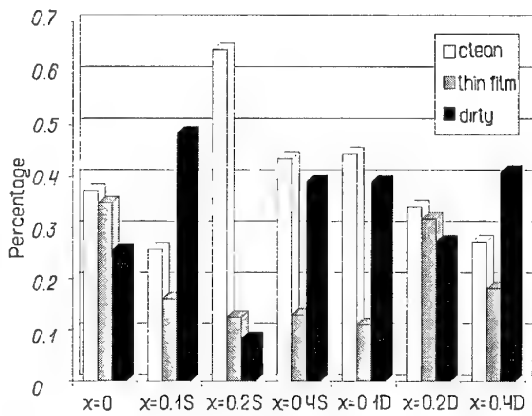


Fig. 4. Histogram showing the distribution of clean, thin-film-coated and dirty grain boundaries for a sample of the stoichiometric composition ( $x=0$ ), D and S samples. The dashed lines show the fraction of faceted clean boundaries among all clean boundaries.

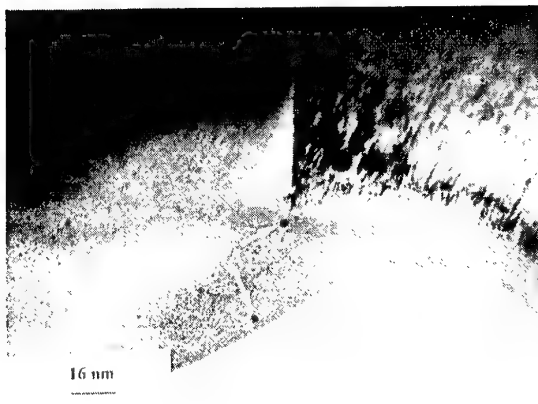


Fig. 5. Micrograph of a 'clean' boundary with Ag precipitates (shown by arrows) in TEM for an S sample ( $x=0.4$ ).

small precipitates of 2–5 nm in size on the boundary itself, or close to it (up to 5 nm). The average distance between these precipitates was about 30 nm. An example of such a 'clean' boundary with Ag precipitates is presented in Fig. 5. These small Ag precipitates can act as very efficient pinning centres resulting most likely in the 3-fold increase in  $J_c$  in this composition.

To detect possible Ag segregation at clean grain boundaries, EDX analysis in STEM with 1 nm probe was used. The detected concentration of Ag on some clean boundaries was twice higher than the obtained solubility limit of Ag in the grains ( $x=0.03$ ). This increased Ag segregation on grain boundaries most probably leads to SNS behaviour of weak links in S samples as result of a percolation path of supercurrent through such 'clean' boundaries with an extremely narrow Ag segregation ( $\approx 1$  nm) on them.

### 3.2 Cu-DEFICIENT DYSPROSIUM CERAMICS DOPED WITH 1 wt.% Pt

The next system studied was Cu-deficient dysprosium ceramics doped by Pt. Such a ceramic system was chosen due to the following reason. As we saw above, the deviation from stoichiometry leads to the formation of secondary phases in sintered ceramics. According to the literature data [10, 11], in melt-textured ceramics the addition of Pt can result in decrease in size of 211 secondary phase inclusions, improving thereby their pinning possibility and, then the critical current. In our work, for Cu-deficient dysprosium sintered ceramics doped with Pt, we tried again to identify microstructural elements, which can be responsible for the differences in superconducting properties.

In all compositions, Pt-doping resulted in the nucleation of intragranular secondary phases of submicron

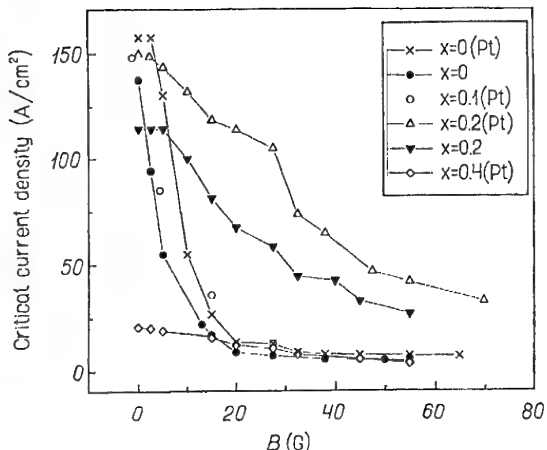


Fig. 6. Critical current density at 77 K versus applied magnetic field for  $\text{DyBa}_2\text{Cu}_{3-x}\text{O}_y/1\text{wt.\%Pt}$  and  $\text{DyBa}_2\text{Cu}_{3-x}\text{O}_y$  samples.

size, which contain Pt and were homogeneously distributed into 123 grains. In addition, in the non-stoichiometric composition, Pt was also located in intergranular  $\text{BaCuO}_2$  secondary phases. Unlike the melt-textured 123 ceramics [10, 11], no influence of Pt on size and distribution of 211 secondary phase was found. Traces of Pt in the 123 grains were detected in all compositions doped by Pt. Distribution of Pt in the matrix was inhomogeneous. The maximum content of Pt in a grain was 0.06 molar content.

Fig. 6 displays the dependence of critical current density  $J_c$  on applied magnetic field. As seen, at zero-magnetic field doping with platinum practically does not change  $J_c$  in stoichiometric composition, but leads to its substantial increase for non-stoichiometric composition with  $x=0.2$ . The stoichiometric compositions exhibit a sharp drop of  $J_c$  values even in very low magnetic field. Non-stoichiometric compositions show a much smoother decrease in  $J_c$  with magnetic field. Doping with Pt strongly contributed to the so-called 'fish-tail' effect which means stabilization of  $J_c$  in magnetic field. For this composition this 'fish-tail' behaviour became more pronounced when the temperature was decreased (Fig. 7). So, the copper-deficient samples, especially the one doped with Pt seem to have better possibilities for pinning magnetic vortices in applied magnetic fields.

Similar to the system with Ag, for these ceramics with Pt we also tried to identify the character of the intergranular junction network from  $J_c$  versus temperature dependence (Fig. 8). Grain boundary network was found to behave predominantly as SIS junctions, even in Pt-doped samples so that Pt seems not to segregate in sufficient amount, at least, at grain boundaries. Within the accuracy of our EDX analysis we did not reveal higher concentration of Pt in boundaries compared with grains.

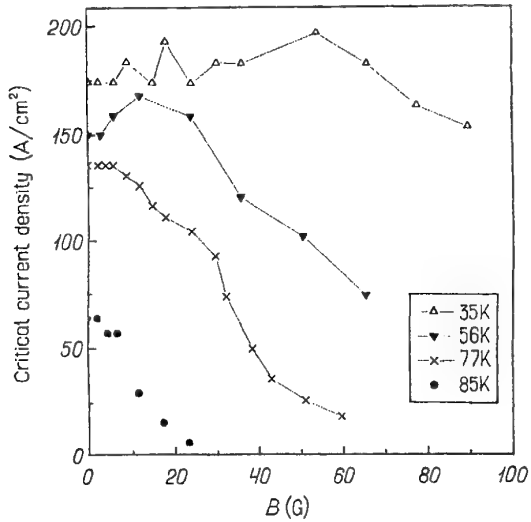


Fig. 7. Critical current density at 77 K versus applied magnetic field for  $\text{DyBa}_2\text{Cu}_{2.8}\text{O}_y$ /1wt.%Pt at different temperatures.

The above superconducting properties were correlated with the microstructural features of the studied samples. In all compositions the 123 matrix exhibits well crystallized and well twinned grains, but with different twin density. It is known that twin boundaries in the 123 materials may act as flux pinning centres [12, 13]. In granular ceramics, where critical current is limited by weak links at grain boundaries, it is reasonable to consider twins near the boundaries. The higher the twin density the more efficient the pinning of vortices along the boundary. We compared the twin density in our compositions. As seen in the Table 2, in non-stoichiometric composition, the average spacing  $d$  between twins is twice smaller than in the stoichiometric one. In addition, in non-stoichiometric composition doped with Pt we locally observed very fine twins with  $d=20$  nm, whereas in such composition only without Pt such a high density of twins was not found, at all. The presence of these highly dense twins can be caused by partial substitution of Cu by Pt in grains. A decrease of twin spacing due to Pt doping was observed in melt-textured 123 ceramics in [13, 14]. The higher density of twin boundaries in the vicinity of grain boundaries can improve the pinning properties under magnetic field. The highest local density of twins was observed in the composition, which exhibited the best 'fish-tail' effect in magnetic field.

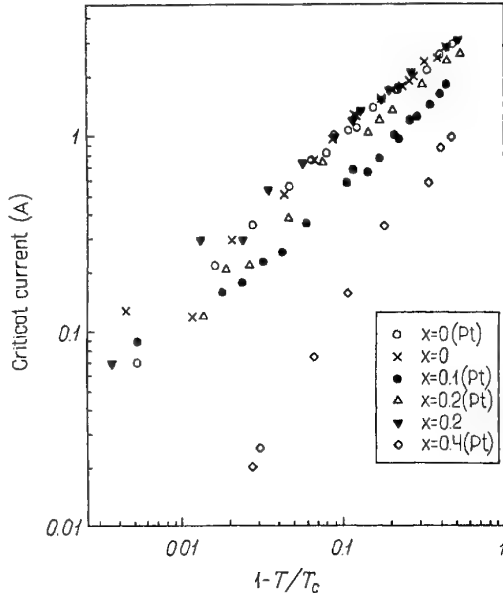


Fig. 8. Critical current versus  $1-T/T_c$  plotted on logarithmic scale to determine the value  $\beta$  in the equation  $I_c = \text{const} (1-T/T_c)^\beta$  for  $\text{DyBa}_2\text{Cu}_{3-x}\text{O}_y$ /1wt.%Pt and  $\text{DyBa}_2\text{Cu}_{3-x}\text{O}_y$  samples.

We also performed comparative statistical study of grain boundaries, Table 3. It was found that in non-stoichiometric composition, unlike the stoichiometric one, grain boundaries are mostly clean or thin-film-coated. Doping with Pt resulted in a higher proportion of clean boundaries. Such statistical results can explain the sharp drop of  $I_c$  under very low magnetic fields ( $\leq 10$  G) in  $\text{DyBa}_2\text{Cu}_3\text{O}_y$ /1wt.%Pt samples. As already noted above, no more than a half of clean boundaries can be considered as favourable [9]. So the supercurrent is likely to pass through a few thin-film-coated GBs resulting in the sharp drop in  $I_c$  in low magnetic fields. The non-stoichiometric compositions with  $x=0.2$  have enough clean boundaries to provide the percolation path for supercurrent. A possibility for redistribution of the supercurrent through clean boundaries in a magnetic field and high dense twins locally observed can be reasons for better  $I_c$  behaviour in a magnetic field in non-stoichiometric composition doped with Pt.

## CONCLUSION

- In all considered ceramic systems the critical current  $I_c$  is controlled by weak links at grain boundaries.

Table 2. The spacing between twins in  $\text{DyBaCuO(Pt)}$  samples.

	$\text{DyBa}_2\text{Cu}_3\text{O}_y$ /1wt.%Pt	$\text{DyBa}_2\text{Cu}_{2.8}\text{O}_y$ /1wt.%Pt	$\text{DyBa}_2\text{Cu}_{2.8}\text{O}_y$
Average twin spacing $d$	110 nm	50 nm (fine twins with $d \approx 20$ nm locally observed)	60 nm

**Table 3.** The distribution of clean, thin-film-coated and dirty grain boundaries in  $DyBa_2Cu_{3-x}O_y/1\text{wt\% Pt}$  samples.

	$DyBa_2Cu_3O_y/1\text{wt\% Pt}$	$DyBa_2Cu_{2.8}O_y/1\text{wt\% Pt}$	$DyBa_2Cu_{2.8}O_y$
Clean	24 %	58 %	44 %
Thin-film	16 %	29 %	37 %
Dirty	56 %	5 %	15 %
Non-characterized	4 %	8 %	4 %

(ii) In Cu-deficient yttrium ceramics doped with Ag in amount equal the deficiency, Ag doping leads to change of type of the weak links from SIS to SNS-type. Such SNS behaviour is a result of percolation path of supercurrent through clean boundaries with extremely narrow (1nm) Ag-segregation on them. For  $x=0.4$ , decoration of clean boundaries by very fine Ag-precipitates (2–5 nm) is the most likely reason for 3 fold increase of critical current.

(iii) In non-stoichiometric composition with  $x=0.2$ , Pt-doping leads to pronounced increase in  $I_c$  and fish-tail effect in magnetic field. This may be associated with the substantial increase in proportion of clean boundaries and highly dense twins locally observed (due to Pt segregation in 123 grains). No noticeable segregation of Pt in grain boundaries was revealed.

## REFERENCES

- [1] S.E. Babcock and J.L. Vargas // *Annu. Rev. Mater. Sci.* **25** (1995) 193.
- [2] R.S. Liu, W.N. Wang, C.T. Chang and P.T. Wu // *Japan. J. Appl. Phys.* **28** (1989) L2155.
- [3] D.F. Lee, X. Chaud and K. Salama // *Physica C* **181** (1991) 81.
- [4] J. Joo, J.P. Singh, R.B. Poepel, A. K. Gangopadhyay and T.O. Mason // *J. Appl. Phys.* **71** (1992) 2351.
- [5] C. Nguyen-van-Huong, E. Crampin, J.Y. Laval and A. Dubon // *Supercond. Sci. Technol.* **10** (1997) 85.
- [6] R.L. Peterson and J.W. Ekin // *Physica C* **157** (1989) 325.
- [7] J. Jung, I. Isaac and A.-K. Mohamed // *Phys. Rev. B* **48** (1993) 7526.
- [8] P.G. DeGennes // *Rev. Mod. Phys.* **36** (1964) 225.
- [9] V.K.S. Shante and S. Kirkpatrick // *Adv. Phys.* **20** (1971) 325.
- [10] M. Murakami, S. Gotoh, N. Koshizuka, S. Tanaka, T. Matsushita, S. Kanube and K. Kitazama // *Cryogenics* **30** (1990) 390.
- [11] M. Murakami, H. Fujimoto, S. Gotoh, K. Yamagushi, N. Koshizuka and S. Tanaka // *Physica C* **185-189** (1991) 321.
- [12] A.H. King and Y. Zhu // *Phil. Mag. A* **67** (1993) 1037.
- [13] I. Monot, K. Verbist, M. Hervieu, P. Laffez, M.P. Delamare, J. Wang, G. Desgardin and G.V. Tendeloo // *Physica C* **274** (1997) 253.
- [14] M.P. Delamare, M. Hervieu, J. Wang, J. Provost, I. Monot, K. Verbist and G.V. Tendeloo // *Physica C* **262** (1996) 220.

# MODELING OF SIZE EFFECT ON DIELECTRIC RESPONSE OF THIN FERROELECTRIC FILMS

O.G. Vendik and S.P. Zubko

Electronics Department, Electrotechnical University,  
Prof. Popova 5, St. Petersburg 197376, Russia  
Fax: +7 812 234-4809,

Received: September 30, 1999

**Abstract.** The size effect in thin film sandwich structures is considered. Three types of boundary conditions for dynamic polarization at interface electrode-ferroelectric layer are formulated. The type of boundary conditions depends on matching crystal lattices of electrodes and ferroelectric layer. A model describing the dependence of dielectric permittivity on biasing field, temperature, and thickness of the thin ferroelectric film is proposed. The results of the simulation are in good agreement with experiments.

The dielectric nonlinearity of ferroelectrics allows to use these materials as the basis of electrically tunable devices. Thin film ferroelectrics are used at microwaves. If the thickness of the film is comparable with the correlation radius the size effect appears in the film, i.e. the dielectric permittivity of film depends on its thickness. The size effect is related with the spatial distribution of polarization inside the ferroelectric film and type of the boundary conditions for polarization. The size effect results in a decrease in the polarization and therefore, in reduced dielectric permittivity and tunability. Through the selection of electrode material one can control the size effect on dielectric response of the thin ferroelectric films.

The dielectric permittivity of ferroelectric bulk material is a function of biasing field and temperature. The model of dependence of dielectric permittivity on biasing field and temperature is based on Ginsburg-Devonshire expansion of free energy density in the power series over the order parameter. For ferroelectrics the order parameter is a spontaneous polarization [1-4].

The phenomenological model of the dielectric permittivity of a bulk sample is presented by the following equation:

$$\begin{aligned} \epsilon^{-1} = \epsilon_{\infty}^{-1} \{ & [(\xi^2 + \eta^3)^{1/2} + \xi]^{2/3} + \\ & [(\xi^2 + \eta^3)^{1/2} - \xi]^{2/3} - \eta \} \end{aligned} \quad (1)$$

where

$$\xi(U_B) = \sqrt{\xi_s^2 + \xi_B^2}, \quad (2)$$

$$\eta(T) = \frac{\theta_F}{T_c} \sqrt{\frac{1}{16} + \left(\frac{T}{\theta_F}\right)^2} - 1, \quad (3)$$

$$\xi_B = \frac{U_B}{E_N h}, \quad E_N = \frac{2D_N}{\epsilon_0 (3\epsilon_{\infty})^{3/2}}, \quad (4)$$

$\epsilon_0$  is the permittivity of a free space,  $h$  is the thickness of ferroelectric film included in sandwich capacitor represented in Fig. 1,  $U_B$  is a biasing voltage.

Model parameters:  $\epsilon_{\infty}$  is the analogue to Curie-Weiss constant;  $T_c$  is the effective Curie temperature;  $\theta_F$  is the effective Debye temperature of the sublattice oscillations causing ferroelectric polarization;  $E_N$  is the

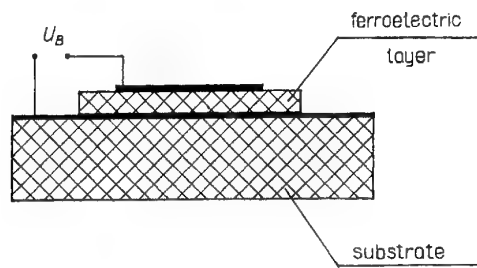


Fig. 1. Sandwich capacitor as a simplified general structure.

**Table 1.** Model parameters for single crystal  $\text{SrTiO}_3$ .

	$T_c$ (K)	$\epsilon_{\infty}$	$E_N$ (kV/cm)	$\theta_p$ (K)	$\xi_s$
single crystal $\text{SrTiO}_3$ [5]	42	2081	19.3	175	0.018

normalizing electric field;  $\xi_s$  is the statistical dispersion of the biasing field characterizing the quality of material. The numerical values of model parameters for bulk material [5] are presented in Table 1.

The dependence of dielectric permittivity of the film on its thickness should be included in the model. In order to take into account the size effect, it is necessary to solve a second-order differential equation with respect to polarization. This equation is a consequence of Ginsburg-Devonshire expansion [6]:

$$-2\lambda_1 \frac{d^2 P(x)}{dx^2} + \frac{D(x)}{\epsilon(T)} + \frac{D^3(x)}{D_N^2} = \epsilon_0 E(x), \quad (5)$$

$$\epsilon(T) = \frac{\epsilon_{\infty}}{\eta(T)} \quad (6)$$

where  $P(x)$ ,  $D(x)$ ,  $E(x)$  are polarization, displacement, and electric field;  $\lambda_1$  is a correlation parameter;  $x$  axis is directed normally to the electrode-ferroelectric film interface.

The numerical values of the correlation parameter determined from the experimental data on inelastic neutron scattering on soft mode of ferroelectric crystal are presented in Table 2 [7,8]. The film thickness above which the size effect appears is a correlation radius of ferroelectric polarization which can be extracted from the equation (5).

**Table 2.** Numerical values of correlation parameter.

$\lambda_1$	$\text{SrTiO}_3$	$\text{KTaO}_3$	$\text{BaTiO}_3^*$
$\mu\text{m}^2$	$1.15 \cdot 10^{-7}$	$5.37 \cdot 10^{-7}$	$10^{-9}$

\* Preliminary estimation

$$r_c(T) = \sqrt{2\lambda_1 \epsilon(T)}. \quad (7)$$

For different crystal structures of electrodes three different types of boundary conditions at electrode-ferroelectric interface can be realized. The spatial distribution of polarization corresponding to a certain type of boundary conditions induces the size effect in the film.

There are three types of boundary conditions for dynamic polarization [9]:

(I) Zero boundary conditions:

$$P_{ac}(x)|_{x=\pm h/2} = 0 \quad h_{eff} = h$$

(II) Intermediate boundary conditions:

$$\left( P_{ac}(x) \pm b \frac{dP_{ac}(x)}{dx} \right) \Big|_{x=\pm h/2} = 0 \quad h < h_{eff} < \infty$$

(III) Free boundary conditions:

$$\frac{dP_{ac}(x)}{dx} \Big|_{x=\pm h/2} = 0 \quad h_{eff} \rightarrow \infty.$$

The boundary conditions of the type (I) are referred to a sandwich capacitor with electrodes made of a normal metal. The polarization distribution provided by these boundary conditions causes the size effect. The boundary conditions of the type (II) are referred to a sandwich capacitor with  $\text{YBa}_2\text{Cu}_3\text{O}_{7-x}$  (YBCO) electrodes. In this case polarization can partially penetrate inside the electrodes. To allow the better understanding of that, the effective film thickness  $h_{eff}$  was introduced. Free boundary conditions (type III) are realized in structures with  $\text{SrRuO}_3$  (SRO) electrodes. The spatial distribution of polarization inside the ferroelectric layer for three types of boundary conditions is shown in Fig. 2.

Having solved equation (5) with zero boundary conditions, one can derive the expression for dynamic polarization taking into account the size effect:

$$P_{ac}(x) = P_{ac}(0) \left[ 1 - \frac{ch(\alpha x)}{ch(\alpha h/2)} \right],$$

$$P_{ac}(0) = \frac{Q_{ac}}{S} \left[ 1 - \frac{1}{\epsilon(T)} - 3 \left( \frac{Q_{dc}}{D_N S} \right)^2 \right]$$

where  $Q_{ac}$  and  $Q_{dc}$  are the alternating and direct current components of the charge at the electrodes respectively;  $S$  is the area of the electrodes.

The inverse effective dielectric permittivity of a thin ferroelectric film is:

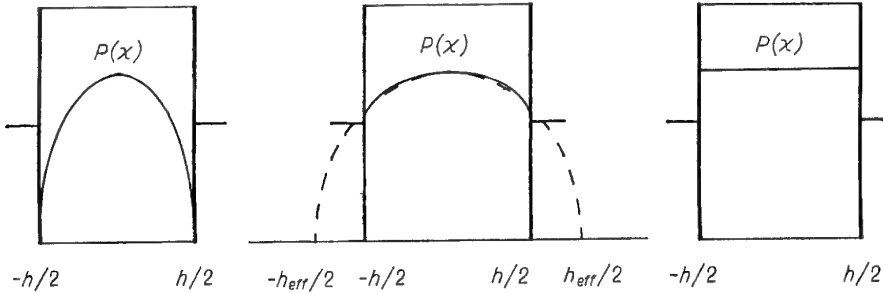


Fig. 2. Spatial distribution of dynamic polarization inside ferroelectric layer in the case: a — zero boundary conditions; b — intermediate boundary conditions; c — free boundary conditions.

$$\varepsilon^{-1} = \varepsilon_{\text{oo}}^{-1} \left\{ \left[ (\xi^2 + \eta^3)^{1/2} + \xi \right]^{2/3} + \left[ (\xi^2 + \eta^3)^{1/2} + \xi \right]^{2/3} - \eta + a^2 \right\} \quad (8)$$

where the parameter of size effect is  $a = \sqrt{2\varepsilon_{\text{oo}} / \alpha h_{\text{eff}}}$ ;  $\alpha = 1 / \sqrt{2\lambda_1}$ .

The numerical values of the model parameters obtained for various sandwich structures are presented in Table 3. Fig. 3 shows good agreement between experimental and model dependencies calculated using

model parameters from Table 3. Curves in Fig. 3 illustrate influence of size effect on dielectric permittivity. In the ferroelectric capacitors with YBCO electrodes dynamic polarization partially penetrates inside electrodes and influence of the size effect in this case is attenuated.

Experimental [13] and model dependencies of dielectric permittivity of thin film  $\text{Ba}_{0.12}\text{Sr}_{0.88}\text{TiO}_3$  (BSTO) included in sandwich capacitors with Pt and SRO electrodes are presented in Fig. 4. At room temperature

Table 3. Model parameters for thin ferroelectric films.

Capacitor	$h(\mu\text{m})$	$h_{\text{eff}}(\mu\text{m})$	$\varepsilon_{\text{oo}}$	$T_c(K)$	$\Theta_p(K)$	$E_N(\text{kV/cm})$	$\xi_s$	$a$	
YBCO/STO/Au [10]	0.250	0.230	4265	34	152	6.0	2.3	16	(I)
Pt/STO/Ni [11]	0.046	0.037	4143	40	152	8.7	1.5	7	(I)
YBCO/STO/YBCO [12]	0.800	2.300	3090	35	152	6.5	0.8	1.2	(II)
SRO/BSTO/SRO [13]	0.020	$\infty$	4400	42	175	12	1.0	0	(III)
SRO/BSTO/Pt [13]	0.020	0.37	4400	42	175	12	1.0	3	(II)

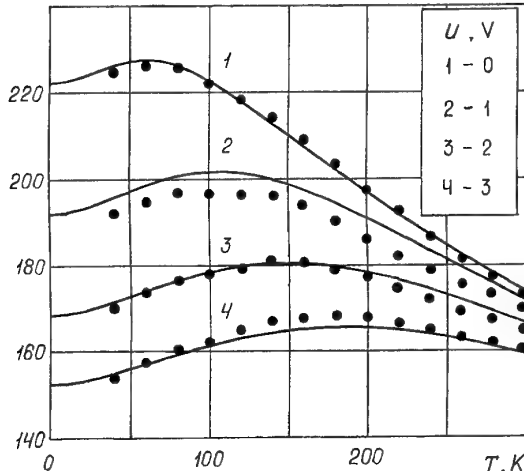


Fig. 3. Experimental (points) [10] and model dependencies (solid lines) of effective dielectric constant of  $\text{SrTiO}_3$  film on temperature and biasing field.

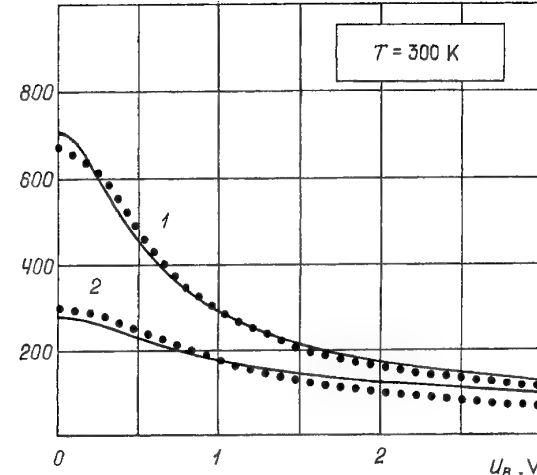


Fig. 4. Experimental (points) [13] and model dependencies (solid lines) of effective dielectric constant on biasing voltage: 1 —  $\text{SrRuO}_3/\text{Ba}_{0.12}\text{Sr}_{0.88}\text{TiO}_3/\text{SrRuO}_3$ ; 2 —  $\text{SrRuO}_3/\text{Ba}_{0.12}\text{Sr}_{0.88}\text{TiO}_3/\text{Pt}$ .

effective permittivity of the film in capacitor with SRO electrodes is higher than permittivity of single crystal in about 2.5 times. One can conclude that in the case of good matching of crystal lattices of electrodes and ferroelectric film the size effect is suppressed and free boundary conditions for dynamic polarization are realized. Tunability of such capacitor is more better than tunability of the capacitor with Pt electrode.

Thus interface between thin ferroelectric film and electrodes determines distribution of polarization inside ferroelectric layer and therefore variation of dielectric characteristics of sandwich capacitor. By chosen electrodes one can suppress size effect in thin film structures.

## REFERENCES

- [1] V.L. Ginsburg // *Zh. Eksp. Theor. Fiz.* **19** (1949) 36.
- [2] A.F. Devonshire // *Phil. Mag.* **40** (1949) 1040.
- [3] O.G. Vendik // *Fiz. Tverd. Tela* **14** (1972) 989.
- [4] O.G. Vendik and S.P. Zubko // *J. Appl. Phys.* **82** (1997) 4475.
- [5] K. Bethe // *Philips Research Report*, Supplement, No. 2 (1970) 1.
- [6] O.G. Vendik and L.T. Ter-Martirosyan // *Fiz. Tverd. Tela* **36** (1994) 3343.
- [7] O.G. Vendik and I.G. Mironenko // *Fiz. Tverd. Tela* **16** (1974) 3445.
- [8] S.P. Zubko // *Tech. Phys. Lett.* **24** (1998) 839.
- [9] O.G. Vendik, S.P. Zubko and L.T. Ter-Martirosyan // *Appl. Phys. Lett.* **73** (1998) 37.
- [10] F.A. Miranda, C.H. Mueller, G.A. Koepf and R.M. Yandrofski // *Supercond. Sci. Technol.* **8** (1995) 755.
- [11] S. Komatsu and K. Abe // *Jpn. J. Appl. Phys.* **23** Pt. 1 (1995) 3597.
- [12] A.T. Findikoglu, C. Doughty and S.M. Anlage // *Appl. Phys. Lett.* **63** (1993) 3215.
- [13] M. Izuha, K. Abe and N. Fukushima // *Jpn. J. Appl. Phys.* **36**, Pt.1 (1997) 5866.

# CRITICAL CURRENT DENSITY IN POLYCRYSTALLINE HIGH- $T_c$ SUPERCONDUCTORS WITH DISORDERED TILT BOUNDARIES

S.A. Kukushkin, A.V. Osipov and I.A. Ovid'ko

Institute of Problems of Mechanical Engineering, Russian Academy of Sciences,  
Bolshoi 61, Vas. Ostrov, St. Petersburg, 199178, Russia

Received: November 18, 1999

**Abstract.** A theoretical model is suggested which describes the effect of tilt boundaries with chaotically arranged dislocations on the critical current density in high-transition-temperature ( $T_c$ ) superconductors. Stress fields of such boundaries, that suppress high- $T_c$  superconductivity, are revealed to be long-range as compared to those of tilt boundaries with periodically ordered grain boundary dislocations. With this factor taken into consideration, the dependence of the critical current density across tilt boundaries on boundary misorientation  $\theta$  is calculated and compared with the experimental data [1].

## 1. INTRODUCTION

The transport properties of grain boundaries in high- $T_c$  superconducting materials are the subject of intensive theoretical and experimental studies (e.g., see [1-14]) motivated by extremely large interest to applications of such materials. It has been experimentally revealed that grain boundaries drastically suppress the superconducting critical current [1-3]. In particular, the critical current density,  $j_c$ , across tilt boundaries in  $\text{YBa}_2\text{Cu}_3\text{O}_{7-\delta}$  superconductors decreases with boundary misorientation angle  $\theta$  as follows:  $j_c(\theta) \approx j_c(0^\circ) \exp(-\theta/8^\circ)$ , for  $\theta$  ranging from  $0^\circ$  to  $15^\circ$ . The critical current density  $\gamma_c(\theta)$  across high-angle tilt boundaries with  $\theta > 15^\circ$  is tentatively constant and low:  $j_c(\theta > 15^\circ) \approx 0.02 j_c(0^\circ)$  [1-3].

Microscopic mechanism of the grain boundary effect on high- $T_c$  superconductivity is not understood yet, though several models of the effect in question have been suggested [5-14]. In particular, theoretical models have been elaborated describing the grain boundary effect as that related to the following factors: (i) a decrease of electron free path in vicinities of grain boundaries [6]; (ii) stress-field-induced structural disorder and pinning of magnetic vortices at grain boundaries [7-9]; (iii) formation of the antiferromagnetic phase within grain boundary cores [10]; (iv) faceting of grain boundaries and  $d$ -symmetry of the superconducting order parameter [11]; (v) deviations from bulk stoichiometry in vicinities of grain boundaries [12-14].

Most models discussed treat stress fields of grain boundary dislocations as those responsible for suppression of the superconducting order parameter in vicinities of grain boundaries in high- $T_c$  superconductors [7-10]. Though the concrete mechanism of the suppression is not unambiguously recognized yet, many researchers assume the existence of a critical stress,  $\sigma_c$ , which characterizes superconductor-to-non-superconductor transition in stressed regions [7-10]. More precisely, superconductivity is supposed to be completely suppressed in regions where some component(s) of stress tensor is (are) larger than  $\sigma_c$ . However, this idea is in contradiction with experimental data in case of low-angle boundaries consisting of periodically arranged lattice dislocations (Fig. 1a). Actually, for any value of  $\sigma_c$ , the volume fraction of "critically stressed" regions (regions where some component(s) of stress tensor is (are) larger than  $\sigma_c$ ) in vicinities of such low-angle boundaries (that create short- or intermediate-range stress fields which drop as  $\exp(-x/h_0)$ , where  $x$  denotes the distance from a boundary plane, and  $h_0$  the interspacing (period) between periodically arranged dislocations, see (Figs. 1a and 2a) decreases with boundary misorientation  $\theta$ .

This, in context of the idea on existence of the critical stress  $\sigma_c$ , results in increase of the critical current density,  $j_c$ , with boundary misorientation  $\theta$ , while experiments [1-3] are indicative of the fact that  $j_c$  drastically decreases with  $\theta$  in the range of  $\theta$  from  $0^\circ$  to tentatively  $15^\circ$ . In order to avoid the contradiction dis-

Corresponding author: I.A. Ovid'ko, e-mail: ovidko@def.ipme.ru

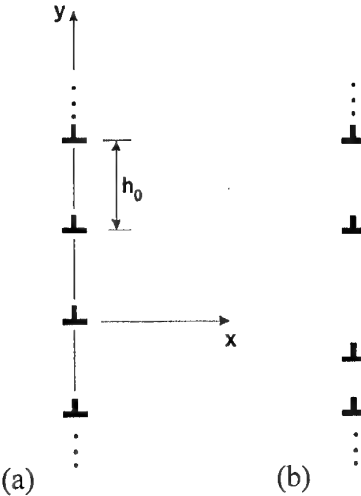


Fig. 1. Ordered and disordered, low-angle tilt boundaries are represented as (a) periodically ordered and (b) disordered walls of crystal lattice dislocations of the edge type, respectively.

cussed, Gurevich and Pashitskii [10] assume that the non-superconducting, critically stressed regions consist of two, normal metal and antiferromagnetic, phases, in which case the antiferromagnetic phase effectively destroys the coupling of Cooper electrons in vicinities of grain boundaries.

In this paper we suggest an alternative model of the grain boundary effect on high- $T_c$  superconductivity, based on both the idea on critical stress  $\sigma_c$  and that on disorder in spatial arrangement of grain boundary dislocations in high- $T_c$  superconductors. Actually, high- $T_c$  superconducting materials commonly are synthesized at non-equilibrium conditions at which grain boundary dislocations can form "non-equilibrium" structures (Figs. 1b and 2b) that are different from "equilibrium", periodic ones (Figs. 1a and 2a). In this situation, grain boundaries in high- $T_c$  superconducting materials, as with boundaries in conventional materials synthesized at non-equilibrium conditions [15,16], create long-range stress fields which drop as  $x^{-1/2}$  or  $x^{-3/2}$ . The main aim of this paper is to calculate the angular dependence of the critical current density,  $j_c(\theta)$ , in high- $T_c$  superconductors with tilt boundaries containing disorderedly distributed dislocations.

## 2. MODELS OF LOW- AND HIGH-ANGLE TILT BOUNDARIES IN HIGH- $T_c$ SUPERCONDUCTORS

Stress fields of grain boundaries, in fact, are created by boundary defects (first of all, dislocations) whose parameters are caused by the structural geometry of boundaries. So, low-angle tilt boundaries (with misorientation  $\theta$  ranging from  $0^\circ$  to  $\theta_c \approx 15^\circ$ ) are ef-

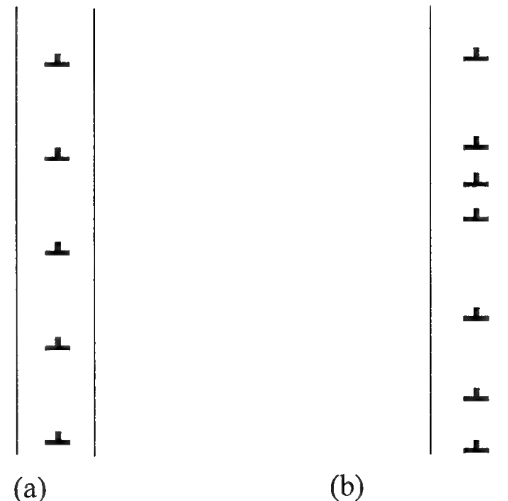


Fig. 2. High-angle tilt boundaries with (a) periodically ordered and (b) disordered ensembles of grain boundary dislocations.

fectively represented as walls of lattice dislocations (of the edge type) with Burgers vectors being those of the crystalline lattice [17,18] (Fig.1). For  $\theta > \theta_c$ , cores of lattice dislocations overlap which compose grain boundaries. As a corollary, high-angle tilt boundaries (with  $\theta > \theta_c$ ) have layer-like cores (characterized by thickness  $\approx 1$  nm) (Fig.2) with the structure being different from the crystalline structure of adjacent grains. The layer-like cores of high-angle boundaries commonly contain grain boundary dislocations (Fig.2) with Burgers vectors being those of displacement-shift-complete lattices of high-angle boundaries [18]. Moduli of such Burgers vectors commonly are lower than moduli of Burgers vectors of crystal lattice dislocations composing low-angle boundaries.

Grain boundaries at equilibrium conditions form either periodic (Figs. 1a and 2a) [17,18] or quasiperiodic [18-20] ensembles that correspond to minimum elastic energy density of such boundaries. Grain boundaries in polycrystalline materials synthesized at highly non-equilibrium conditions are non-equilibrium in the sense that they are characterized by disorder in spatial arrangement of boundary dislocations (see Figs. 1b and 2b). In doing so, ensembles of grain boundary dislocations at high-angle boundaries (Fig. 2b), in general, are more disorderedly distributed than lattice dislocations composing low-angle boundaries (Fig. 1b). The aforesaid is related to the fact that dislocations at high-angle boundaries are characterized by small Burgers vectors as compared to those at low-angle boundaries; in this case displacements of dislocations from their equilibrium positions at high-angle boundaries are accompanied by low changes in the elastic energy den-

sity as compared to those of dislocations composing low-angle boundaries.

Now let us consider a low-angle tilt boundary of infinite extent, which consists of lattice dislocations periodically spaced in plane  $yz$  in coordinate system shown in (Fig. 1a). Such dislocations are characterized by ordinates  $y_n = nh_0$  and Burgers vectors  $\bar{b} = (b, 0, 0)$  with  $h_0$  and  $b$  being in the Frank's relationship [18]:  $b = 2h_0 \sin(\theta/2)$ . Dislocations at "non-equilibrium" tilt boundary (Fig. 1b) are assumed to be displaced by  $h_0 \delta_n$  ( $-a < \delta_n < a$ ) in a randomly uniform way from their "equilibrium" positions corresponding to the periodic arrangement shown in Fig. 1a. In other words, the probability of finding the  $n$ th dislocation in an infinitesimal interval  $(y_n, y_n + dy)$  belonging to the interval  $y_n - a \leq y \leq y_n + a$  is equal to  $dy/2a$ . In the situation discussed, ordinates of the dislocations composing the "non-equilibrium" tilt boundary (Fig. 1b) are given as:

$$y_n = \frac{b(n + \delta_n)}{2 \sin(\theta/2)}, \quad (1)$$

where

$$\langle \delta_n \rangle = 0, \langle \delta_n^2 \rangle = \frac{a^2}{3}, \langle \delta_m \delta_n \rangle = 0, \quad (2)$$

with  $\langle \dots \rangle$  being the averaging on the non-equilibrium dislocation ensemble. The dispersion of grain boundary stress is equal to the sum of the dispersions of stresses induced by the boundary dislocations:

$$D\sigma_{\alpha\beta}(x, y) = \sum_{n=-\infty}^{\infty} \{ \langle [\sigma_{\alpha\beta}(x, y)]^2 \rangle - \langle [\sigma_{\alpha\beta}(x, y)] \rangle^2 \} \quad (\alpha, \beta = (x, y)) \quad (3)$$

with  $\sigma_{\alpha\beta}^{(n)}$  (on the r.h.s. of formula (3)) being the stress field of the  $n$ th dislocation, which, following [17], can be written as:

$$\frac{\sigma_{xx}^{(n)}}{G} = \frac{b}{2\pi(1-\mu)} \frac{(y - y_n)[3x^2 + (y - y_n)^2]}{[x^2 + (y - y_n)^2]^2}, \quad (4)$$

$$\frac{\sigma_{yy}^{(n)}}{G} = \frac{b}{2\pi(1-\mu)} \frac{(y - y_n)[x^2 + (y - y_n)^2]}{[x^2 + (y - y_n)^2]^2}, \quad (5)$$

$$\frac{\sigma_{xy}^{(n)}}{G} = \frac{b}{2\pi(1-\mu)} \frac{x[x^2 - (y - y_n)^2]}{[x^2 + (y - y_n)^2]^2}, \quad (6)$$

$$\frac{\sigma_{zz}^{(n)}}{G} = \frac{\mu}{G} (\sigma_{xx}^{(n)} + \sigma_{yy}^{(n)}), \quad (7)$$

Here  $G$  denotes the shear modulus, and  $\mu$  the Poisson ratio.

After some algebra based on the calculation scheme [15], from (1)–(7) we have found the averaged (on the ordinate  $y$ ) dispersion,  $D\sigma_{\alpha\beta}(x)$ , of stress tensor components in vicinity of a non-equilibrium tilt boundary. Following the results of our calculations, the largest dispersion is that of  $\sigma_{xx}$ :

$$D\sigma_{xx}(x) = \left( \frac{Gb}{2\pi h_0(1-\mu)} \right)^2 \frac{5\pi a^2}{4 x \left[ \frac{x^2}{h_0^2} + a^2 \right]}. \quad (8)$$

For any  $x$ , values of  $D\sigma_{xy}$  and  $D\sigma_{yy}$  are lower by factor 5, while values of  $D\sigma_{zz}$  (for  $\mu=0.2$ ; see experimental data [21]) are lower by factor  $\approx 4$  than those of  $D\sigma_{xx}$ . Therefore, in context of the idea [7–10] on the crucial effect of the largest stress tensor component on high- $T_c$  superconductivity, here and in the following we will focus on analysis of the dispersion  $D\sigma_{xx}$ . In doing so, we find the mean value of modulus of  $\sigma_{xx}$  in vicinity of a non-equilibrium tilt boundary of infinite extent to be as follows :

$$\langle |\sigma_{xx}| \rangle = \sqrt{\frac{D\sigma_{xx}}{\pi}}, \quad (10)$$

because  $\langle \sigma_{xx} \rangle = 0$ .

The dispersion of stress tensor components in the case of grain boundaries with partly relaxed dislocation distributions can be calculated by the same methods as with previously examined non-relaxed disordered dislocation ensembles. So, in paper [16] it has been shown that the dispersion in question can be written as  $\Delta^2 D\sigma_{xx}$  with  $\Delta$  ( $0 < \Delta < 1$ ) being the factor of relaxation. In these circumstances, the mean value of modulus of  $\sigma_{xx}$  depends on the distance,  $x$ , from a partly relaxed tilt boundary as follows:

$$\sigma(x) \equiv \langle |\sigma_{xx}| \rangle = \Delta \sqrt{\frac{D\sigma_{xx}}{\pi}} = \frac{G\Delta}{2\pi(1-\mu)} \times \sqrt{\frac{5 \sin(\theta/2)}{2 \frac{x}{b} \left[ 1 + 4 \frac{x^2}{a^2 b^2} \sin^2(\theta/2) \right]}} \quad (11)$$

According to formula (10),  $\sigma(x)$  is strongly affected by the two non-dimensional parameters,  $a$  and  $\Delta$ :  $\sigma \propto x^{-3/2}$ , if  $x \ll ab/2 \sin(\theta/2)$ ; and  $\sigma \propto x^{-1/2}$ , if  $x \gg ab/2 \sin(\theta/2)$  [15].

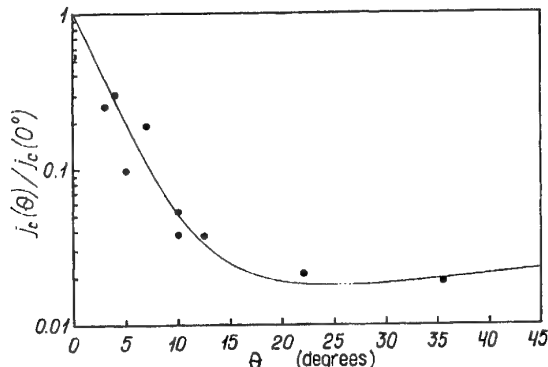


**Fig.3.** Theoretical (solid curve) and experimental [1] (dots) dependences of the averaged density ( $j_c$ ) of the superconducting critical current across “non-equilibrium” tilt boundaries on boundary misorientation ( $\theta$ ).

### 3. CRITICAL CURRENT DENSITY ACROSS DISORDERED TILT BOUNDARIES

In spirit of models [7-10], let us assume that high- $T_c$  superconductivity disappears in stressed regions in which  $\sigma(x) > \sigma_c = \alpha_c G$ , where  $\alpha_c \ll 1$ . Following [8],  $\alpha_c \approx 10^{-2}$ . In the situation discussed, we find that the non-superconducting phase in vicinity of a tilt boundary with a partly relaxed dislocation distribution lies in the layer:  $-x_c < x < x_c$ , where  $x_c$  is extracted from equation  $\sigma(x = x_c) = \alpha_c G$ . For definiteness, let us assume that the non-superconducting phase exhibits the normal metal properties. Then, according to the theory of Cooper pairs tunneling [22,23], we find the critical current density across a normal metal layer of thickness  $2x_c$  in vicinity of the tilt boundary to be as follows:

$$\frac{j_c(\theta)}{j_c(0^\circ)} = \exp(-2x_c(\theta)/\xi), \quad (11)$$

where  $\xi$  is the electron coherence length in the normal metal phase. Formula (10) and (11) allow one to calculate  $x_c(\theta)$  and, therefore, the dependence of the critical current density,  $j_c$ , on boundary misorientation.

In the framework of the suggested model, the angular dependence of  $j_c$  was calculated as that optimally corresponding to the experimental data [1], in which case parameters,  $a$  and  $\Delta$ , was used as adjusting parameters. In doing so, for characteristic values of  $\mu = 0.2$  [21],  $\alpha_c = 10^{-2}$  and  $\xi/b=5$ , we find the optimal correspondence between our theoretical calculations of  $j_c(\theta)$  and the experiments [1] (Fig.3) to come into play at  $a_{opt} \approx 4.13$  and  $\Delta_{opt} = 0.313$ . Fig.3 is indicative of a satisfactory agreement between the model under consideration and the experimental data [1].

Analysis of the theoretical dependence  $j_c(\theta)$  shows that this dependence is weakly affected by parameters,  $\xi/b$  and  $\alpha_c$ , because  $a_{opt} \approx 0.83\xi/b$ , and  $\Delta_{opt}$  runs parallel with  $\alpha_c$  at constant  $a$ . When  $\xi/b$  grows, value of  $\Delta_{opt}$  weakly increases. With this taken into consideration, we find that “structural transition” from low-angle tilt boundaries (weakly disordered walls of dislocation with large Burgers vectors; see Fig.1b) to high-angle tilt boundaries (containing highly disordered ensembles of dislocations with small Burgers vectors; see Fig.2b) occurring at  $\theta \approx \theta_c$  does not result in any jump-like changes of the theoretical dependence  $j_c(\theta)$  at  $\theta \approx \theta_c$  (see Fig.3).

### 4. CONCLUSION

In conclusion, in this paper we have developed a theoretical model which describes the tilt boundary effect on high- $T_c$  superconductivity as that related to long-range stresses (which suppress the superconducting order parameter) created by tilt boundaries with disorderly arranged dislocations. In this context, the disorder of grain boundary dislocation ensembles is caused by highly non-equilibrium conditions of synthesis of polycrystalline high- $T_c$  superconductors. The angular dependence,  $j_c(\theta)$ , calculated within the framework of the suggested model, is in a satisfactory agreement with the experimental data [1] (see Fig.3).

### ACKNOWLEDGMENTS

This work was supported, in part (for I.A.O.), by the Office of US Naval Research (grant N00014-99-1-0896).

### REFERENCES

- [1] D. Dimos, P. Chaudhari, J. Mannhart and F.K. LeGoues // *Phys. Rev. Lett.* **61** (1988) 219.
- [2] D. Dimos, P. Chaudhari and J. Mannhart // *Phys. Rev. B* **41** (1990) 4038.
- [3] T. Amrein, M. Seitz, D. Uhe, L. Schultz and K. Urban // *Appl. Phys. Lett.* **63** (1993) 1978.
- [4] M. Prester // *Supercond. Sci. Technol.* **11** (1998) 33.
- [5] N.D. Browning, E.M. James, K. Kyosuke, I. Arslan, J.P. Buban, J.A. Zaborac, S.J. Pennycook, Y.Xin and G. Duscher // *Rev. Adv. Mater. Sci.* **1** (2000) 3.
- [6] K.E. Bagnall, I.V. Grigorieva and J.W. Steeds // *Supercond. Sci. Technol.* **8** (1995) 605.
- [7] D. Agassi, C.S. Pande and R.A. Masumura // *Phys. Rev. B* **52** (1995) 16237.
- [8] M.F. Chisholm and S.J. Pennycook // *Nature* **351** (1991) 47.

- [9] K. Jagannadham and J. Narayan // *Philos. Mag.* **61** (1990) 129.
- [10] A. Gurevich and E.A. Pashitskii // *Phys. Rev. B* **57** (1998) 13878.
- [11] H. Hilgenkamp, J. Mannhart and B. Mayer // *Phys. Rev. B* **53** (1996) 14586.
- [12] S.E. Babcock and D.C. Larbalestier // *Appl. Phys. Lett.* **55** (1989) 393.
- [13] D.M. Kroeger, A. Choudhary, J. Brynestad, R.K. Williams, R.A. Padgett and W. Goghan // *J. Appl. Phys.* **64** (1988) 331.
- [14] A.Yu. Kraevskii and I.A. Ovid'ko // *Phys. Sol. State* **42** (2000).
- [15] A.A. Nazarov, A.E. Romanov and B. Baudelet // *Philos. Mag. Lett.* **68** (1993) 303.
- [16] A.A. Nazarov, R.Z. Valiev and A.E. Romanov // *Sol. State Phen.* **35/36** (1994) 381.
- [17] J.P. Hirth and J. Lothe, *Theory of Dislocations* (N.Y.:McGraw-Hill, 1975).
- [18] A.P. Sutton and R.W. Balluffi, *Interfaces in Crystalline Materials* (Oxford, Clarendon Press, 1995).
- [19] K.N. Mikaelyan, I.A. Ovid'ko and A.E. Romanov // *Mater. Sci. Eng. A* **259** (1999) 132.
- [20] I.A. Ovid'ko // *Mater. Sci. Eng. A* **280** (2000) 355.
- [21] M. Cankurtaran, G.A. Saunders, J.R. Willis, A. Al-Kheffaji and D.P. Almond // *Phys. Rev. B* **39** (1989) 2872.
- [22] P.G. De Gennes // *Rev. Mod. Phys.* **36** (1964) 225.
- [23] A. Barone and G. Paterno, *Physics and Applications of the Josephson Effect* (N.Y., Wiley, 1982).

# TEM AND STM INVESTIGATIONS ON THE DISCLINATION NATURE OF FRAGMENT BOUNDARY TRIPLE JUNCTIONS

M. Seefeldt

Freiberg University of Mining and Technology, Institute of Physical Metallurgy, Gustav-Zeuner-Straße 5,  
D-09596 Freiberg, Germany

Present address: Catholic University of Leuven, Department of Metallurgy and Materials Engineering, Willem de  
Croylaan 2, B-3001 Heverlee, Belgium

Received: October 30, 1999

**Abstract.** After a short review of recent TEM measurements to characterize partial disclinations in fragment boundary triple junctions in cold-rolled copper, STM results from the same specimens are presented which support a disclination interpretation of the observed fragment structure. The role of the fragment boundary mosaic or of the corresponding immobile partial disclination network in work-hardening is discussed. Although the orientational mismatches around the fragment boundary triple junctions are only small, the disclination contribution dominates work-hardening behaviour at large strains.

## 1. INTRODUCTION

The substructure development of crystalline metals under cold deformation up to large strains is characterized by the formation of a fragment structure on the mesoscopic scale [1]. Typically, with increasing strain the mean fragment size decreases monotonously starting from the micrometer range, whereas the mean misorientation across the fragment boundaries increases monotonously reaching several degrees [1-3]<sup>1</sup>. In contrast to the cell structure, the fragment structure does not saturate<sup>2</sup> and its formation and evolution are quite universal phenomena which are observed in fcc, hcp, and bcc single- as well as polycrystals [1].

While the coexistence of the cell and fragment structures and the evolutions of their characteristic parameters are well investigated [1-3], the defect composition of the fragment boundary mosaic and its influence on work-hardening are not yet completely understood. Especially, to the authors' knowledge, there is no work-hardening model up to now which takes the fragment structure explicitly into account.

Following the Russian school of plasticity, the authors propose the triple junctions of the fragment

boundaries to have a disclination character [4-6] and, thus, to be sources of long-range stresses hindering dislocation motion and, thereby, contributing to work-hardening at large strains.

## 2. NONCOMPENSATED NODES OF FRAGMENT BOUNDARIES

According to experimental observations, a model describing the fragment structure development as well as its coupling to the macroscopic mechanical behaviour requires tools which take into account such collective behaviour of dislocations that results into the formation, spread-out and enlargement of misorientations and into the presence of long-range stresses in the fragment interiors. A model on the substructure development and work-hardening under cold deformation up to large strains suggested by the present authors [7,8] uses disclinations [9,10] as such a tool. Especially, the formation of partial disclination dipoles (PDD) is modelled through incidental non-balanced trapping of neighbouring mobile dislocations of the same Burgers vector into cell walls and by incidental trapping of mobile dislocations with "matching" Burgers vector into preexisting fragment boundaries [8]. The first PDD configuration corresponds to a both-side terminated excess dislocation wall, the second one to a tilt or twist boundary segment with enlarged misorientation. To describe the non-conservative propa-

<sup>1</sup> Hansen and coworkers use the term «cell block» instead of fragment.

<sup>2</sup> Saturation means in this context that average cell structure parameters like cell size, cell wall width, or misorientation do not change any more.

Corresponding author: M. Seefeldt, e-mail: Marc.Seefeldt@mtm.kuleuven.ac.be

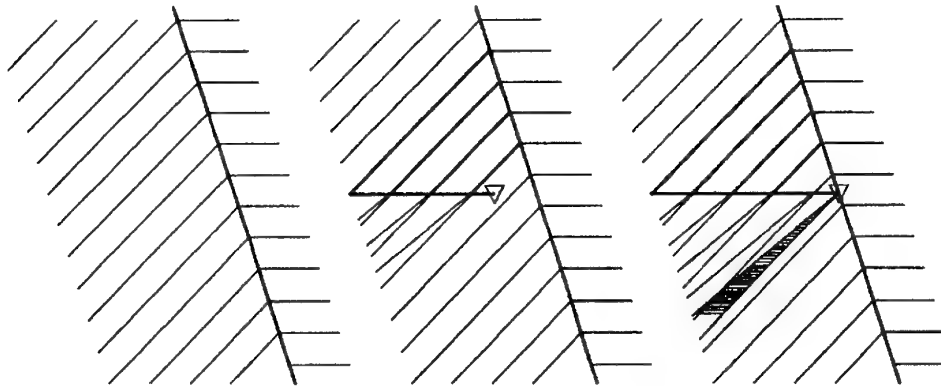


**Fig. 1.** A propagating partial disclination approaches a preexisting fragment boundary, is locked in this boundary and leaves an orientational mismatch behind.

gation of the partial disclinations of such dipoles along cell walls or fragment boundaries, respectively, the capturing mechanism proposed by Vladimirov and Romanov [10,11] is used.

If a partial disclination propagates like that and approaches a preexisting fragment boundary, then it will rotate the crystal regions to the left and to the right of the growing backward fragment boundary against each other (Fig. 1b). When it is finally locked in the preexisting fragment boundary, an orientational mismatch is left behind (Fig. 1c). This mismatch can be accommodated in two different ways: either "plastically" by generation of an additional dislocation boundary or "elastically" by rotational distortion. In the latter case, the triple junction is a non-compensated node containing a line defect of the disclination type.

### 3. TEM RESULTS

Since partial disclinations locked in the triple junctions of the fragment boundaries should – at least at low homologous temperatures – be stable under load relaxation, they are suitable objects for an experimental confirmation of the disclination approach used in the above mentioned model. TEM microdiffraction measurements around fragment boundary triple junctions in copper single and polycrystals rolled down to 70% and 50% thickness reduction at room temperature, respectively, showed [12]

- that the product of the three misorientation matrices does not give the identity and
- that the local orientation varies continuously when passing with the electron beam by the node.

Whereas the first observation proves an orientational mismatch, the second one points towards its accommodation by elastic distortion rather than by an additional dislocation boundary. Both items together indicate that the triple junction includes an additional line defect which has – probably beside other

contributions [13,14] – a disclination nature. The measured orientational mismatches correspond to Frank vectors of

$$\vec{\omega} = [-0.0292, 0.0094, 0.0052] \text{ with } |\vec{\omega}| = 1.78^\circ, \quad (1)$$

for a node in the single crystal specimen and

$$\vec{\omega} = [-0.0046, -0.0316, 0.0004] \text{ with } |\vec{\omega}| = 1.93^\circ, \quad (2)$$

for a node in the polycrystal specimen. These PD powers are in good agreement with the theoretical expectation of  $|\vec{\omega}| \approx 1-3^\circ$  given by Romanov and Vladimirov in [10]. At present, PDD groups in a copper single crystal rolled down to 60% thickness reduction as shown in the TEM micrographs in Figs. 2 and 3 are analysed.

First results indicate that the PDD groups are not fully compensating dipole (Fig. 2) and quadrupole (Fig. 3) configurations, respectively [15].

### 4. STM RESULTS

Since it is very difficult to find sufficiently large perfect crystal volumes to obtain Kikuchi patterns in the surroundings of the nodes in heavily deformed metals, an additional local characterization method which does not make use of diffraction is desirable. Scanning tunnel microscopy (STM) is such a method. In their pioneering works, Vettegren' et al. [16-20] have studied the profiles of polished surfaces of loaded copper, gold, and molybdenum specimens and found clusters of etch pits. The pits have been explained by the exit of dislocation groups after bursting through barriers on intersecting glide planes, whereas the clusters have been interpreted as an early stage of crack formation [21].

Unfortunately, the STM contrast theory is not yet very well developed. It is known [22] that the strong electric field between the tip and the surface has an etching effect. It is generally admitted that this "field etching" should also result into preferred evaporation

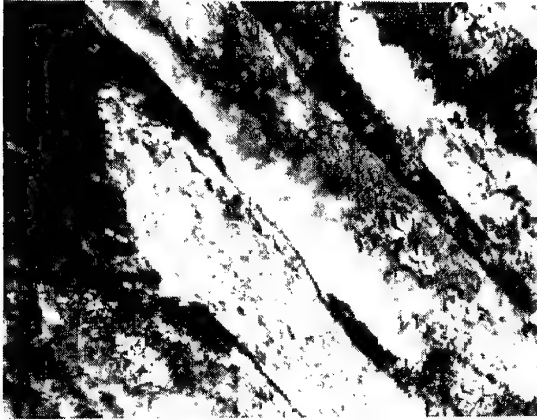


Fig. 2. TEM micrograph of a partial disclination dipole configuration. Copper single crystal rolled down to 60% thickness reduction at room temperature.  $2.61 \times 1.90 \mu\text{m}^2$ .

and/or surface diffusion at high-energy surface regions. From an analogy to Mullins' thermal etching theory [23], one can conclude that etch grooves should arise and deepen at the lines where planar defects like grain boundaries or fragment boundaries reach the surface. Depth and shape  $z(x,t)$  of the grooves scale with the plane energy  $\gamma$  of the planar defect, e.g. for thermal etching with dominating evaporation and condensation through [23]

$$z(x,t) = -2 \tan \beta \sqrt{At} \operatorname{erfc} \left( \frac{x}{2\sqrt{At}} \right) \quad (3)$$

with  $\beta$  defined by the mechanical equilibrium between the planar defect (e.g. grain boundary) tension and the surface tensions,  $2\gamma_s \sin \beta = \gamma_{gb}$ , and  $A$  given by

$$A = \frac{\rho_0 \gamma_s \Omega^2}{(2\pi M)^{1/2} (k_B T)^{2/3}} \quad (4)$$

with vapour pressure  $\rho_0$  for plain surface, atomic volume  $\Omega$ , atomic mass  $M$  and temperature  $T$ . Fragment boundaries can be approximated as low-angle grain boundaries, so that their plane energy can be expressed through the misorientation, e.g. for a tilt boundary [24]

$$\gamma_s = \frac{Gb}{4\pi(1-\nu)} \varphi \left( \ln \frac{b}{r_0} - \ln \varphi \right) \quad (5)$$

with misorientation  $\varphi$  and dislocation core radius  $r_0$ . Thus, at least in the thermal etching analogy, the groove depth and shape are directly related to the fragment boundary misorientation. Correspondingly, "field etching" should also result into notching of etch pits at the points where line defects like dislocations or disclinations reach the surface. Depth and shape of the pits should then scale with the line energy, that means

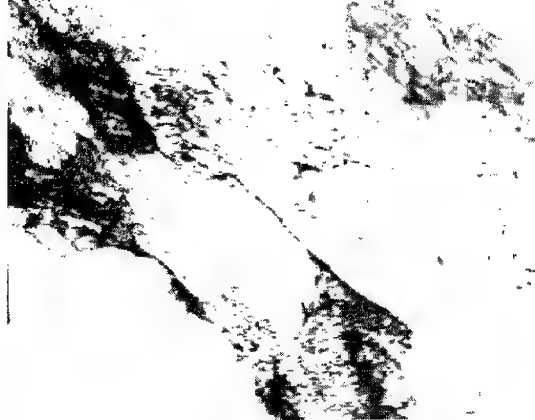


Fig. 3. TEM micrograph of a partial disclination quadrupole configuration. Copper single crystal rolled down to 60% thickness reduction at room temperature.  $1.59 \times 1.16 \mu\text{m}^2$ .

with the powers or with the moduli of the Burgers or Frank vectors, respectively. Although Romanov has given the elastic fields around PDDs reaching the surface [25], there is no etch pit theory up to now, not even for the thermal analogy. Therefore, the following discussion has to remain a qualitative one: If the triple junctions of fragment boundaries include additional high-energy line defects, then the corresponding etch pits should be much deeper than the etch grooves corresponding to the joining fragment boundaries.

For the present work, cut surfaces of copper polycrystals rolled at room temperature have been abraded, polished and treated with the basic alumina OPS be-



Fig. 4. STM surface profile with fragment boundary grooves. Copper polycrystal rolled down to 70% thickness reduction at room temperature. Arrow "A" marks a splitting point of a fragment boundary, arrow "B" a triple junction, arrows "C" a chain of nearly equidistant shallow etch pits.  $5 \times 5 \mu\text{m}^2$ . Grey scale from white to black corresponding to 15 nm depth.

fore being investigated with a Nanoscope II STM. Fig. 4 shows a  $5 \times 5 \mu\text{m}^2$  surface profile from a copper polycrystal rolled down to 71% thickness reduction. The parallelity of the two grooves on the left (to each other and also to the very much different structure of a chain of nearly equidistant small pits marked with the arrows "C"!), the similarity of the defect structure with the one observed in TEM (confer e.g. [2,26]), especially the band width in the micrometer range and the splitting up of one groove into two neighbouring ones at the point "A" (confer splitting up of dense dislocation walls (DDW) into first generation microbands (MB1),

e.g. [2,26]) point to a deformation-induced rather than to a polishing effect.

Fig. 5 gives the scanning profiles for the three lines marked in Fig. 4, line 1 cutting through the two neighbouring ordinary grooves, line 2, in addition to this, cutting through the triple junction marked with "B", and line 3 cutting through the splitting point marked with "A". Obviously, the pits at the triple junctions are deeper than the ordinary grooves by about a factor 2 which might indicate the presence of an additional high-energy line defect, e.g. a partial disclination.

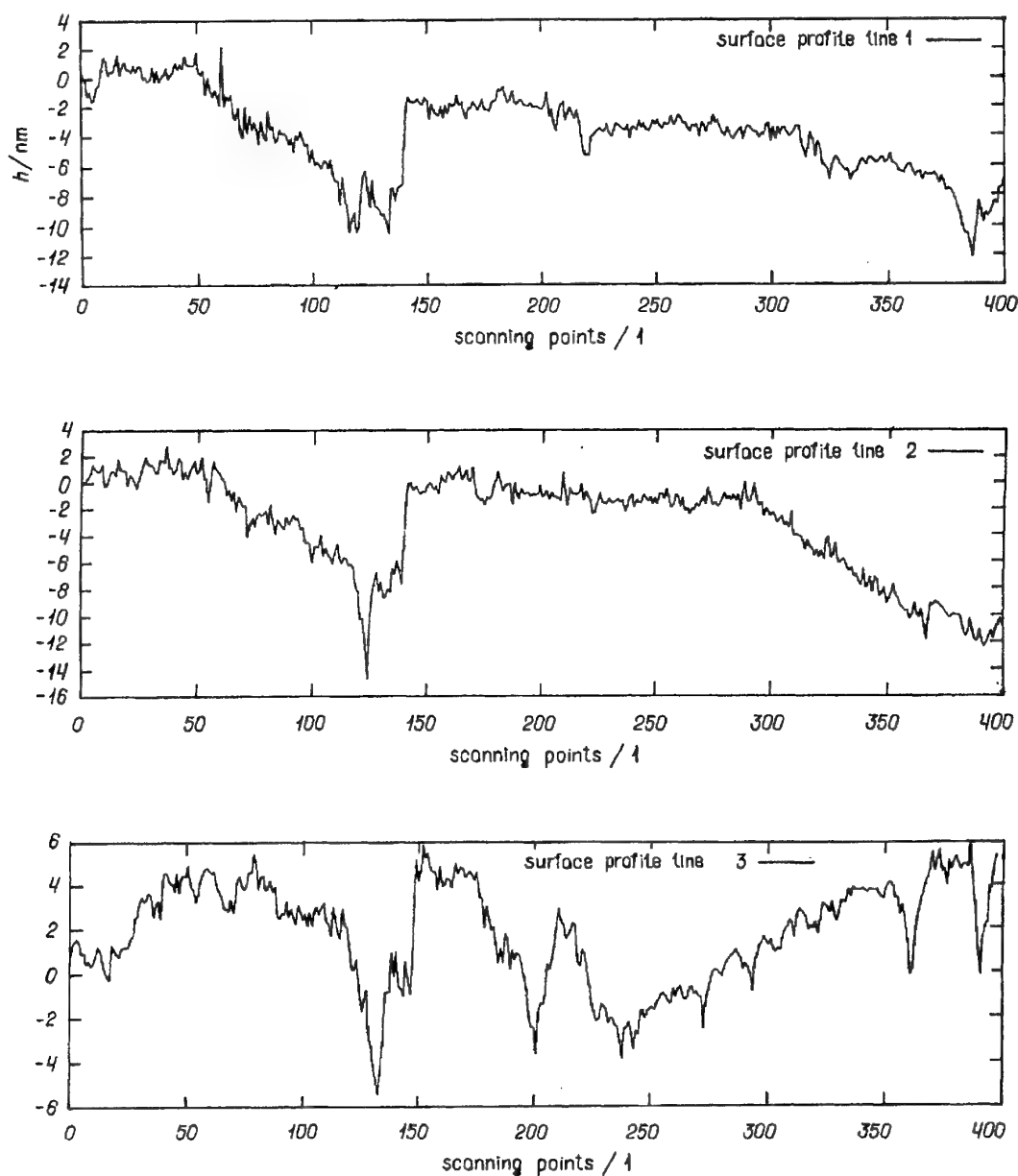


Fig. 5. STM surface profiles along the lines 1-3 in Fig. 4. 400 scanning points correspond to  $5 \mu\text{m}$ .

## 5. EFFECT ON WORK-HARDENING

In a disclination-based model for the fragment structure development like the one proposed in [7,8], propagating PDDs are immobilized as discussed in section 2 and Fig. 1 – resulting in a mosaic of fragment boundaries or, correspondingly, in a network of immobile partial disclinations in the node lines of this mosaic. The evolutions of the cell wall dislocation density and of the propagating and immobile disclination densities can be described with the equations [8]

$$\frac{d\rho_c}{d\epsilon} = I\sqrt{\rho_c} - R\rho_c, \quad (6)$$

$$\frac{d\theta_p}{d\epsilon} = \frac{K_c}{N}\sqrt{\rho_c} + \frac{K_f}{N}\sqrt{\theta_c} - J\theta_c\theta_p, \quad (7)$$

$$\frac{d\theta_i}{d\epsilon} = J\sqrt{\theta_c}\theta_p, \quad (8)$$

including immobilization ( $I$ -term) of mobile and dynamic recovery ( $R$ -term) of mobile with cell wall dislocations, PDD generation by incidental non-balanced trapping of  $N$  neighbouring mobile dislocations into cell walls ( $K_c$ -term) and by incidental trapping of mobile dislocations with the “right” Burgers vector into fragment boundaries ( $K_f$ -term), and immobilization of propagating PDDs in the network of immobile ones ( $J$ -term). The coefficients can be estimated from physical models for the elementary processes [7,8]. Whereas the cell wall dislocation density saturates according to the Kocks-type equation (6), the immobile disclination density increases monotonously according to equation (8) – corresponding to a monotonously decreasing mean fragment size.

The cell wall dislocation density is coupled to a flow stress contribution according to

$$\Delta\sigma_p = \frac{\xi\alpha Gb}{m_s}\sqrt{\frac{\rho_c}{\xi}}, \quad (9)$$

where  $m_s$  is the Schmid factor and  $\xi$  denotes the volume fraction of the cell walls. The effect of the immobile disclination density on the flow stress is described by Romanov's and Vladimirov's law [10]

$$\Delta\sigma_p = \beta G|\vec{\omega}|. \quad (10)$$

The mean disclination power  $|\vec{\omega}|$  is equivalent to the average orientational mismatch around the node lines and may – following the discussion in section 2 and Fig. 1 – be approximated by the mean misorientation  $\varphi$ . Assuming a Poisson-Voronoi geometry of the fragment boundary mosaic, the mean misorientation is

calculated by distributing the available excess dislocation density which develops according to ( $E$ -term describes capturing of mobile dislocations by propagating partial disclinations)

$$\frac{d\rho_{ex}}{d\epsilon} = K_c\sqrt{\rho_c} + K_f\sqrt{\theta_c} + E\theta_p, \quad (11)$$

on the total fragment boundary plane area, finally giving [7]

$$\varphi \approx b\rho_{ex}/1.21\sqrt{\theta_c}. \quad (12)$$

Integration of the evolution equations (6–8) and the flow stress contributions (9–10) shows that the disclination contribution to flow stress dominates the dislocation one starting from a von Mises strain of about 0.9 (parameters for copper at room temperature). Stage III of single crystal plastic deformation can be attributed to cell structure or dislocation work-hardening, stage IV to fragment or disclination work-hardening [7,8].

## 6. CONCLUSIONS

TEM microdiffraction measurements indicate the presence of line defects of disclination nature in the triple junctions of fragment boundaries. STM shows deep etch pits at the points where the triple junction lines reach the surface – pointing to high-energy line defects in the triple junctions. Although the orientational mismatches remain small, the disclination long-range stress fields do have a significant influence on work-hardening and even dominate the dislocation contribution at large strains.

## REFERENCES

- [1] V.V. Rybin, *Large Plastic Deformation and the Fracture of Metals* (Metallurgiya, Moskva, 1986) (in Russian).
- [2] B. Bay, N. Hansen, D.A. Hughes and D. Kuhlmann-Wilsdorf // *Acta Metall. Mater.* **40** (1992) 205.
- [3] Q. Liu, D. Juul Jensen and N. Hansen // *Acta Mater.* **46** (1998) 5819.
- [4] V.A. Likhachev and V.V. Rybin // *Izv. Akad. Nauk. SSSR Fiz.* **37** (1973) 2433.
- [5] V.I. Vladimirov and I.M. Zhukovskiy // *Fiz. Tverd. Tela* **16** (1974) 346.
- [6] V.A. Likhachev and V.V. Rybin // *Fiz. Tverd. Tela* **18** (1976) 163.
- [7] M. Seefeldt and P. Klimanek // *Modelling Simul. Mater. Sci. Eng.* **6** (1998) 349.
- [8] M. Seefeldt, V. Klemm and P. Klimanek, in: *Investigations and Applications of Severe Plastic*

*Deformation*, Proceedings of the NATO Advanced Research Workshop, edited by T.C. Lowe and R.Z. Valiev (Kluwer, Dordrecht, 1999), in print.

[9] R. de Wit // *J. Res. Natl. Bur. Stand. (US) A* **77** (1973) 49, 359 and 607.

[10] A.E. Romanov and V.I. Vladimirov, Disclinations in Crystalline Solids, in: *Disclinations in Solids*, vol. 9, edited by F.R.N. Nabarro (North Holland, Amsterdam, 1992) p. 191.

[11] V.I. Vladimirov and A.E. Romanov // *Fiz. Tverd. Tela* **20** (1978) 3114.

[12] V. Klemm, P. Klimanek and M. Seefeldt // *Phys. Stat. Sol. (a)* **175** (1999) 569.

[13] V.V. Rybin, N.Yu. Zolotorevskiy and I.M. Zhukovskiy // *Fiz. Met. Metalloved.* **69** (1990) 5.

[14] V.V. Rybin, A.A. Zisman and N.Yu. Zolotorevskiy // *Acta Metall. Mater.* **41** (1993) 2211.

[15] V. Klemm, P. Klimanek and M. Seefeldt, to be published.

[16] V.I. Vettegren', S.Sh. Rakhimov and V.N. Svetlov // *Fiz. Tverd. Tela* **37** (1995) 913.

[17] V.I. Vettegren', S.Sh. Rakhimov and E.A. Bakulin // *Fiz. Tverd. Tela* **37** (1995) 3630.

[18] V.I. Vettegren', S.Sh. Rakhimov and V.N. Svetlov // *Fiz. Tverd. Tela* **37** (1995) 3635.

[19] V.I. Vettegren', S.Sh. Rakhimov and V.N. Svetlov // *Fiz. Tverd. Tela* **38** (1996) 590.

[20] V.I. Vettegren', S.Sh. Rakhimov and V.N. Svetlov // *Fiz. Tverd. Tela* **38** (1996) 1142.

[21] V.I. Vettegren', V.L. Gilyarov, S.Sh. Rakhimov and V.N. Svetlov // *Fiz. Tverd. Tela* **40** (1998) 668.

[22] T.T. Tsong // *Phys. Rev. B* **44** (1991) 13703.

[23] W.W. Mullins // *J. Appl. Phys.* **28** (1957) 333.

[24] P. Paufler and G.E.R. Schulze, *Physikalische Grundlagen mechanischer Festkörpereigenschaften I* (Akademie-Verlag, Berlin, 1978).

[25] A.E. Romanov // *Poverkhnost'* **6** (1982) 121.

[26] D.A. Hughes and N. Hansen // *Mater. Sci. Technol.* **7** (1991) 544.

**International Workshop**  
**on**  
**INTERFACE CONTROLLED MATERIALS: RESEARCH AND DESIGN (ICMRD)**  
*St.Petersburg, Russia, June 7-9, 2000*

**Announcement:**

Much of the recent advancement in technology is based on new and novel materials that have been designed for specific functions. The application of these materials is responsible for the growth of industrial sectors such as electronics, energy and aerospace engineering. The objective of this Workshop is to present current research on advanced interface controlled materials with primary focus on nanostructured materials and high transition-temperature superconducting materials (characterized by nano-scaled coherence length). Special attention will be paid to design of such interface controlled materials with their unique and highly desirable properties. The Workshop objectives are to assess the current status and to identify future directions of research, design and applications of nanostructured bulk solids, films and coatings as well as polycrystalline superconducting materials. Particular emphasis is placed on developing close interactions and fostering future collaborations among scientists and engineers from Russia, the USA and other countries.

**We plan to focus on the following topics:**

Synthesis and processing;  
 Modeling;  
 Characterization and properties (mechanical and transport properties of nanostructured materials, high- and low-current properties of superconducting polycrystalline materials);  
 Design;  
 Applications.

**International Organizing Committee:**

<b>I.A.Ovid'ko</b> (Russian Academy of Sciences, Russia)	<b>B.I.Smirnov</b> (Russian Academy of Sciences, Russia)
<b>C.S.Pande</b> (Naval Research Laboratory, USA)	<b>M.Soto</b> (Office of the US Naval Research, USA)
<b>B.B.Rath</b> (Naval Research Laboratory, USA)	

**Submission of Abstracts for Oral and Poster Presentations:**

Anyone interested in making a contribution to the workshop is invited to submit by email a half page abstract with an application form to Dr.Ilya Ovid'ko (E-mail: [ovidko@def.ipme.ru](mailto:ovidko@def.ipme.ru)) by MAY 1, 2000

Current info on the ICMRD meeting and the application form can be found on the web-site:  
<http://mclab.me.uic.edu/activities.htm>

**Invited Speakers:**

**S.Babcock** (University of Wisconsin at Madison, USA), **U.Balachandran** (Argonne National Laboratory, USA), **M.Baro** (UAB; Bellaterra, Spain), **G.M.Chow** (National University of Singapore, Singapore), **Y.Gogotsi** (University of Illinois at Chicago, USA), **H.Hilgenkamp** (University of Twente, The Netherlands), **Y.Hwu** (Institute of Physics, Taiwan), **P.Jena** (Virginia Commonwealth University, USA), **A.King** (Purdue University, USA), **G.Kiriakidis** (IESL, Greece), **P.Klimanek** (Freiberg Technical University, Germany), **M. Muhammed** (Royal Institute of Technology, Sweden), **I.Ovid'ko** (Russian Academy of Sciences, Russia), **M.Seefeldt** (K.University of Leuven, Belgium), **B.Smirnov** (Russian Academy of Sciences, Russia), **C.Pande** (Naval Research Laboratory, USA), **S.Ranganathan** (Indian Institute of Science, India), **B.B.Rath** (Naval Research Laboratory, USA), **A.Romanov** (Russian Academy of Sciences, Russia), **R.E.I.Schiopp** (Utrecht University, The Netherland), **M.Soto** (Office of Naval Research, USA), **B.Starumal** (Russian Academy of Science, Russia), **T.Tsakalakos** (Rutgers University, USA), **T.Watanabe** (Tohoku University, Japan), **T.Yamasaki** (Himeji Institute of Technology, Japan), **A.Zhilyaev** (Ufa State Aviation University, Russia).

**ADVANCED STUDY CENTER.  
TRANSFER OF COPYRIGHT AGREEMENT**

Article entitled:

Corresponding author:

To be published in the journal: "Materials Physics and Mechanics"

Effective upon acceptance for publication, copyright (including all rights thereunder and including the right to authorise photocopying and reproduction in all media, whether separately or as a part of a journal issue or otherwise) in the above article and any modifications of it by the author(s) is hereby transferred throughout the world and for the full term and all extensions and renewals, to:

*"Advanced Study Center" Co. Ltd., (St. Petersburg, Russia)*

This transfer includes the right to adapt the presentation of the article for use in conjunction with computer systems and programs, including reproduction or publication in machine-readable form and incorporation in retrieval systems.

**Rights of authors**

The following rights are retained by the author(s):

1. Patent and trademark rights and rights to any process or procedure described in the article.
2. The right to photocopy or make single electronic copies of the article for their own personal use, including for their own classform use, or for the personal use of colleagues, provided the copies are not offered for sale and are not distributed in a systematic way outside of their employing institution (e.g. via an e-mail list or public file server). Posting of a preprint version of this work on an electronic public server is permitted. Posting of the published article on a secure network (not accessible to the public) within the author's institution is permitted. However, posting of the published article on an electronic public server can only be done with written permission of Advanced Study Center. Co. Ltd.
3. The right, subsequent to publication, to use the article or any part thereof free of charge in a printed compilation of works of their own, such as collected writings or lecture notes, in a thesis, or to expand the article into book-length form for publication.

**Note**

All copies, paper or electronic, or other use of the information must include an indication of the copyright ownership and a full citation of the journal source. *Please refer requests for all uses not included above, including the authorization of third parties to reproduce or otherwise use all or part of the article (including figures and tables) to:*

Materials Physics and Mechanics  
 Editorial Office  
 Institute of Problems of Mechanical Engineering  
 Russian Academy of Sciences  
 Bolshoj 61, Vas.Ostrov, St.Petersburg 199178, Russia  
 E-mail: [mpm@def.ipme.ru](mailto:mpm@def.ipme.ru)  
 Fax: +(7 812)321 4771

**Authorship**

If the article was prepared jointly with other author(s), the signing author has informed the co-author(s) of the terms of this copyright transfer and is signing on their behalf as their agent and represents that he or she is authorized to do so. Please confirm by marking the appropriate box following the signature line. The signing author shall bear the responsibility for designating the co-author(s) and must inform Advanced Study Center of any changes in authorship.

If copyright is held by the employer, the employer or an authorized representative of the employer must sign. If the author signs, it is understood that this is with the authorization of the employer and the employer's acceptance of the terms of the transfer. Please confirm by marking the appropriate box following the signature line.

**Warranties**

The author(s) warrant(s) that the article is the author's original work and has not been published before. The author(s) warrant(s) that the article contains no libelous or other unlawful statements, and does not infringe on

the rights of others. If experts from copyrighted works are included, the author(s) has (have) obtained or will obtain written permission from the copyright owners and will credit the sources in the article.

Signature of copyright owner(s) \*:

Name (printed):

Title (if employer representative):

Company or institution:

Date:

If any of the following apply, please mark the box(es):

- author on behalf of all co-authors
- employer representative

PLEASE SIGN IN INK AND RETURN THE COMPLETE **ORIGINAL** (do not send by fax), retaining a copy of this form for your files, TO:

Materials Physics and Mechanics  
Editorial Office  
Institute of Problems of Mechanical Engineering  
Russian Academy of Sciences  
Bolshoj 61, Vas.Ostrov, St.Petersburg 199178, Russia  
E-mail: [mpm@def.ipme.ru](mailto:mpm@def.ipme.ru)  
Fax: +(7 812)321 4771

---

\*To be signed by the author, also on behalf of any co-authors, or to be signed by employer, where appropriate.

## INSTRUCTIONS FOR AUTHORS

### Submission of papers:

Manuscript should be submitted in English in both electronic (by e-mail) and hard copy (original +copy) versions.

### Hard copy submission:

Manuscripts should be submitted typed on good quality bond paper of A4 format with 1" margins (right, left, top, bottom), double-spaced, using Times Roman 12 pt font, to:

Materials Physics and Mechanics  
Editorial Office  
Institute of Problems of Mechanical Engineering  
Russian Academy of Sciences  
Bolshoj 61, Vas.Ostrov, St.Petersburg, 199178, Russia  
Fax: +(7 812)321 4771

### Electronic submission:

Manuscripts should be submitted by e-mail to:

E-mail: mpm@def.ipme.ru

Filetypes: TeX (LaTeX) and MS Word files preferred. LaTeX style files are available on the Web-site: <http://www.ipme.ru/e-journals/MPM/>. Pictures and photos should be submitted in TIFF format (400 dpi).

### Length:

Papers should be limited to 30 typewritten pages (including Tables and Figures each on separate page).

### Structure of the manuscript:

Cover sheet; Text; Tables; References; Figure Captions; Pictures and Photos

A cover sheet should be included that contains the complete title, the names, affiliations, mailing addresses of the authors, fax and e-mail address of the corresponding author and the abstract.

TITLE – bold, centered. (14 pt)

Author(s) – bold, centered, e.g. S. R. Brown and T. Klein

Affiliation(s) – centered, complete postal address for all authors, e-mail address of corresponding author.

**ABSTRACT.** About 150-200 words.

Tables: type each table on the separate page, number consecutively in arabic numerals and supply a heading.

### References:

References should be indicated in the text by consecutive numbers in square parentheses, e.g. [1,2,5-7], as a part of the text, the full reference being cited at the end of the text. References should contain the names of the authors together with their initials, the title of the journal, volume number, year and the first page number as illustrated below. References to books should contain the names of the authors, the title (the names of editors), the publisher name, location and year, as illustrated below.

### REFERENCES

[1] R. Birringer, H. Gleiter, H.P. Klein and P. Marquardt // *Phys. Lett.* **102** (1984) 365.

[2] F.R. Nabarro, *Theory of Crystal Dislocations* (Clarendon Press, Oxford, 1967).

[3] V. Provenzano, In: *Nanostructured Materials: Science and Technology*, ed. by G.-M. Chow and N.I Noskova (Kluwer: Dordrecht, 1998), p. 335.

### Figures:

For best results submit illustrations in the actual size at which they should be published. The line drawings of the original should be laser printed, the photographs should be original, with somewhat more contrast than is required in the printed version. Each figure should be typed on separate page, the listing of the figure captions must be included.

Equations must be clearly printed and numbered sequentially with arabic numbers enclosed with round parentheses at the right-hand margin.

Units – the authors are encouraged to use the SI-units, other units are also acceptable.

---

Отпечатано в типографии «Альт-СПб»

Гарнитура Таймс, подписано к печати 06.04.2000

усл. печ. л. 9.5, тираж 950 экз., заказ 289.

<b>AC Magnetic Properties of Compacted FeCo Nanocomposites .....</b>	<b>1</b>
A.K. Giri, K.M. Chowdary and S.A. Majetich	
<b>Nanostructured Ni films by Polyol Electroless Deposition .....</b>	<b>11</b>
J. Zhang, G.M. Chow, S. H. Lawrence and C.R. Feng	
<b>Heteroepitaxial Growth of InAs on Si: the New Type of Quantum Dots .....</b>	<b>15</b>
G.E. Cirlin, N.K. Polyakov, V.N. Petrov, V.A. Egorov, D.V. Denisov, B.V. Volovik, V.M. Ustinov, Zh.I. Alferov, N.N. Ledentsov, R. Heitz, D. Bimberg, N.D. Zakharov, P. Werner and U.G. Osele	
<b>Fabrication of 2-D and 3-D Photonic Band-Gap Crystals in the GHz and THz Regions .....</b>	<b>20</b>
G. Kiriakidis and N. Katsarakis	
<b>A Mathematical Model of Metal Film Deposition from Photoactive Compound Solutions on Solid-Liquid Interface .....</b>	<b>27</b>
S.A. Kukushkin and S.V. Nemenat	
<b>Enhanced Diffusion near Amorphous Grain Boundaries in Nanocrystalline and Polycrystalline Solids .....</b>	<b>31</b>
R.A. Masumura and I.A. Ovidko	
<b>Correlation Between Superconducting Transport Properties and Grain Boundary Microstructure in High-Tc Superconducting Ceramics .....</b>	<b>39</b>
T.S. Orlova, J.Y. Laval and B.I. Smirnov	
<b>Modeling the Influence of Size Effect on Dielectric Response of Thin Ferroelectric Films .....</b>	<b>45</b>
O.G. Vendik and S.P. Zubko	
<b>Critical Current Density in Polycrystalline High-Tc Superconductors with Disordered Tilt Boundaries .....</b>	<b>49</b>
S.A. Kukushkin, A.V. Osipov and I.A. Ovid'ko	
<b>TEM and STM Investigations on the Disclination Nature of Fragment Boundary Triple Junctions .....</b>	<b>54</b>
M. Seefeldt	